Chapter 79

Entangled Atoms and Fields: Cavity QED

Authors

Q. Y. He (Peking University) and W. Zhang (Renmin University of China)

Abstract

Although the concept of a *free atom* is of use as a first approximation, a full quantum description of the interaction of atoms with an omnipresent electromagnetic radiation field is necessary for a proper account of spontaneous emission and radiative level shifts such as the Lamb shift (Chap. 27). This chapter is concerned with the changes in the atom-field interaction that take place when the radiation field is modified by the presence of a cavity. An atom in the vicinity of a plane perfect mirror serves as an example of cavity quantum electrodynamics [1, 2, 3, 4, 5].

The interaction between atom and intracavity light field can significantly change the spontaneous and stimulated emission of light, and induce transitions of the atom between different quantum states. In the case of strong coupling, it also becomes possible for a single atom to control the transmission of light through the cavity, and for a single photon to deterministically change the state of the atom.

Introduction

In the weak coupling regime, the coupling of an excited atom to a broad continuum of radiation modes leads to exponential decay (Fig. 79.1a), as first described by *Weisskopf* and *Wigner* [6]. Spontaneous emission may be enhanced or suppressed in structures such as waveguides or *bad* cavities. Cavities also introduce van der Waals forces and the subtle Casimir level shifts [7].

In the strong coupling regime, the excited atom is strongly coupled to an isolated resonant cavity mode. In the absence of damping, an oscillatory exchange of energy between the atom and the field replaces exponential decay (Fig. 79.1b) with a coherent evolution in time. Experimental investigations of these effects began [8] with the development of suitable resonators and techniques for producing atoms with long lived excited states and strong dipole transition moments.

79.1 Atoms and Fields

79.1.1 Two-level Atoms

Most of the essential features of cavity QED can be elucidated by the two-level model atom discussed in Chapts. 68, 69, 70, and 77 (see also [9]). A ground state $|g\rangle$ and an excited state $|e\rangle$ are

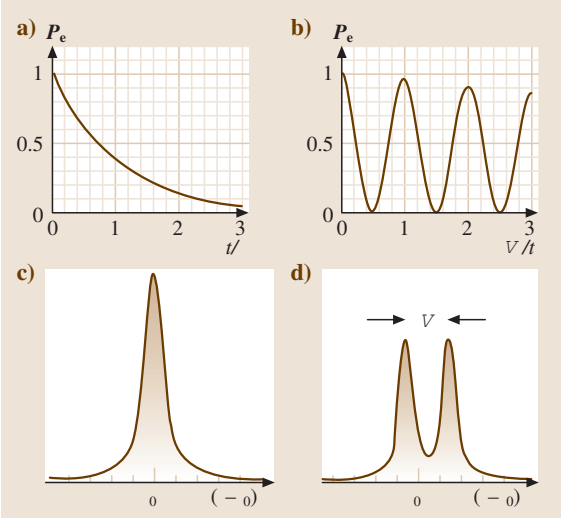

Figure 79.1: *Upper row*: Excitation probability of an excited atom. (a) Exponential decay in free space or bad cavities in the weak coupling limit. (b) Oscillatory evolution in good cavities or in the strong coupling case. *Lower row:* The spectral signature of exponential decay is a Lorentzian line shape (c) while the so-called vacuum Rabi splitting (d) is observed in the strong coupling case

coupled to the radiation field by a dipole interaction. Using the formal equivalence to a spin-1/2 system, the Pauli spin operators are

$$\begin{aligned} \sigma_x &= \sigma_+ + \sigma_- \ , \\ \sigma_y &= -\mathrm{i}\,(\sigma_+ - \sigma_-) \ , \\ \sigma_z &= \sigma_+\sigma_- - \sigma_-\sigma_+ = \left[\sigma_+, \sigma_-\right] \ , \end{aligned} \tag{79.1}$$

with $\sigma_+ = |e\rangle\langle g|$ and $\sigma_- = |g\rangle\langle e|$. The quadratures (out of phase components) of the atomic polarization are given by σ_x and σ_y, while σ_z is the occupation number difference. The free atom Hamiltonian is

$$\mathcal{H}_{\mathrm{atom}} = \frac{1}{2}\hbar\omega_0\sigma_z \ , \tag{79.2}$$

where $\hbar\omega_0 = E_e - E_g$ is the transition energy.

79.1.2 Electromagnetic Fields

Classical Fields Classical electromagnetic fields have longitudinal and transverse components:

$$\boldsymbol{E}(\boldsymbol{r},t) = \boldsymbol{E}^{\mathrm{l}}(\boldsymbol{r},t) + \boldsymbol{E}^{\mathrm{t}}(\boldsymbol{r},t) \ . \tag{79.3}$$

In the Coulomb gauge, the longitudinal part is the instantaneous electric field. The transverse part is the radiation field which obeys the wave equation

$$\left(\nabla^2 - \frac{1}{c^2}\frac{\partial^2}{\partial t^2}\right)\boldsymbol{E}^{\mathrm{t}}(\boldsymbol{r},t) = \frac{1}{\epsilon_0 c^2}\frac{\partial}{\partial t}\boldsymbol{j}(\boldsymbol{r},t) \ . \tag{79.4}$$

In empty space, the driving current density $\boldsymbol{j}(\boldsymbol{r},t)$ vanishes, and the field may be expanded in a set of orthogonal modes as

$$\boldsymbol{E}^{\mathrm{t}}(\boldsymbol{r},t) = \sum_\mu E_\mu(t)\,\mathrm{e}^{-\mathrm{i}\omega_\mu r}\boldsymbol{u}_\mu(\boldsymbol{r}) + \mathrm{c.c.} \ , \tag{79.5}$$

with slowly varying amplitudes $E_\mu(t)$. The spatial distributions $\boldsymbol{u}_\mu(\boldsymbol{r})$ obey the vector Helmholtz equation

$$\left[\nabla^2 + \left(\frac{\omega_\mu}{c}\right)^2\right]\boldsymbol{u}_\mu(\boldsymbol{r},t) = 0 \ , \tag{79.6}$$

depending on geometric boundary conditions as imposed by conductive or dielectric mirrors, waveguides, and resonators. In free space, plane wave solutions $\boldsymbol{u}_\mu(\boldsymbol{r},t) = \boldsymbol{u}_\epsilon\,\mathrm{e}^{\mathrm{i}\boldsymbol{k}\cdot\boldsymbol{r}}$ have a continuous index $\mu = (\boldsymbol{k},\epsilon)$ with wave vector $\boldsymbol{k}$ and an index ϵ for the two independent polarizations. The orthogonality relation

$$\frac{1}{V}\int_V \boldsymbol{u}_\mu \cdot \boldsymbol{u}_\nu^* \mathrm{d}^3\boldsymbol{r} = \delta_{\mu\nu} \tag{79.7}$$

applies. For a closed cavity, V is the resonator volume. In waveguides and free space, an artificial boundary is introduced and then increased to infinity at the end of a calculation, such that the final results do not depend on V.

Quantum Fields The quantum analog of the classical transverse field in (79.4) is obtained through a quantization of its harmonic modes leading to a number state expansion. Field operators obey standard commutation relations $[a_\mu, a_\nu^\dagger] = \delta_{\mu,\nu}$, and for a single mode with index μ, the amplitude E_μ in (79.5) is replaced by the corresponding operator

$$E_\mu(t) = \mathcal{E}_\mu a_\mu \, \mathrm{e}^{-\mathrm{i}\omega t} \; , \quad E_\mu^\dagger(t) = \mathcal{E}_\mu{}^* a_\mu^\dagger \, \mathrm{e}^{\mathrm{i}\omega t} \; . \tag{79.8}$$

The normalization factor $\mathcal{E}_\mu$ is chosen such that the energy difference between number states $|n\rangle_\mu$ and $|n+1\rangle_\mu$ in the volume V is $\hbar\omega_\mu$, giving

$$\mathcal{E}_\mu \mathcal{E}_\mu{}^\dagger = \frac{\hbar\omega_\mu}{2\epsilon_0 V} \; . \tag{79.9}$$

The Hamiltonian of the free field is

$$\mathcal{H}_{\mathrm{Field}} = \sum_\mu \hbar\omega_\mu \left(a_\mu^\dagger a_\mu + \frac{1}{2} \right) \; . \tag{79.10}$$

In the Coulomb gauge, the vector potential $\boldsymbol{A}(\boldsymbol{r})$ is related to the electric field $\boldsymbol{E} = -\partial \boldsymbol{A}/\partial t$ by

$$\boldsymbol{A}_\mu(\boldsymbol{r}, t) = -\frac{\mathcal{E}_\mu}{\omega_\mu} \left(a_\mu \, \mathrm{e}^{-\mathrm{i}\omega t} + a_\mu^\dagger \, \mathrm{e}^{\mathrm{i}\omega t} \right) \boldsymbol{u}_\mu(\boldsymbol{r}) \; . \tag{79.11}$$

The ground state $|0\rangle_\mu$ is called the vacuum state. While the expectation value $\langle n|\boldsymbol{E}|n\rangle = 0$ for a number state, the variance is not zero, since $\langle n|\boldsymbol{E}\boldsymbol{E}^*|n\rangle > 0$, giving rise to nonvanishing *fluctuations* of the free electromagnetic field.

79.1.3 Dipole Coupling of Fields and Atoms

The combined system of atoms and fields can be described by the product quantum states $|a, n\rangle$ of atom states $|a\rangle$ and field states $|n\rangle$. The interaction Hamiltonian $\mathcal{H}_I$ of the atom and the radiation field is given by (The $\boldsymbol{A}^2$-term plays an important role in energy shifts and can only be neglected when radiative processes involving energy exchange are considered.)

$$\mathcal{H}_{\mathrm{I}} = -\frac{q}{m} \boldsymbol{p} \cdot \boldsymbol{A}(\boldsymbol{r}) + \frac{q^2}{2m} \boldsymbol{A}^2(\boldsymbol{r}) \; . \tag{79.12}$$

This interaction causes the atom to exchange energy with the radiation field. In the dipole approximation, the interaction can be reduced to the commonly used form of $\boldsymbol{p} \cdot \boldsymbol{E}$ [10], with the coupling strength proportional to the component of the atomic dipole moment $\boldsymbol{d}_{eg} = q\langle e|\boldsymbol{r}_{eg}|g\rangle$ along the electric field. The coupling constant

$$g_\mu(\boldsymbol{r}) = |\boldsymbol{d}_{eg} \cdot \boldsymbol{u}_\mu(\boldsymbol{r}) \mathcal{E}_\mu|/\hbar \; . \tag{79.13}$$

In the rotating wave approximation (RWA) (Chapts. 68, 69, and 70),

$$\mathcal{H}_{\mathrm{RWA}} = \sum_\mu \hbar \left(g_\mu \sigma_+ a_\mu + g_\mu^* a_\mu^\dagger \sigma_- \right) \; , \tag{79.14}$$

where we have used the atomic operators of (79.1).

For the simplest scenario of a two-level atom interacting with a mono-mode cavity, the Hamiltonian under RWA reduces to the Jaynes-Cummings (JC) model

$$\mathcal{H}_{\mathrm{JC}} = \frac{1}{2}\hbar\omega_0 \sigma_z + \hbar\omega_C a^\dagger a + \hbar \left(g\sigma_+ a + g^* a^\dagger \sigma_- \right) \; , \tag{79.15}$$

where ω_C denotes the cavity mode frequency, and the zero-point energy of the field is neglected. Note that the JC model is valid only if the RWA can be employed to describe the coherent dipole interaction between the atom and the field mode. This usually requires the coupling constant g is relatively much smaller than the energy scales of ω_0 and ω_C. Research beyond the RWA has been conducted in the regime where the coupling constant g is comparable with the atomic and field frequencies.

In a continuous electromagnetic spectrum, the atom interacts with a large number of modes

having quantum numbers μ, yielding exponential decay of an excited atomic level at the rate [6]

$$\Gamma_{eg} = \frac{2\pi}{\hbar^2} \sum_{\tilde{\mu}} \sum_{\boldsymbol{k}} |g_\mu|^2 \, \delta(\omega_\mu - \omega_0) \ . \quad (79.16)$$

Here we have separated the discrete ($\tilde{\mu}$) and the continuous part (wave vector $\boldsymbol{k}$) of the mode index μ. If g_μ (79.13) does not vary much across a narrow resonance, then

$$\Gamma_{eg} \simeq 2\pi \, |g_\mu(\omega_0)|^2 \sum_{\tilde{\mu}} \rho_{\tilde{\mu}}(\omega_0) \ . \quad (79.17)$$

The density of states corresponding to the continuous mode index $\boldsymbol{k}$ of dimension ν can be evaluated on a ν-dimensional fictitious volume $V^{(\nu)}$ as

$$\rho_{\tilde{\mu}} = \sum_{\boldsymbol{k}} \delta(\omega_{\tilde{\mu},\boldsymbol{k}} - \omega) \to \frac{V^{(\nu)}}{(2\pi)^\nu} \int_0^\infty \mathrm{d}^\nu k \delta(\omega_{\tilde{\mu},\boldsymbol{k}} - \omega) \quad (79.18)$$

provided $\omega(\boldsymbol{k})$ is known, and by converting the sum (This is formally accomplished by taking the limit of $\Delta k = 2\pi/l$ for large l, where l is a linear dimension of an artificial resonator, and the resonator volume is $V = l^3$. If the relation between mode spacing Δk and geometric dimension is nonlinear in a more complex geometry, this analysis can be very complicated.) over plane wave vectors $\boldsymbol{k}$ into an integral.

The Rate of Spontaneous Emission In free space [$\omega(\boldsymbol{k})^2 = (c\boldsymbol{k})^2$], the sum in (79.17) contributes a factor of two, due to polarization, to the total density of states in free space, $\rho_{\mathrm{free}}(\omega) = V\omega^2/\pi^2c^3$. When the vector coupling of atom and field (79.13) is replaced by its average in isotropic free space, that is, by 1/3, the result

$$\Gamma_{eg} = A_{eg} = \frac{e^2 r_{eg}^2 \omega^3}{3\pi\epsilon_0 \hbar c^3} \quad (79.19)$$

is obtained for the decay rate A_{eg} as measured by the natural linewidth Γ_{eg}.

79.2 Weak Coupling in Cavity QED

The regime of weak cavity QED generally applies when an atom is coupled to a continuum of radiation modes. This is always the case with mirrors, waveguides, or bad cavities. The signatures of weak cavity QED are modifications of the rate of spontaneous emission, as well as the existence of van der Waals and Casimir forces. Formally, this regime is well described by perturbation theory.

79.2.1 Radiating Atoms in Waveguides

Within the continuous spectrum of a waveguide, radiative decay of an excited atomic level remains exponential, and Γ_{eg} may be determined as in the preceding section. We now consider the modifications of spontaneous decay in a parallel plate waveguide. According to (79.17), the theoretical problem is reduced to a geometric evaluation of mode densities. Between a pair of mirrors it is convenient to distinguish $\mathrm{TE}_{n\boldsymbol{k}}$ and $\mathrm{TM}_{n\boldsymbol{k}}$ modes, where n is the number of half waves across the gap of width d. The dispersion relation $\omega(\boldsymbol{k})$ reflects the discrete standing wave part ($n\pi/d$) and a running wave part as in free space,

$$\omega_{n,\boldsymbol{k}}^2 = c^2\big(|\boldsymbol{k}|^2 + n\pi/d\big)^2 \qquad \begin{matrix} n = 0, 1, 2, \ldots & \mathrm{TM} \\ n = 1, 2, \ldots & \mathrm{TE} \end{matrix} . \quad (79.20)$$

The average mode density [$\boldsymbol{du} = 1$, (79.13)] is evaluated [(79.18), $\nu = 2$] with an appropriate quantization volume containing the area of the plates, $V = Ad$, giving

$$\begin{aligned} \rho^{\mathrm{TE}}(\omega) &= \frac{\omega_{\mathrm{c}}[\omega]}{2\omega_{\mathrm{c}}^2} \rho_{\mathrm{free}}(\omega_{\mathrm{c}}) \ , \\ \rho^{\mathrm{TM}}(\omega) &= \frac{\omega_{\mathrm{c}}[\omega+1]}{2\omega_{\mathrm{c}}^2} \rho_{\mathrm{free}}(\omega_{\mathrm{c}}) \ , \end{aligned} \quad (79.21)$$

where $[x]$ is the largest integer in x, and $\omega_{\mathrm{c}} = \pi c/d$ gives the waveguide cutoff frequency. Be-

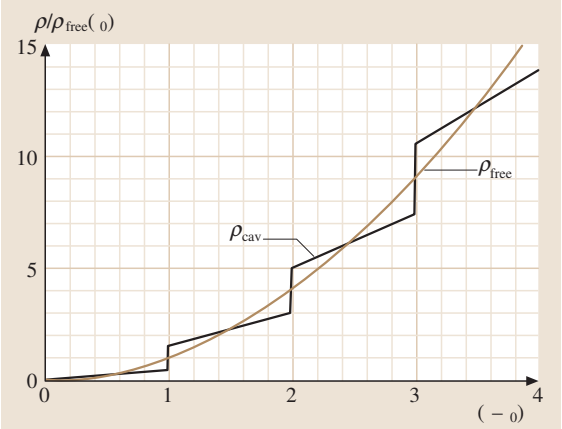

Figure 79.2: Modification of the average vacuum spectral density ($\rho^{\mathrm{TE}} + \rho^{\mathrm{TM}}$) in a parallel plate cavity (*thick line*) compared with free space (*thin line*)

low ω_c, the TE-mode density clearly vanishes and, with the pictorial notion of turning off the vacuum introduced by *Kleppner* [11], inhibition of radiative decay is obvious. Figure 79.2 shows the calculated mode density for a parallel plate waveguide. The decay rate can be calculated from (79.17), with the spatial variation of g_μ included. This configuration was used for the first experiments which showed the suppression of spontaneous emission in both the microwave and the near optical frequency domain [12, 13] with atomic beams.

79.2.2 Trapped Radiating Atoms and Their Mirror Images

Boundary conditions imposed by conductive surfaces may also be simulated by appropriately positioned image charges. Inspired by classical electrodynamics, this image charge model can be successfully used to determine the modifications of radiative properties in confined spaces. In the simplest case, an atom is interacting with its image produced by a plane mirror. Trapped atoms and ions allow one to control their relative posi-

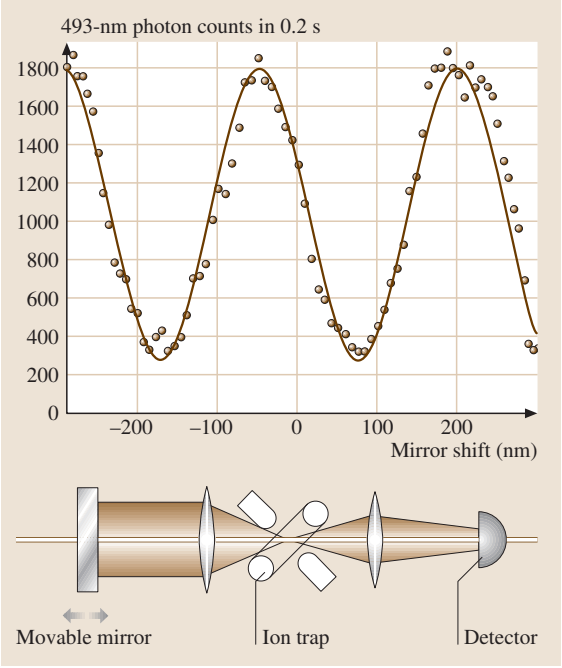

Figure 79.3: Sinusoidal variation of the $\lambda = 493$ nm spontaneous emission rate of a single trapped Ba ion caused by self-interference from a retroreflecting mirror. The experimental arrangement is sketched at the bottom [14]

tion with respect to a mirror to distances below the wavelength of light. Hence they are ideal objects for studying the spatial dependence of the mirror induced modifications of their radiative properties. In an experiment with a single trapped ion (see Fig. 79.3), its radiation field was superposed onto its mirror image [14, 15], yielding a sinusoidal variation of both the spontaneous decay rate and the mirror induced level shift with excellent contrast.

79.2.3 Radiating Atoms in Resonators

Resonators In a resonator, the electromagnetic spectrum is no longer continuous and the discrete mode structure can also be resolved ex-

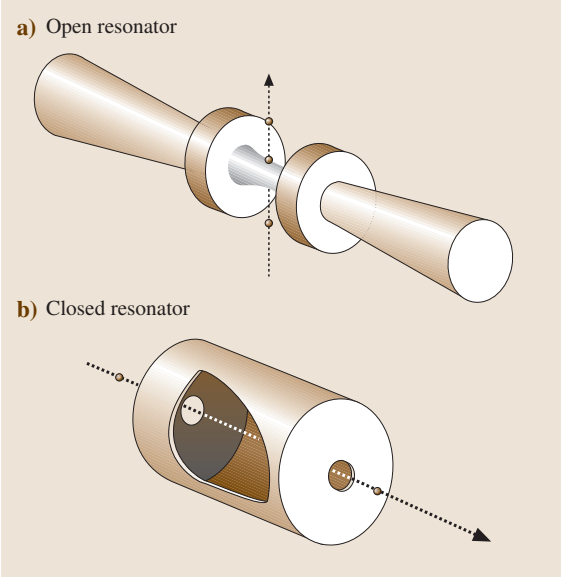

Figure 79.4: Two frequently used resonator types for cavity QED: (a) Open Fabry–Perot optical cavity. (b) Closed *pillbox* microwave cavity

perimentally. While a resonator is only weakly coupled to external electromagnetic fields, it still interacts with a large thermal reservoir through currents induced in its walls. The total damping rate is due to resistive losses in the walls ($\kappa_{\rm wall}$) and also due to transmission at the radiation ports, $1/\tau_\mu = \kappa_\mu = \kappa_{\rm wall} + \kappa_{\rm out}$. An empty resonator stores energy for times

$$\tau_\mu = Q/\omega_\mu \ , \tag{79.22}$$

and the power transmission spectrum is a Lorentzian with width $\Delta\omega_\mu = \omega_\mu/Q_\mu$. The index μ, for instance, represents the TE_{lm} and TM_{lm} modes of a *pillbox* microwave cavity, or the TEM_{klm} modes of a Fabry–Perot interferometer (Fig. 79.4).

When cavity damping remains strong, $\Gamma_\mu \gg \Gamma_{eg}$, the atomic radiation field is *immediately* absorbed and Weisskopf–Wigner perturbation theory remains valid. In this so-called bad cavity limit, resonator damping can be accounted for by an effective mode density of Lorentzian width $\Delta\omega_\mu$ for a single isolated mode,

$$\rho_\mu(\omega) = \frac{1}{\pi}\,\frac{\omega_\mu/2Q_\mu}{(\omega-\omega_\mu)^2 + (\omega_\mu/2Q_\mu)^2} \ . \tag{79.23}$$

Bad and Good Cavities The modification of spontaneous decay is again calculated from (79.17). For an atomic dipole aligned parallel to the mode polarization, and right at resonance, $\omega_\mu = \omega_0$, the enhancement of spontaneous emission is found to be proportional to the Q-value of a selected resonator mode:

$$\frac{\Gamma_{eg}^{\rm cav}}{\Gamma_{eg}^{\rm free}} = \frac{\rho_\mu |\boldsymbol{u}(\boldsymbol{r})|}{\rho_{\rm free}} = \frac{3Q\lambda^3}{4\pi^2 V}\,|\boldsymbol{u}(r)|^2 = \frac{3Q\lambda^3}{4\pi^2 V_{\rm eff}} \ , \tag{79.24}$$

where the effective mode volume is $V_{\rm eff} = V/|u(\boldsymbol{r})|^2$. The lowest possible value $V_{\rm eff} \simeq \lambda^3$ is obtained for ground modes of a closed resonator. For an atom located at the waist of an open Fabry–Perot cavity with length L, it is much larger. Special limiting cases for concentric and confocal cavities are $V_{\rm eff}^{\rm conc} = \lambda^2 L(R/D)$ and $V_{\rm eff}^{\rm conf} = \lambda L^2/2\pi$, respectively, where (R/D) gives the ratio of mirror radius to cavity diameter.

At resonance, the atomic decay rate Γ_μ grows with Q_μ, whereas the resonator damping time constant κ_μ is reduced. Eventually, the energy of the atomic radiation field is stored for such a long time that reabsorption becomes possible. Perturbative Weisskopf–Wigner theory is no longer valid in this good cavity limit, which is separated from the regime of bad cavities by the more formal condition

$$\Gamma_{eg}^{\rm cav} > \kappa_\mu \ . \tag{79.25}$$

The strong coupling case is considered explicitly in Sect. 79.3.

Antenna Patterns Since the reflected radiation field of an atomic radiator is perfectly coherent with the source field, the combined radiation pattern modifies the usual dipole distribution of a radiating atom. The new radiation pattern can

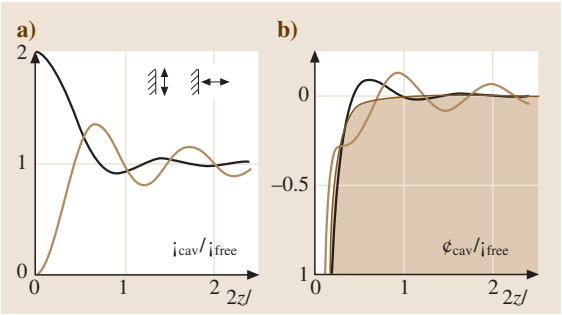

Figure 79.5: (a) Normalized rate of modified spontaneous emission in the vicinity of a perfectly reflecting wall for σ and π orientation of the radiating dipole. (b) Corresponding energy shift of the resonance frequency. *Shaded area* indicates contribution of static van der Waals interaction

be understood in terms of antenna arrays [16]. For a single atomic dipole in front of a reflecting mirror for example, one finds a quadrupole type pattern due to the superposition of a second, coherent image antenna. In some of the earliest experimental investigations on radiating molecules in cavities, modifications of the radiation pattern were observed [17].

79.2.4 Radiative Shifts and Forces

When the radiation field of an atom is reflected back onto its source, an energy or radiative shift is caused by the corresponding self polarization energy. An atom in the vicinity of a plane mirror (Fig. 79.5) again makes a simple model system. Since the energy shift depends on the atom wall separation z, it is equivalent to a dipole force $\boldsymbol{F}_{\rm dip}$ whose details depend on the role of retardation. Here we distinguish between the two cases where no radiation energy is exchanged between the atom and the field (van der Waals, Casimir forces) and where the atomic radiation causes forces by self-interference.

The Unretarded Limit: van der Waals Forces When the radiative round trip time $t_{\rm r} = 2z/c$ is short compared with the characteristic atomic revolution period $2\pi/\omega_{\rm eg}$, retardation is not important. In this quasistatic limit, van der Waals energy shifts for decaying atomic dipoles vary as z^{-3} with the atom–wall separation. Such a shift is also present for a nonradiating atom in its ground state. In perturbation theory, the van der Waals energy shift of an atomic level $|a\rangle$ is

$$\Delta_{\rm vdW} = -\frac{\langle a|q^2\left[(\boldsymbol{d}^2\cdot\widehat{\boldsymbol{x}}_{\rm t})^2 + 2(\boldsymbol{d}^2\cdot\widehat{\boldsymbol{z}})^2\right]|a\rangle}{64\pi\epsilon_0 z^3}\ . \tag{79.26}$$

Since the van der Waals force is anisotropic for electronic components parallel ($\widehat{\boldsymbol{z}}$) and perpendicular ($\widehat{\boldsymbol{x}}_{\rm t}$) to the mirror normal, the degeneracy of magnetic sublevels in an atom is lifted near a surface. The total energy shift is $\approx 1\,$kHz for a ground state atom at $1\,\mu$m separation, and very difficult to detect. However, the energy shifts grow as n^4 since the transition dipole moment scales as n^2. With Rydberg atoms, van der Waals energy shifts have been successfully observed in spectroscopic experiments [18].

The Retarded Limit: Casimir Forces At large separation, retardation becomes relevant, since the contributions of individual atomic oscilllation frequencies in (79.26) cancel by dephasing, thus reducing the $\Delta_{\rm vdW}$. A residual Casimir–Polder [19] shift may be interpreted as the polarization energy of a slowly fluctuating field with squared amplitude $\langle\mathcal{E}^2\rangle = 3\hbar c/64\epsilon_0 z^4$ originating from the vacuum field noise

$$\Delta_{\rm CP} = -\frac{1}{4\pi\epsilon_0}\frac{3\hbar c\alpha_{\rm st}}{8\pi z^4}\ , \tag{79.27}$$

where $\alpha_{\rm st}$ is the static electric polarizability. The vacuum field noise $\Delta_{\rm CP}$ replaces $\Delta_{\rm vdW}$ at distances larger than characteristic wavelengths, and is even smaller. Only indirect observations have been possible to date, relying on a deflection of polarizable atoms by this force [20, 21].

The Casimir–Polder force can also be regarded as an ultimate, cavity induced consequence of the mechanical action of light on atoms [22]. It is an example of the conservative and dispersive dipole force which is even capable of binding a polarizable atom to a cavity [23].

Radiative Self-Interference Forces Spontaneous emission of atoms in the vicinity of a reflecting wall also provides an example of cavity induced modification of the dissipative type of light forces, or radiation pressure. If the returning field is reabsorbed, the spontaneous emission rate is reduced and a recoil force directed away from the mirror is exerted. If the returning radiation field causes enhanced decay, a recoil towards the mirror occurs due to stimulated emission.

If the photon is detected at some angle with respect to the normal vector connecting the atom with the mirror surface, two paths for the photon are possible: It can reach a detector directly, or following a reflection off the wall. At small atom–mirror separation these paths are indistinguishable, the atom is thus left in a superposition of two recoil momentum states.

79.2.5 Experiments on Weak Coupling

Perhaps the most dramatic experiment in weak coupling cavity QED is the total suppression of spontaneous emission. For the experiments which have been carried out with Rydberg atoms and for a low-lying near infrared atomic transition [12, 13], it is essential to prepare atoms in a single decay channel. In addition, the atoms must be oriented in such a way that they are only coupled to a single decay mode (see the model waveguide in Fig. 79.4). This may be interpreted as an anisotropy of the electromagnetic vacuum, or as a specific antenna pattern.

An important problem in detecting the modification of radiative properties – changes in emission rates as well as radiative shifts – arises from their inhomogeneity due to the dependence on atom–wall separation. This difficulty has been overcome by controlling the atom–wall separation at microscopic distances through light forces [18], or by using well localized trapped ions [14, 15]. Furthermore, spectroscopic techniques that are only sensitive to a thin layer of surface atoms [24] have been used to clearly detect van der Waals shifts.

An atom emitting a radiation field in the vicinity of a reflecting wall will experience an additional dipole optical force caused by its radiation field. This force has been observed as a modification of the trapping force holding an ion at a fixed position with respect to the reflector [25].

Conceptually most attractive and experimentally most difficult to detect is the elusive Casimir interaction. Only for atomic ground states is this effect observable, free from other much larger shifts. The influence of the corresponding Casimir force on atomic motion has been observed in a variant of a scattering experiment, confirming the existence of this force in neutral atoms [20, 21].

The success of this experiment shows that spectroscopic techniques involving the exchange of photons are not suitable for the Casimir problem. A notable exception could be Raman spectroscopy of the magnetic substructure in the vicinity of a surface. In general, scattering or atomic interferometry experiments are more promising methods. The experiment by *Brune* et al. [26] may be interpreted in this way.

79.2.6 Cavity QED and Dielectrics

There are two variants of dielectric materials employed to study light-matter interaction in confined space: Conventional materials such as glass or sapphire, and artificial materials called photonic materials or metamaterials.

While dielectric materials are theoretically more difficult to treat than perfect mirrors, since the radiation at least partially enters the

medium, they have a similar influence on radiative decay processes. One new aspect is, however, the coupling of atomic excitations to excitations of the medium, which was observed for the case of a surface-polariton in [27].

Cavities with dimensions comparable to the wavelength promise the most dramatic modification of radiative atomic properties, but micrometer sized cavities for optical frequencies with highly reflecting walls are difficult to manufacture. So-called whispering gallery modes of spherical microcavities [28] have been intensely studied, but no simple way of coupling atoms to these resonator modes has been found yet.

On the other hand, dielectric materials with a periodic modulation of the index of refraction may exhibit photonic bandgaps in analogy with electronic bandgaps in periodic crystals [29, 30]. Electronic phenomena of solid state physics can then be transferred to photons. For example, excited states of a crystal dopant or a quantum dot cannot radiate into a photonic bandgap, the radiation field cannot propagate, and the excitation energy remains localized. The bandgap behaves like an empty resonator, and if a resonator structure is integrated into the device, the regime of strong coupling [31, 32] can be achieved with such photonic structures. An overview of suitable systems can be found in [33].

79.3 Strong Coupling in Cavity QED

Strong coupling of atoms and fields is realized in a good cavity when $\Gamma_\mu < \Gamma_{eg}$ (79.25). The Hilbert space of the combined system is then the product space of a single two-level atom and the countable set of Fock-states of the field,

$$\mathcal{H} = \mathcal{H}_{\text{atom}} \otimes \mathcal{H}_{\text{field}} \,, \tag{79.28}$$

which is spanned by the states

$$|n; a\rangle = |n\rangle|a\rangle \,. \tag{79.29}$$

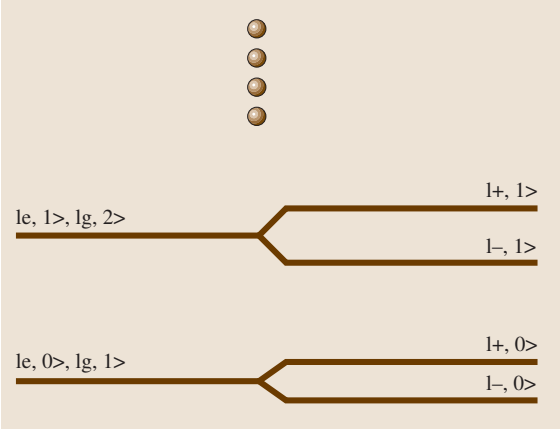

Figure 79.6: Level diagram for the combined states of noninteracting atoms and fields (a) which are degenerate at resonance. Degeneracy is lifted by strong coupling of atoms and fields (b) yielding new *dressed* eigenstates

The interaction of a single cavity mode with an isolated atomic resonance is now characterized by the Rabi nutation frequency, which gives the exchange frequency of the energy between atom and field. For an amplitude $\mathcal{E}$ corresponding to n photons,

$$\Omega(n) = g_\mu \sqrt{n+1} \,. \tag{79.30}$$

This is the simplest possible situation of a strongly coupled atom–field system. The new energy eigenvectors are conveniently expressed in the dressed atom model [34]:

$$\begin{aligned} |+, n\rangle &= \cos\theta |g, n+1\rangle + \sin\theta |e, n\rangle \,, \\ |-, n\rangle &= -\sin\theta |g, n+1\rangle + \cos\theta |e, n\rangle \,, \end{aligned} \tag{79.31}$$

with $\tan 2\theta = 2g_\mu\sqrt{n+1}/(\omega_0 - \omega_\mu)$. The separate energy structures of free atom and empty resonator are now replaced by the combined system of Fig. 79.6. At resonance, the new eigenstates are separated by $2\hbar\Omega_{\text{R}}$, where $\Omega_{\text{R}} = g_\mu$ is the vacuum Rabi frequency.

79.3.1 The Jaynes-Cummings Model

In a microscopic laser, simple atoms are strongly coupled to a single mode of a resonant or near resonant radiation field. Collecting atomic and field operators from (79.2), (79.10), and (79.14), this situation is described by the Jaynes–Cummings model Hamiltonian (79.15) [40, 41]

$$\begin{aligned}\mathcal{H}_{\rm JC} &= \mathcal{H}_{\rm atom} + \mathcal{H}_{\rm field} + \mathcal{H}_{\rm RWA} \\ &= \frac{1}{2}\hbar\omega_0\sigma_z + \hbar\omega_\mu a_\mu^\dagger a_\mu \\ &\quad + \hbar\left(g_\mu\sigma_+ a_\mu + g_\mu^* a_\mu^\dagger\sigma_-\right) \ .\end{aligned} \tag{79.32}$$

The JC model (79.32) represents the most basic and, at the same time, the most informative model of strong coupling in quantum optics. It consists of a single two-level atom interacting with a single mode of the quantized cavity field. The time evolution of the system is determined by

$$\mathrm{i}\hbar\frac{\partial\psi}{\partial t} = H\psi \ . \tag{79.33}$$

This model can be solved exactly due to the existence of the additional constant of motion

$$N = a^\dagger a + \sigma_z + 1 \ , \tag{79.34}$$

i. e., conservation of the *number of excitations*. Its eigenvalues are the integers N which are twofold degenerate except for $N = 0$. The simultaneous eigenstates of H and N are the pairs of dressed states defined in (79.31) which are not degenerate with respect to the energy H. The initial state problem corresponding to (79.33) is solved by elementary methods in terms of the expansion

$$|\Psi(t)\rangle = \sum_{n=0}^{\infty}\sum_{j=1}^{2} C_n^j(t)|n,j\rangle \ , \tag{79.35}$$

where the expansion coefficients are

$$\begin{aligned}C_n^1(t) = \Bigg(&C_n^1(0)\left\{\cos[\Omega(n)t] - \mathrm{i}\frac{\delta}{2\Omega(n)}\sin[\Omega(n)t]\right\} \\ &- \mathrm{i}\frac{\sqrt{n}g_\mu}{\Omega(n)}C_{n-1}^2(0)\sin[\Omega(n)t]\Bigg) \\ &\times\exp\left[-\mathrm{i}\omega_\mu\left(n-\frac{1}{2}\right)t\right]\end{aligned} \tag{79.36}$$

and

$$\begin{aligned}C_n^2(t) = \Bigg(&C_n^2(0)\Bigg\{\cos[\Omega(n+1)t] \\ &+ \mathrm{i}\frac{\delta}{2\Omega(n+1)}\sin[\Omega(n+1)t]\Bigg\} \\ &- \mathrm{i}\frac{g_\mu\sqrt{n+1}}{\Omega(n+1)}C_{n+1}^1(0)\sin[\Omega(n+1)t]\Bigg) \\ &\times\exp\left[-\mathrm{i}\omega_\mu\left(n+\frac{1}{2}\right)t\right] \ ,\end{aligned} \tag{79.37}$$

with $\delta = \omega_\mu - \omega_0$ the detuning between the atom and cavity and $\Omega(n) = \frac{1}{2}(\delta^2 + 4g_\mu^2 n)^{1/2}$ is the generalized Rabi frequency. The coefficients $C_n^j(0)$ are determined by the initial preparation of atom and cavity mode. The result simplifies considerably for $\delta = 0$ to

$$\begin{aligned}|\Psi(t)\rangle = \sum_{m=0}^{\infty}\Big\{&C_m^1(0)\,\mathrm{e}^{-\mathrm{i}\omega_\mu(m-1/2)t} \\ &\times\left[\cos\left(g_\mu\sqrt{m}t\right)|m;1\rangle\right. \\ &\left.-\,\mathrm{i}\sin\left(g_\mu\sqrt{m}\,t\right)|m-1;2\rangle\right] \\ &+ C_m^2(0)\,\mathrm{e}^{-\mathrm{i}\omega_m u(m+1/2)t} \\ &\times\left[\cos\left(g_\mu\sqrt{m+1}\,t\right)|m;2\rangle\right. \\ &\left.-\,i\sin\left(g_\mu\sqrt{m+1}t\right)|m+1;1\rangle\right]\Big\} \ .\end{aligned} \tag{79.38}$$

The coefficients $C_n^j(0)$ represent any initial state of the system, from uncorrelated product states to entangled states of atom and field. There exist numerous generalizations of this model which

include more atomic levels and several coherent fields.

79.3.2 Fock States, Coherent States and Thermal States

We now illustrate the properties of the Jaynes–Cummings model by specifying the initial state. Assume that the atom and field are brought into contact at time $t = 0$ and that all correlations that might exist due to previous interactions are suppressed.

Rabi Oscillations If the atom is initially in the excited state and the field contains precisely m quanta, then

$$C_n^j(t=0) = \delta_{n,m}\delta_{j,2} \; . \tag{79.39}$$

The solution of (79.33) assumes the form

$$\begin{aligned} |\Psi(t)\rangle = \mathrm{e}^{-\mathrm{i}\omega_\mu(m+1/2)t}\big[\cos\big(g_\mu\sqrt{m+1}\,t\big)|m;2\rangle \\ - i\sin\big(g_\mu\sqrt{m+1}\,t\big)|m+1;1\rangle\big] \; . \end{aligned} \tag{79.40}$$

The occupation probabilities of the atomic states evolve in time according to

$$n_2(t) = \langle\Psi(t)|2\rangle\langle 2|\Psi(t)\rangle = \cos^2\big(g_\mu\sqrt{m+1}\,t\big) \; , \tag{79.41}$$

$$n_1(t) = \langle\Psi(t)|1\rangle\langle 1|\Psi(t)\rangle = \sin^2\big(g_\mu\sqrt{m+1}\,t\big) \; . \tag{79.42}$$

The photon number and its variance are

$$\langle n(t)\rangle = \big\langle\Psi(t)a^\dagger a\Psi(t)\big\rangle = m + \sin^2\big(g_\mu\sqrt{m+1}\,t\big) \; , \tag{79.43}$$

$$\begin{aligned} \langle\Delta^2 n\rangle &= \big\langle\Psi(t)\big(a^\dagger a - \langle a^\dagger a\rangle\big)^2\Psi(t)\big\rangle \\ &= \frac{\sin^2\big(2g_\mu\sqrt{m+1}\,t\big)}{4} \; . \end{aligned} \tag{79.44}$$

In the limit of large m, $g_\mu\sqrt{m+1}$ is proportional to the field amplitude and the classical Rabi oscillations in a resonant field are recovered. The nonclassical features of the states are characterized by Mandel's parameter

$$Q_\mathrm{M} = \frac{\big\langle\Delta^2 n\big\rangle - \langle n\rangle}{\langle n\rangle} \geq -1 \; . \tag{79.45}$$

For the present example,

$$Q_\mathrm{M} = -1 + \frac{1}{4}\frac{\sin^2\big(2g_\mu\sqrt{m+1}\,t\big)}{m + \sin^2\big(g_\mu\sqrt{m+1}\,t\big)} \; . \tag{79.46}$$

$Q_\mathrm{M} \geq 0$ indicates the classical regime, while $Q \leq 0$ can only be reached by a quantum process.

The Coherent State Consider the case where the field is initially prepared in a coherent state

$$|\alpha\rangle = \exp\big(\alpha a^\dagger - \alpha^* a\big)|0\rangle = \mathrm{e}^{-|\alpha|^2/2}\sum_{n=0}^{\infty}\frac{\alpha^n}{\sqrt{n!}}|n\rangle \; , \tag{79.47}$$

while the atom starts from the excited state

$$C_n^j(0) = \mathrm{e}^{-|\alpha|^2/2}\frac{|\alpha|^n}{\sqrt{n!}}\delta_{j,2} \; . \tag{79.48}$$

In this case, the general solution specializes to

$$\begin{aligned} |\Psi(t)\rangle = \sum_{n=0}^{\infty}\frac{\alpha^n}{\sqrt{n!}}\mathrm{e}^{-\mathrm{i}\omega(n+1/2)t}\,\mathrm{e}^{-|\alpha|^2/2} \\ \times\big[\cos\big(g_\mu\sqrt{n+1}\,t\big)|n;2\rangle \\ - i\sin\big(g_\mu\sqrt{n+1}\,t\big)|n+1;1\rangle\big] \; , \end{aligned} \tag{79.49}$$

and the occupation probability of the excited state is

$$n_2(t) = \frac{1}{2}\left[1 + \sum_{n=0}^{\infty}\frac{|\alpha|^{2n}}{n!}\,\mathrm{e}^{-|\alpha|^2}\cos\big(2g_\mu\sqrt{n+1}\,t\big)\right] \; . \tag{79.50}$$

From here, detailed quantitative results can only be obtained by numerical methods [42]. However, if the coherent state contains a large number of photons $|\alpha|^2 \gg 1$, the essential dynamics

can be determined by elementary methods. Initially, the population oscillates with the Rabi frequency $\Omega_1 \approx g_\mu|\alpha|$, which is proportional to the average amplitude of the field, as expected from its classical counterpart. With increasing time, the coherent oscillations tend to cancel due to the destructive interference of the different Rabi frequencies in the sum:

$$n_2(t) = \frac{1}{2}\left[1 + \cos(2g_\mu\,|\alpha|\,t)\,\mathrm{e}^{-(gt)^2/2}\right] . \tag{79.51}$$

However, strictly aperiodic relaxation of $n_2(t)$ is impossible since the exact expressions, (79.35) and (79.36), represent a quasiperiodic function which, given enough time, approaches its initial value with arbitrary accuracy.

For short times, the oscillating terms in the sum cancel each other due to the slow evolution of their frequency with n. However, consecutive terms interfere constructively for larger times t_r, such that the phases satisfy

$$\phi_{n+1}(t_\mathrm{r}) - \phi_n(t_\mathrm{r}) = 2\pi . \tag{79.52}$$

For $|\alpha|^2 \gg 1$, the increment of the arguments is

$$\phi_{n+1} - \phi_n = g_\mu t_\mathrm{r}/|\alpha| , \tag{79.53}$$

and therefore the first revival of the Rabi oscillations occurs approximately at $t_\mathrm{r} = \pi|\alpha|/g_\mu$. A clear distinction of Rabi oscillation, collapses, and revivals requires a clear separation of the three time scales

$$t_1 \ll t_2 \ll t_3 , \tag{79.54}$$

where $t_1 \approx (g_\mu|\alpha|)^{-1}$ for Rabi oscillation, $t_2 \approx g_\mu^{-1}$ for collapse, and $t_3 \approx |\alpha|/g_\mu$ for revival.

The discovery of collapse and revival of Rabi oscillations is one of the key demonstration of photons [42, 43, 44]. The typical features of the transient evolution starting from a coherent state are shown in Fig. 79.7. With time increasing even further, revivals of higher order occur which spread in time, and finally can no longer be separated order by order. It is also proposed

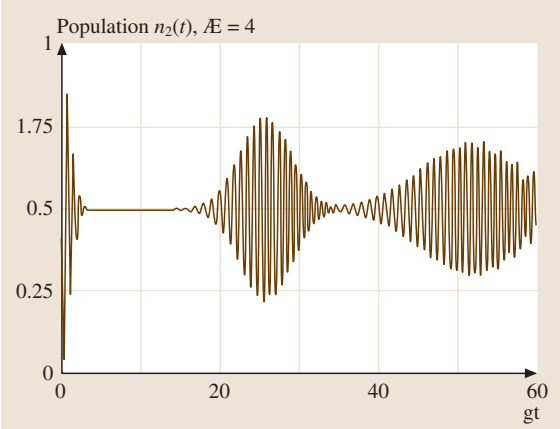

Figure 79.7: Rabi oscillations, dephasing, and quantum revival

that by carefully manipulating the initial states and atom-light coupling during evolution, arbitrary Fock states can be created with prechosen evolution time [45].

The Thermal State Consider a microwave resonator brought into thermal contact with a reservoir, inducing loss on a time scale κ^{-1} and thermal excitation. The dissipative time evolution is described by the master equation

$$\begin{aligned}\dot\rho &= (L_0 + L)\rho \\ &\equiv \mathrm{i}[H,\rho]/\hbar + \kappa(n_\mathrm{th}+1)\big\{\big[a,\rho a^\dagger\big] + \big[a\rho, a^\dagger\big]\big\} \\ &\quad + \kappa n_\mathrm{th}\big\{\big[a^\dagger,\rho a\big] + \big[a^\dagger\rho, a\big]\big\} ,\end{aligned} \tag{79.55}$$

where $n_\mathrm{th} = [\exp(\beta\hbar\omega) - 1]^{-1}$, at $T = k_\mathrm{B}\beta^{-1}$, is the equilibrium population of the cavity mode, L_0 symbolizes the unitary evolution according to the Jaynes–Cummings dynamics and L is a dissipation term.

The solution of this model can be expressed in terms of an eigenoperator expansion of the equation

$$L\rho = -\lambda\rho . \tag{79.56}$$

The eigenvalues λ that determine the relaxation rates, as well as the eigenoperators, are known

in closed form for the case of vanishing temperature [46]. Since energy is exchanged between the nondecaying atom and the decaying cavity mode, cavity damping is modified in a characteristic way due to the presence of the atom. The technical details can be found in [47].

79.3.3 Vacuum Splitting

In the classical case, the eigenvalues of the interaction free Hamiltonian are degenerate at resonance. The atom–field interaction splits the eigenvalues and determines the Rabi frequency of oscillation between the two states. One consequence is the existence of side bands in the resonance fluorescence spectrum [48]. In the quantum case, the field itself is treated as a quantized dynamical variable determined from a self-consistent solution for the complete system of atom plus field. The vacuum Rabi frequency $\Omega_{\mathrm{vac}} = g_\mu$ remains finite, and accounts for the spontaneous emission of radiation from an excited atom placed in a vacuum. In the limiting case of a single atom interacting with the quantized field, the photon number n can only change by ± 1, and the population oscillates with the frequency $\Omega(n)$ given by (79.30). For an ensemble of N atoms, n can in principle change by up to $\pm N$. However, if the field and atoms are only weakly excited, the collective frequency of the ensemble is determined by the linearized Maxwell–Bloch equations. The eigenfrequencies are given by

$$\lambda^{\pm} = \frac{1}{2}\left[\mathrm{i}(\gamma_\perp + \kappa) \pm \sqrt{4g_\mu^2 N - (\gamma_\perp - \kappa)^2}\right] , \tag{79.57}$$

where $\gamma_\perp^{-1}$ is the phase relaxation time of the atom and κ^{-1} the decay time of the resonator. This is the polariton dispersion relation in the neighborhood of the polariton gap. The spectral transmission

$$T(\omega) = T_0 \left| \frac{\kappa[\gamma + \mathrm{i}(\omega_0 - \omega)]}{(\omega - \lambda^+)(\omega - \lambda^-)} \right|^2 \tag{79.58}$$

of an optical cavity containing a resonant atomic ensemble of N atoms reveals the internal dynamics of the coupled system and a splitting of the resonance line occurs. T_0 is the peak transmission of the empty cavity. The splitting increases either with the number of photons, approaching $\sqrt{n+1}$ in the presence of a single atom, or with the number of atoms, approaching $\sqrt{N}$ in the resonator when the field is weak. The latter case is demonstrated in Fig. 79.8 [35] for an optical resonator with $1-10$ atoms interacting with a field that contains, on average, much less than a single photon.

79.3.4 Strong Coupling in Experiments

In order to achieve strong coupling experimentally, it is necessary to use a high-Q resonator in combination with a small effective mode volume. This condition was first realized for ground modes of a closed microwave cavity [8], and later also for open cavity optical resonators (Fig. 79.6) [35]. It is interesting to control the interaction time of the atoms with the cavity field. In earlier experiments, this was typically achieved by selecting the passage time for an atom transiting the cavity. The advancement of atom trapping methods has also led to the observation of a truly one-atom laser at optical frequencies [36].

More recently, this situation has also been realized for artificial atoms including superconducting systems [37, 38] and quantum dots [31, 32].

Rydberg Atoms and Microwave Cavities At microwave frequencies, very low loss superconducting niobium cavities are available with $Q \approx 10^{10}$. Resonator frequencies are typically several tens of GHz and can be matched by atomic dipole transitions between two highly excited Rydberg states. By selective field ionization, the excitation level of Rydberg atoms can be detected, and hence it is possible to measure

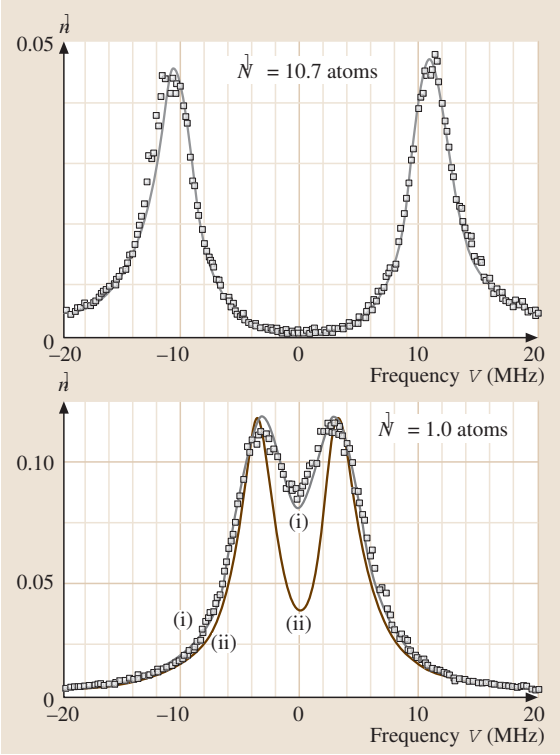

Figure 79.8: Intracavity photon number (measured from a transmission experiment, [35]) as a function of probe frequency detuning, and for two values of N, the average number of atoms in the mode. *Thin lines* give theoretical fits to the data, including atomic number and position fluctuations. *Curve (ii)* in the *lower graph* is for a single intracavity atom with optimal coupling g_μ

whether a transition between the levels involved has occurred. The efficiency of this method approaches unity, so that experiments can be performed at the single atom level. The interaction or transit time T is usually much shorter than the lifetime $\tau_{\rm Ry}$ of the Rydberg states involved. For this reason, circular Rydberg states with quantum numbers $l = m = n - 1$ are particularly suitable.

Rydberg atoms [39] are prepared in an atomic beam, selectively excited to an upper level, and then sent through a microwave cavity where the upper and lower levels are coupled by the electromagnetic field. If the atom is detected in the lower of the coupled levels as it leaves the resonator, the excitation energy has been stored in the resonator field. Thus the evolution of the resonator field is recorded as a function of the atomic interaction.

A microwave cavity in interaction with a single or a few Rydberg atoms is called a micromaser (formerly a one atom maser) [8]. The experimental conditions may be summarized as

$$g_\mu > 1/T > 1/\tau_{\rm Ry} > \kappa_\mu \ . \tag{79.59}$$

Strong Coupling in Open Optical Cavities At optical wavelengths, a cavity with small $V_{\rm eff}$ in (79.24) is clearly more difficult to construct than at centimeter wavelengths. However, dielectric coatings are now available which allow very low damping rates ω_μ/Q_μ for optical cavities. Very high finesse $\mathcal{F} \simeq 10^7$ (which is a more convenient measure for the damping rate of an optical Fabry–Perot interferometer) has been achieved. By reducing the volume of such a high-Q cavity mode, strong coupling of atoms and fields at optical frequencies has been demonstrated [35].

In open structures, the atoms can still decay into the continuum states with a rate γ. Therefore the condition for strong coupling in such systems is usually given as

$$\frac{g_\mu^2}{\kappa_\mu \gamma} > 1 \ . \tag{79.60}$$

79.4 Micromasers

Sustained oscillations of a cavity mode in a microwave resonator can be achieved by a weak beam of Rydberg atoms excited to the upper level of a resonant transition. For a cavity with a $Q \approx 10^{10}$, much less than a single atom at a time, on average, suffices to balance the cavity

losses. Operation of a single atom maser has been demonstrated [8]. The atoms enter the cavity at random times, according to the Poisson statistics of a thermal beam, and interact with the field only for a limited time. In order to restrict the fluctuations of the atomic transit time, the velocity spread is reduced. This is achieved either by Fizeau chopping techniques, or by making use of Doppler velocity selection in the initial laser excitation process. Since most of the time no atom is present, it is natural to separate the dynamics into two parts [49]:

1. For the short time while an atom is present, the state evolves according to the Jaynes–Cummings dynamics, where H is defined in (79.32),

$$\dot{\rho}(t) = \mathrm{i}[H, \rho]/\hbar \; , \tag{79.61}$$

and damping can safely be neglected. The formal solution is abbreviated by $\rho(t) = F(t - t_0)\rho(t_0)$.

2. During the time interval between successive atoms, the cavity field relaxes freely toward the thermal equilibrium according to (79.55) with $L_0 = 0$:

$$\dot{\rho}(t) = L\rho \; , \tag{79.62}$$

with the formal solution $\rho(t) = \exp[L(t - t_0)]\rho(t_0)$.

The time development of the micromaser therefore consists of an alternating sequence of unitary $F(t)$ and dissipative $\mathrm{e}^{(Lt)}$ evolutions. Atoms enter the cavity one by one at random times t_i. Until the next atom enters at time t_{i+1}, the evolution t_i is given by

$$\rho(t_{i+1}) = \exp(Lt_p)F(\tau)\rho(t_i) \; , \tag{79.63}$$

where $t_p = t_{i+1} - t_i - \tau$, and τ is the transit time. If $\tau \ll t_{i+1} - t_i$ on average, then $t_p \approx t_{i+1} - t_i$. After averaging (79.63) over the Poisson distribution $P(t) = R\exp(-Rt_p)$ for t_p, where R is the injection rate, the mean propagator from atom to atom is

$$\langle\rho(t_{i+1})\rangle = \frac{R}{R - L}F(\tau)\langle\rho(t_i)\rangle \; . \tag{79.64}$$

After excitation, the reduced density matrix of the field alone becomes diagonal after several relaxation times κ^{-1}:

$$\langle n|\mathrm{Tr}_{\mathrm{atom}}(\rho)|m\rangle = P_n\delta_{n,m} \; . \tag{79.65}$$

Due to the continuous injection of atoms, the field never becomes time independent, but may relax toward a stroboscopic state defined by

$$\langle\rho(t_{i+1})\rangle = \langle\rho(t_i)\rangle \; . \tag{79.66}$$

The state of the cavity field can be determined in closed form by iteration:

$$P_n = N\prod_{k=1}^{n}\frac{n_{\mathrm{th}}\kappa + A_k}{(n_{\mathrm{th}} + 1)\kappa} \; , \tag{79.67}$$

where N guarantees normalization of the trace and $A_k = (R/n)\sin^2(g_\mu\tau\sqrt{n})$, and exact resonance between cavity mode and atom is assumed. Since all off-diagonal elements vanish in steady state, (79.67) provides a complete description for the photon statistics of the field.

79.4.1 Maser Threshold

The steady state distribution determines the mean photon number of the resonator as a function of the operating conditions:

$$\langle n\rangle = \sum_{n=0}^{\infty} nP_n \; . \tag{79.68}$$

A suitable dimensionless control parameter is

$$\Theta = \frac{1}{2}g_\mu\tau\sqrt{R/\kappa} \; . \tag{79.69}$$

For $\Theta \ll 1$, the energy input is insufficient to counterbalance the loss of the cavity, effectively resulting in a negligible photon number. With increasing pump rate R, a threshold is reached

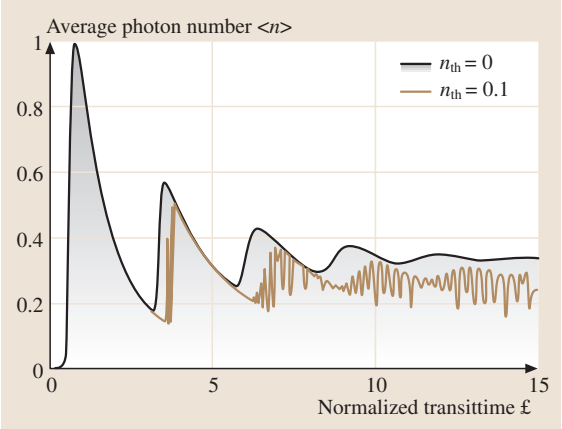

Figure 79.9: Average photon number as a function of the normalized transit time defined by (79.69)

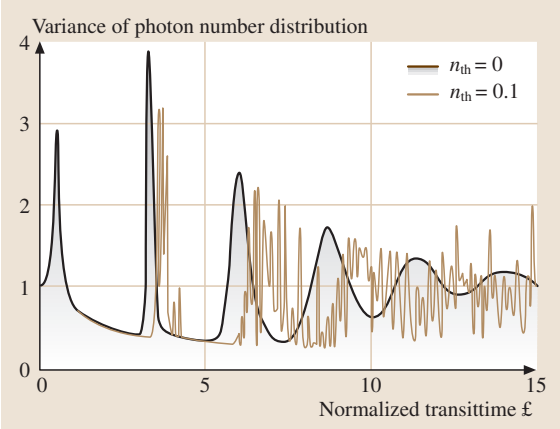

Figure 79.10: Variance normalized on the average photon number $\sigma^{2<n>}/\langle\sigma\rangle$. Values below unity indicate regions of nonclassical behavior

at $\Theta \simeq 1$, where $\langle n\rangle$ increases rapidly with R. In contrast to the behavior of the usual laser, the single atom maser displays multiple thresholds with a sequence of minima and maxima of $\langle n\rangle$ as a function of Θ [50]. This can be related to the rotation of the atomic Bloch vector. When the atom undergoes a rotation of about π during the transit time τ, a maximum of energy is transferred to the cavity and $\langle n\rangle$ is maximized. The converse applies if the average rotation is a multiple of 2π. This behavior is shown in Fig. 79.9. The minima in $\langle n\rangle$ are at $\Theta \simeq 2n\pi$.

79.4.2 Nonclassical Features of the Field

Fluctuations can be of classical or of quantum origin. The variance of the photon number

$$\sigma^2 = \left(\langle n^2\rangle - \langle n\rangle^2\right) \qquad (79.70)$$

is a measure of the randomness of the field intensity. Classical Poisson statistics require that $\sigma^2 \geq \langle n\rangle$. A value below unity indicates quantum behavior, which has no classical analog. In Fig. 79.10, the variance is plotted as a function of Θ. Regions of enhanced fluctuations $\sigma^2 > \langle n\rangle$ alternate with regions with sub-Poissonian character $\sigma^2 < \langle n\rangle$ [51]. When $\langle n\rangle$ approaches a local maximum it is accompanied by large fluctuations, while at points of minimum field strength the fluctuations are reduced below the classical limit. This feature is repeated with a period of $\Theta \simeq 2\pi$, but finally washes out at large values of Θ.

The large variance of n is caused by a splitting of the photon distribution P_n into two peaks, which gives rise to bistability in the transient response [52]. The sub-Poissonian behavior of the field is reflected in an increased regularity of the atoms leaving the cavity in the ground state.

79.4.3 Trapping States

If cavity losses are neglected, operating conditions exist which lead directly to nonclassical, i. e., Fock states. If the cavity contains precisely n_q photons, an atom that enters the resonator in the excited state leaves it again in the same state provided the condition [53]

$$g_\mu \tau \sqrt{n_q + 1} = 2q\pi \qquad (79.71)$$

is satisfied, i. e., the Bloch vector of the atom undergoes q complete rotations. Such a photon

Fock state $|n_q\rangle$ is referred as trapping state in the literature of maser. Note that the same term is also used in other contexts with very different definitions. If the maser happens to reach a trapping state $|n_q\rangle$, the photon number n_q can no longer increase irrespective of the flux of pump atoms. With the inclusion of cavity damping at zero temperature, n_q still represents an upper barrier that cannot be overcome, since damping only causes downward transitions. Even in the presence of dissipation, generalized trapping states exist with a photon distribution that vanishes for $n > n_q$ and has a tail towards smaller photon numbers $n \leq n_q$. However, thermal fluctuations at finite temperatures destabilize the trapping states since they can momentarily increase the photon number and allow the distribution to jump over the barrier $n = n_q$. Nevertheless, even for $n_{\rm th} < 10^{-7}$, remnants of the trapping behavior persist, and can be seen in the transient response of the micromaser (Sect. 79.4.4).

79.4.4 Atom Counting Statistics

Direct measurements of the field in a single atom maser resonator are not possible because detector absorption would drastically degrade its quality. However, the field can be deduced from the statistical signature of the atoms leaving the resonator.

The probability $P(n)$ of finding n atoms in a beam during an observation interval t is given by the classical Poisson distribution

$$P(n) = (Rt)^n \, \mathrm{e}^{-Rt}/n! \; . \tag{79.72}$$

Information on the field inside is then revealed by the conditional probability $W(n, |g\rangle, m, |e\rangle, T)$ of finding n atoms in the ground state and m atoms in the excited state during a time t. Since there are only two states, it is sufficient to determine the probability

$$W(n, |g\rangle, t) = \sum_{m=0}^{\infty} W(n, |g\rangle, m, |e\rangle, t) \tag{79.73}$$

for being in the ground state [54]. For $n = 0$, the probability of observing no atom in the ground state during the period t is

$$W(0, |g\rangle, t) = \mathrm{Tr}(\rho_{\rm stst}) \exp\{L + R[O_{|g\rangle} + (1-\eta)O_{|e\rangle} - 1]t\} \; , \tag{79.74}$$

where $O_{|j\rangle} = \langle j|F(\tau)|j\rangle$ (79.61) and $\rho_{\rm stst}$ is the steady state of the maser field. This probability is closely related to the waiting time statistic $P_2(0, |g\rangle, t)$ between two successive ground state atoms, a property which is easily determined in a start-stop experiment. For an atom detector with finite quantum efficiency η for state selective detection, the waiting time probability is

$$\begin{aligned} &P_2(0, |g\rangle, t) \\ &= \big\{ \mathrm{Tr}(\rho_{\rm stst}) O_{|g\rangle} \\ &\quad \times \exp[L + R[O_{|g\rangle} + (1-\eta)O_{|e\rangle} - 1]T] O_{|g\rangle} \big\} \\ &\quad \big/ \big[\mathrm{Tr}(\rho_{\rm stst}) O_{|g\rangle} \big]^2 \; . \end{aligned} \tag{79.75}$$

How a specific field state is reflected in the atom counting statistics will be illustrated for two situations: the region of sub-Poisson statistics and the region where the trapping condition is satisfied. Increased regularity of the cavity field $Q_{\rm M} \leq 0$ manifests itself in increased regularity of ground state atoms in the beam. The statistical behavior exhibits *anti-bunching*, i. e., $P_2(0, |g\rangle, t)$ has a maximum at finite t, indicating *repulsion* between successive atoms in comparison with a Poissonian beam. If the transit time τ is chosen in such a way that $g\tau \simeq 2\pi$, the chance of observing an initially excited atom in the ground state is negligible. At some point, however, an unlikely thermal fluctuation occurs, adding a photon. The rotation angle of the Bloch vector suddenly increases to $2\pi\sqrt{2} \simeq 3\pi$, and the atoms tend to leave the cavity in the ground state. After a typical cavity lifetime, the field decays and the trapping condition is restored again. Under this operation condition, the statistics of ground state atoms is governed by two time constants:

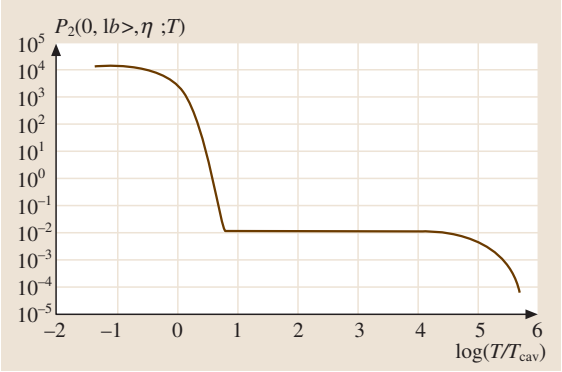

Figure 79.11: Waiting time probability for atoms in the ground state while cavity is operated at vacuum trapping-state condition

1. a short interval, in which successive atoms leave the cavity in the ground state after a thermal fluctuation;

2. a long time interval, in which the trapping condition is maintained and all atoms leave the resonator in their excited state until the next fluctuation occurs.

The probability $P_2(0, |g\rangle, t)$ is plotted in Fig. 79.11. The plot clearly shows the two time regimes that govern the imperfect trapping situation.

79.5 Cavity Cooling

In previous sections, we present some important aspects of cavity QED by examining the effect of coupling between a single cavity photon and the atomic (pseudo-)spin degree of freedom. However, an experimental realization and a perfect control of such coupling requires very cold atoms trapped at a specific position. Thus, the external degree of freedom associated with the kinetic motion of atoms needs to be taken into account to achieve a complete description of the system. As an example, the cavity modes can exert light forces on moving atoms, and induce significant effect in transmission spectroscopy measurement [55, 56, 57].

Another important example, and one of the most promising applications of the cavity QED dynamics involving atomic motion is the realization of cavity cooling, i.e., the dissipation of kinetic energy through the cavity photon loss channel in a controlled manner. The realization of cavity cooling has been proved to be an essential step for the experimental achievement of strongly coupled cavity QED systems with sufficiently long interaction times and precise control of atomic motion. In the weak coupling regime, the atom can be cooled by coupling with cavity photons if the pumping is red detuned with $\omega_p - \omega_C < 0$, in which case the average frequency of emitted photons is higher than that of the pumping laser due to the increase of mode density around the cavity frequency. The energy hence has to be compensated by the loss in kinetic energy of the atomic center-of-mass (CoM) motion. In the strong-coupling regime, however, the atom-light scattering process becomes complicated with the non-negligible photon reabsorption. For a high-finesse FP cavity, the dynamic cavity cooling effect in this case can be interpreted in the frequency domain with a Sisyphus-type mechanism using the dressed-state picture [58]. For the case of a ring cavity, the intuitive photon scattering picture can still be used but with a full velocity dependence of the radiation pressure [59].

79.5.1 Master Equation

As a simplest example, we consider a system of a single two-level atom trapped in a single mode optical cavity, which is driven by a monochromatic pumping laser. Under the dipole approximation and the RWA, the Hamiltonian of the system can be written as

$$\mathcal{H} = \mathcal{H}_{\rm GJC} + \mathcal{H}_{\rm CoM} + \mathcal{H}_{\rm pump} \,. \qquad (79.76)$$

The generalized Jaynes-Cummings (GJC) term is similar to the JC model in Eq. (79.15)

$$\begin{aligned}\mathcal{H}_{\rm GJC} =& \frac{1}{2}\hbar\omega_0(\mathbf{r})\sigma_z + \hbar\omega_C a^\dagger a \\ &+ \hbar\left[gf(\mathbf{r})\sigma_+ a + g^* f^*(\mathbf{r}) a^\dagger \sigma_-\right] ,\end{aligned} \tag{79.77}$$

where the atomic frequency $\omega_0(\mathbf{r})$ acquires explicit dependence on the CoM coordinate $\mathbf{r}$ of the atom owing to a differential AC-stark shift induced by a far-detuned external trapping potential exerted on the atom. Besides, the atom-photon coupling strength is spatially modulated with a function $f(\mathbf{r})$ according to the electric field strength of cavity mode. For a standing-wave mode in an FP cavity, the coupling modulates in magnitude with $f(\mathbf{r}) = \cos(kx)$, while for a propagating-wave mode in a ring cavity, the coupling modulates in phase with $f(\mathbf{r}) = e^{i\pi kx}$. In the both cases, the intracavity mode is assumed without loss of generality to be along the x direction. The motion of the atomic CoM degree of freedom is described by the term

$$\mathcal{H}_{\rm CoM} = \frac{\mathbf{p}^2}{2m} + V_{\rm trap}(\mathbf{r}) , \tag{79.78}$$

where m is the mass of the atom and $V_{\rm trap}(\mathbf{r})$ denotes the trapping potential. If pumped by a driving laser at frequency ω_p, the pumping Hamiltonian takes the form

$$\begin{aligned}\mathcal{H}_{\rm pump} =& i\hbar\eta(a^\dagger - a)e^{-i\omega_p t} \\ &+ i\hbar\Omega_p(\mathbf{r})e^{-i\omega_p t}(\sigma_+ - \sigma_-) ,\end{aligned} \tag{79.79}$$

where the first term describes a pumping laser applied along the cavity direction to couple the cavity mode with amplitude η, and the second corresponds to a driving directly on the atomic spin degree of freedom at a position-dependent Rabi frequency $\Omega_p(\mathbf{r})$.

The dynamics of the system can be described by the density operator ρ, which satisfies the master equation

$$\frac{d\rho}{dt} = -\frac{i}{\hbar}\left[\mathcal{H}, \rho\right] + \mathcal{L}_{\rm cav}\rho + \mathcal{L}_{\rm atom}\rho , \tag{79.80}$$

where the Liouville operators are introduced to describe the dissipation of cavity photons and atoms. If the environment is Markovian, this photon decay can be approximated by

$$\mathcal{L}_{\rm cav}\rho = -\kappa\left(a^\dagger a\rho + \rho a^\dagger a - 2a\rho a^\dagger\right) \tag{79.81}$$

with κ the cavity decay rate. Another decay channel of the system is the spontaneous decay of atom from the excited to the ground state, accompanied by the emission of a photon into the environment. This process takes the form

$$\begin{aligned}\mathcal{L}_{\rm atom}\rho =& -\gamma[\sigma_+\sigma_-\rho + \rho\sigma_+\sigma_- \\ &- 2\int d^2\hat{\mathbf{r}}_\perp h(\hat{\mathbf{r}}_\perp)\sigma_- e^{-ik_0 r_\perp}\rho e^{ik_0 r_\perp}\sigma_+] ,\end{aligned} \tag{79.82}$$

where γ is the spontaneous decay rate, $\hat{\mathbf{r}}_\perp$ is the directional unit vector in the transversal plane, $r_\perp = \mathbf{r}\cdot\hat{\mathbf{r}}_\perp$ is the projection, and $k_0 = \omega_0/c$ is the recoil wave vector of the atom. The function $h(\hat{\mathbf{r}}_\perp)$ is present to describe the directional distribution of spontaneous decay of specific atomic transition.

In general, it is not possible to solve the master equation (79.80) analytically even for a single atom. If the population of the atomic excited state is negligible, one can significantly simplify the Hamiltonian Eq. (79.76) by adiabatically eliminating the atomic excited state. This approximation is valid provided that the atomic transition between the two internal spin states is far detuned from the pumping laser, or has a large spontaneous decay rate. In either case, the atomic operator can be approximated as

$$\sigma_- \approx \frac{gf(\mathbf{r})a + \Omega_p(\mathbf{r})}{-i(\omega_p - \omega_0) + \gamma} . \tag{79.83}$$

By substituting the expressions of σ_- and $\sigma_+ = \sigma_-^\dagger$ back into the Hamiltonian Eq. (79.76), we obtain an effective Hamiltonian in which the CoM motion of the atom is coupled to the cavity

mode

$$\begin{aligned}\mathcal{H}_{\rm eff} = &\frac{\mathbf{p}^2}{2m} + V_{\rm trap}(\mathbf{r}) \\ &- \hbar\left[(\omega_p - \omega_C) - U_0|f(\mathbf{r})|^2\right] a^\dagger a \\ &+ \hbar\eta_{\rm eff}(\mathbf{r})\left[f^*(\mathbf{r})a^\dagger + f(\mathbf{r})a\right] ,\end{aligned} \tag{79.84}$$

where the position-dependent effective pumping strength is given by

$$\eta_{\rm eff}(\mathbf{r}) = \frac{(\omega_p - \omega_0) g\Omega_p(\mathbf{r})}{(\omega_p - \omega_0)^2 + \gamma^2} . \tag{79.85}$$

In this effective model, one can see clearly that the cavity photons provide a trapping potential $\hbar U_0|f(\mathbf{r})|^2 a^\dagger a$ to the atomic CoM motion with

$$U_0 = \frac{g^2(\omega_p - \omega_0)}{(\omega_p - \omega_0)^2 + \gamma^2} . \tag{79.86}$$

The gradient of this effective potential acts as a force exerted on the atom. This force acquires an explicit dependence on the amplitude of the cavity mode, which depends not only on the momentary position of the atom but has a memory effect owing to the finite decay rate κ. The force hence becomes velocity-dependent, which, in a semiclassical theory of atomic motion, leads to an effective viscous friction that can cool the atom.

79.5.2 Cavity Cooling Experiments

Cavity cooling of single atoms was first demonstrated with ^{85}Rb atoms trapped in an FP cavity [60]. In this experiment, the trapping field was red detuned with respect to the atom, while the cooling laser was a blue-detuned probing field with frequency $\omega_p > \omega_0$. From Eqs. (79.84) and (79.86), the interaction between the probing laser and the atom induces to a blueshift of the cavity frequency by an amount of $U_0|f(\mathbf{r})|^2$, which then leads to an increase of the energy stored in the cavity field with a cost of kinetic energy of the atoms. The cooling effect was demonstrated via the observation of extended storage times and improved localization of ^{85}Rb atoms from time-resolved measurement of the cavity transmission signal. As a result, a cooling rate of $\beta/m = 21$ kHz is achieved, which exceeds the estimated value of 4 kHz for blue-detuned Sisyphus cooling of a two-level atom in free space, or with the Doppler cooling rate of 1.5 kHz at equivalent atomic saturation.

With the advanced progresses of free-space laser cooling and trapping, other achievements have been obtained in the exploration and applications of single-atom cavity QED systems. These include the high-precision measurements demonstrated the basic cavity QED model in the optical domain [61, 62], the quantum anharmonic domain of the Jaynes-Cummings spectrum [63, 64], the generation of squeezed light [65], the development of a deterministic single-photon source [66, 67], the realization of the long-time sought atom-photon quantum interface [68, 69] and single-atom quantum memory [70], and the realization of electromagnetically induced transparency with a single atom [71].

79.6 Cavity QED for Cold Atomic Gases

Another new research direction in cavity QED is about the hybrid system of cold and ultracold atomic ensembles and high-finesse optical resonators. With the common coupling of atoms to the cavity field, there exits a long-range interatomic interaction mediated by coherent scattering of cavity photons, an ingredient which is usually absent in free-space cold atom experiments. As a result, this strongly interacting many-body system can present novel quantum phenomena with strong correlation. Besides, the coupling between the cavity mode and the atomic motion can induce a frequency shift of the cavity frequency and its backaction on mechanical motion, which may lead to a self organization of atoms and an implementation of cavity optome-

chanics.

79.6.1 Atomic Ensembles in a Cavity

The interatomic interaction in a cavity is mediated by the cavity mode by its direct coupling to the atomic electric-dipole moments. However, the nature is inherently different from the induced dipole-dipole interaction, i.e., the van der Walls interaction in free-space. In a cavity, the interaction strength does not decay with the interatomic separation and depends only on the local coupling of the atoms to the cavity field. More importantly, the interaction is a global coupling with the ensemble of atoms collectively coupling to the cavity field and experiencing the resulting backaction. Thus, even in cases where the interaction between a single atom and cavity mode is not strong enough, the collective interaction energy can still be enhanced coherently within an atomic ensemble. Next, we discuss the character of the cavity-mediated interatomic interaction in two different pumping geometries, namely, pumping the cavity either directly or indirectly via light scattering off the laser-driven atoms.

In the case of cavity pumping, the detuning between the driving laser and the dispersively shifted cavity resonance depends on the position of all atoms, which in turn experience the optical dipole force of the intracavity field. Under the adiabatic approximation with small atomic velocities and low saturation, the interaction potential among the ensemble of N atoms takes the form [73]

$$\begin{aligned} &V(\mathbf{r}_1,\ldots,\mathbf{r}_N) \\ &= \frac{\hbar(\omega_p-\omega_0)|\eta|^2}{(\omega_p-\omega_0)\kappa+(\omega_p-\omega_C)\gamma} \\ &\times \tan^{-1}\frac{\gamma\kappa-(\omega_p-\omega_0)(\omega_p-\omega_C+g_{\rm eff}^2)}{(\omega_p-\omega_0)\kappa+(\omega_p-\omega_C)\gamma}\,. \end{aligned} \tag{79.87}$$

The collective coupling strength $g_{\rm eff}$ depends on the spatial distribution of the N atoms. This cavity-mediated long-range interatomic interaction gives rise to an asymmetric deformation of the normal-mode splitting, which has been observed experimentally [74].

The situation drastically changes if the system is atom pumped by a driving laser from a direction perpendicular to the cavity axis. In this case, photons are Rayleigh scattered by atoms into the cavity mode. Photons scattered from different atoms will interfere either destructively or constructively depending on the relative positions of the atoms. Consider as a simple example of two atoms trapped in a cavity, if the two atoms are separated by odd integer multiples of the half-wavelength, the photons scattered into the cavity have the same magnitude but opposite sign, resulting in destructive interference and a vanishing cavity field intensity. On the other hand, if the two atoms are separated by even integer multiples of the half-wavelength, the photons scattered off the two atoms interfere constructively to yield a fourfold enhancement of the field intensity. This collective enhancement of scattering photons from multiple atoms is referred as superradiance [75, 76].

Approximately, in the limit of $U_0 \to 0$, the collective potential of the atomic ensemble reads

$$\begin{aligned} V(\mathbf{r}_1,\ldots,\mathbf{r}_N) &= \frac{\hbar(\omega_p-\omega_C)|\eta_{\rm eff}|^2}{(\omega_p-\omega_C)^2+\kappa^2} \\ &\times \left[\sum_{j=1}^{N}\cos(kx_j)\cos(kz_j)\right]^2 . \end{aligned} \tag{79.88}$$

Here, we assume the cavity mode and the pumping laser are both standing waves along the x and z directions, respectively. Notice that if one moves along the cavity direction over a wavelength, the potential varies from its maximal value to zero, leading to a contrast of unity regardless of the atom-cavity coupling constant g. This is in clear contrast to the case of cavity pumping, where the atoms cause only a small modulation of the cavity intensity as $g \to 0$. This observation suggests that significant many-

body effects can be encountered even in the weak-coupling regime in the atom pumping geometry.

The long-range interaction between atoms is the origin of various collective dynamical effects. As an example, a thermal cloud of cold atoms interacting with a single mode FP cavity shows a phase transition upon tuning the atomic pumping power P from a direction perpendicular to the cavity axis [77, 78]. For pumping power less than a critical value $P_{\rm cr}$, the atoms distribute uniformly to minimize its kinetic energy. The light scattered from atoms in different positions then interfere destructively and the average intensity of the cavity field is zero. When the pumping power $P > P_{\rm cr}$, however, the atoms arrange themselves to form a checkerboard pattern to compensate the long-range interaction energy, so that the light interfere constructively to achieve a macroscopic cavity field.

The self-organization of atoms in a transversally driven FP cavity was first demonstrated in 2003 [79]. In that experiment, a total of $N \approx 10^7$ Cs atoms prepared at a temperature of 6 μK are pumped by a strong enough red-detuned laser to achieve collective emission of light into the cavity. As a result, the emission rate exceeds the free-space single-atom Rayleigh scattering rate by a factor of up to 10^3, and the spatial configuration of atoms features a spontaneous symmetry breaking into either the odd or even sites of a checkerboard pattern, which is revealed by measuring π jumps in the phase of emitted cavity field relative to the pumping laser. In a ring-cavity with two propagating-wave modes, the self-organization of atoms are also observed with transverse pumping [80]. However, the system spontaneously breaks a continuous translational symmetry rather than a discrete $\mathbb{Z}_2$ symmetry as in the FP cavity.

79.6.2 Bose-Einstein Condensate in a Cavity

As compared to a thermal cloud of cold atoms, the system of a Bose-Einstein condensate (BEC) coupling with an optical cavity is of particular importance as it corresponds to some conceptually fundamental models of atoms coupling to a single mode light field. When the atoms are Bose condensed into a single motional quantum state, the number of degrees of freedom required to describe the system can be substantially reduced. Therefore, the experimental platform can be used to mimic some model Hamiltonians of matter-light interaction, including the Tavis-Cummings or the Dicke model, as well as the generic model for cavity opto-mechanics.

Under the mean-field approximation, which is valid in the presence of a cavity-mediated global coupling among all atoms, the condensate wave function and the cavity field are assumed by their amplitudes of expectation

$$\begin{aligned} \Psi(\mathbf{r},t) &\to \sqrt{N_c}\phi(\mathbf{r},t)\ , \\ a(t) &\to \alpha(t)\ , \end{aligned} \tag{79.89}$$

where N_c is the number of condensed atoms and $\phi(\mathbf{r})$ is the normalized wave function. These mean fields for atoms and cavity field satisfy the Gross-Pitaevskii-like equations

$$\begin{aligned} & i\hbar\partial_t\phi(\mathbf{r},t) \\ &= \Big\{ -\frac{\hbar^2\nabla^2}{2m} + V_{\rm trap}(\mathbf{r}) \\ &+ N_c g_{\rm atom}|\phi(\mathbf{r},t)|^2 + \hbar U_0|\alpha(t)|^2\cos^2(kz) \\ &+ \hbar\eta_{\rm eff}[\alpha(t)+\alpha^*(t)]\cos(kx)\cos(kz)\Big\}\phi(\mathbf{r},t)\ , \\ & i\partial_t\alpha(t) \\ &= \left[\omega_C - \omega_p + N_c U_0\langle\phi|\cos^2(kz)|\phi\rangle - i\kappa\right]\alpha(t) \\ &+ i\eta + N_c\eta_{\rm eff}\langle\phi|\cos(kx)\cos(kz)|\phi\rangle\ , \end{aligned} \tag{79.90}$$

where the interatomic contact interaction $g_{\rm atom} = 4\pi\hbar^2 a_s/m$ with a_s the s-wave scattering length. On one hand, the dynamics of the cavity field involves spatial averages over the condensate density distribution. On the other hand, the atoms are also affected by the backaction from the cavity field according to the potential-like terms which depend on the amplitude α and

intensity $|\alpha|^2$ of the cavity field in the Gross-Pitaevskii equation for atoms. The mean-field equations are usually solved numerically to obtain the time-evolution of the system and the steady state solutions for both atoms and cavity field [81].

As in a thermal atomic ensemble, the BEC trapped inside a cavity can also self-organize to emit intracavity field collectively. The key difference in the case of BEC is that the atomic motion is also quantized, and the transition is now between a uniform distribution and a periodic array of atoms in the cavity-induced lattice potential. As a consequence, the transition point is determined by the competition of kinetic energy and potential energy associated with the spatial modulation of atomic density.

Under the mean-field approximation, the steady state of the system can be determined by the numerical solutions of the Gross-Pitaevskii-like equations for both the cavity field α and the atomic mode $\phi(\mathbf{r})$. By assuming for simplicity that the atomic motion is only along the cavity axis and the cavity pumping $\eta = 0$, one can define an order parameter $\Theta = \langle\phi|\cos(kx)|\phi\rangle$, which describes the non-uniform spatial modulation of the atoms. As can be seen from a typical result of numerical solution shown in Fig. 79.12, the order parameter takes a nonzero value beyond a critical pumping strength η_{eff}, indicating self-organization of the density of atoms.

Self-organization of a BEC was experimentally achieved in 2010 [82]. In that experiment, a BEC of about 10^5 atoms was trapped inside a high-finesse FP cavity and was illuminated from a transversal direction by a far red-detuned standing-wave laser beam. By gradually increasing the power of the transverse laser beam beyond a critical value, a sharp rise of the intracavity field intensity and a macroscopic populations in the atomic momentum states $(px, pz) = (\pm\hbar k, \pm\hbar k)$ are observed, indicating a transition to the self-organization phase. Above this critical pump power, the relative phase $\Delta\phi$ between pump field and cavity field is observed to stay constant, which demonstrates that the system reached a steady state.

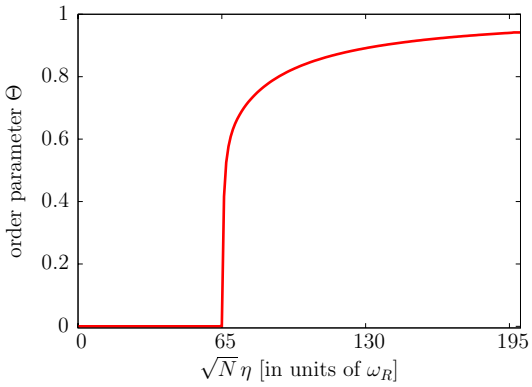

Figure 79.12: The steady-state order parameter Θ plotted as a function of the effective cavity pumping strength η_{eff}, indicating the self-organization of a Bose-Einstein condensate in an FP cavity [81]

Self-organization of a laser-driven BEC in an optical cavity can also be considered as an realization of the Dicke quantum phase transition in an open system, where the quantized atomic motion acts as a macroscopic spin which strongly couples to the cavity field. The Dicke model, or equivalently, the Tavis-Cummings model, is proposed to study the collective interaction between a set of two-level atoms and a single light mode

$$\begin{aligned}\mathcal{H}_{\text{Dicke}} =& \frac{1}{2}\hbar\omega_0 \sum_{j=1}^{N} \sigma_z^{(j)} + \hbar\omega_C a^\dagger a \\ &+ \hbar g \sum_{j=1}^{N} \left(\sigma_+^{(j)} a + a^\dagger \sigma_-^{(j)}\right) ,\end{aligned} \tag{79.91}$$

which contains a sum over all atoms with index j that couple to the field mode. It is instructive

to introduce the collective spin operators

$$S_z = \frac{1}{2}\sum_{j=1}^{N}\sigma_z^{(j)} \ , \qquad S_\pm = \sum_{j=1}^{N}\sigma_\pm^{(j)} \ , \tag{79.92}$$

together with the total spin operator $\mathbf{S} = (S_x, S_y, S_z)$, where N is the number of atoms, $S_\pm = S_x \pm iS_y$, and $\sigma^{(j)}$ are the Pauli spin operators for the j-th atoms. In this notation, the Dicke Hamiltonian becomes

$$\mathcal{H}_{\rm Dicke} = \hbar\omega_0 S_z + \hbar\omega_C a^\dagger a + \hbar g\left(S_+ a + a^\dagger S_-\right) \ . \tag{79.93}$$

Here we assumed that all atoms have the same frequency ω_0 and that they are coupled with the same strength g. Note that the eigenstates of the Dicke Hamiltonian are highly degenerate, reflecting the fact that there are many possible ways to accommodate a fixed number of excitations.

The eigenstates of the Dicke Hamiltonian, usually referred as Dicke states, can be labeled by the quantum numbers of the spin operators $\mathbf{S}^2|J,M\rangle = J(J+1)|J,M\rangle$ and $S_z|J,M\rangle = M|J,M\rangle$, where $J = 0, 1, \ldots, N/2$ and $M = -J, -J+1, \ldots, J$. In the weak excitation limit of $J + M \ll N$, the Dicke states behave like a harmonic oscillator, as can be seen from

$$\begin{aligned}\left|\langle J, M+1|S_+|J,M\rangle\right|^2 &= (J+M+1)(J-M) \\ &\approx (J+M+1)N \ .\end{aligned} \tag{79.94}$$

Thus, in this regime the Dicke model can be regarded as a pair of harmonic oscillators coupled at a rate of $\sqrt{N}g$. If there is only one excitation in the system, the eigenstate is equivalent to that of the JC model, except that the coupling strength is collectively enhanced by a factor of $\sqrt{N}$. However, for the case of more than one excitation, the energy spectrum acquires significant difference of anharmonicity.

For the case of large number of excitations, the Dicke Hamiltonian has been investigated extensively in the context of superradiance, during which process a macroscopic number of the atomic ensemble decay collectively and emit a large pulse of radiation. This can be seen from

$$S_+ S_-|J,M\rangle = (J+M)(J-M+1)|J,M\rangle \ , \tag{79.95}$$

which is proportional to the spontaneous emission rate of the ensemble. For the case of $M = J$, the emission rate is proportional to N as $J = N/2$. For the case of $M = 0$, however, it is proportional to N^2. This increase can be understood as a result of strong correlations between the atoms in the ensemble during the emission process.

The self-organization of a BEC-cavity system can be regarded as the Dicke model by considering a pair of motional states as two pseudo-spin states [82, 83]. The two motional states are given by the uniform condensate mode $|p_x, p_z\rangle = |0, 0\rangle$ and the coherent superposition of the four momentum states $|\pm\hbar k, \pm\hbar k\rangle$, where x and z denote the cavity and pump directions, respectively. Coherent light scattering between the transverse pump beam and the cavity mode couples these two momentum states via two distinguishable Raman channels, resulting in a tunable interaction between the cavity mode and the corresponding collective spin degree of freedom. Experimentally, the phase boundary was mapped out as a function of pump-cavity detuning $\omega_p - \omega_C$ as shown in Fig. 79.13 [82].

79.6.3 Cavity Opto-mechanics with Cold Atoms

The hybrid atom-cavity system can also be used to study an important model of cavity optomechanics, where a harmonically suspended mechanical element interacts with an intracavity single mode field. In certain limiting cases where the motional degrees of freedom of atoms can be reduced to a single-mode harmonic oscillator [72], the effective Hamiltonian of Eq.

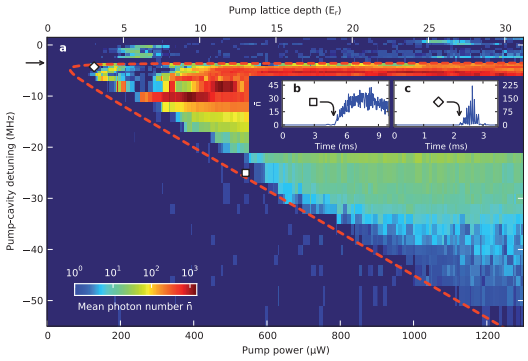

Figure 79.13: Dicke-model phase diagram. The mean-intracavity photon number is finite in the superradiant phase with large pumping power and small pump-cavity detuning [82]

(79.84) can be significantly simplified, leading to a generic form of cavity opto-mechanics Hamiltonian

$$\mathcal{H}_{\rm OM} = \hbar\omega_m c^\dagger c - \hbar\left[(\omega_p - \omega_C) - \frac{G}{2}(c^\dagger + c)\right] a^\dagger a + i\hbar\eta(a^\dagger - a)\,, \tag{79.96}$$

where $c^\dagger$ and c denote creation and annihilation operators of the mechanical oscillator at frequency ω_m, G is the dispersive shift of the cavity frequency induced by the atomic density modulation, and η is the pumping strength along the cavity axis.

The key ingredient of the experimental realization of the cavity opto-mechanics Hamiltonian Eq. (79.96) is that the cavity field must affect and sense predominantly a single collective motional mode of the atomic ensemble, which hence can be regarded as the harmonically suspended mechanical element. One possible way to realize this condition is to trap ultracold atoms in a far-detuned intracavity lattice potential such that the atoms form a stack of tightly confined atom clouds [84]. Each atom cloud is harmonically suspended with oscillation frequency ω_m and extends along the cavity axis by only a fraction of the optical wavelength. A cavity mode, whose periodicity differs from that of the trapping lattice potential, couples strongly to a single collective center-of-mass mode of the atomic stack. All remaining collective modes are detuned from the cavity field and hence contribute as a heat bath.

Another route to realize cavity opto-mechanics Hamiltonian is reported in 2008 [85]. In that experiment, a BEC is prepared in an external harmonic trapping potential, extending over several periods of the cavity standing-wave mode structure. Initially, all condensate atoms are prepared in the zero-momentum state $|p = 0\rangle$. The dispersive interaction with the cavity field diffracts atoms into the symmetric superposition of momentum states $|\pm 2\hbar k\rangle$ along the cavity axis. If the diffraction into higher-order momentum modes can be neglected, the dynamics of the coupled system can be well described by the opto-mechanics Hamiltonian Eq. (79.96).

79.7 Applications of Cavity QED

79.7.1 Quantum Non-demolition (QND) Counting of Photons

When the object of interest consists of only a few atoms and a few photons, the puzzling consequences of quantum mechanical measurement become visible. In the case of the micromaser, the information on the state of the field is imprinted in a subtle way on the atomic beam. While photon counting is normally a destructive operation, the dispersive part of the photon-atom interaction may be used to determine the photon number inside a resonator without altering it, on average. Dispersive effects shift the phase of an oscillating atomic dipole without changing its state.

The phase shift due to the field in the res-

onator can be measured in a Ramsey-type experiment [86]. Consider an atom with two transitions $|g\rangle \to |e\rangle$ and $|e\rangle \to |i\rangle$. The first is far from resonance with the cavity and the second is close to resonance, but with a detuning $\delta_{ie} = \omega - \omega_{ie}$ large enough so as not to change the cavity photon number as the atom passes through. The dynamic Stark effect of the $|g\rangle \to |e\rangle$ transition frequency due to state $|i\rangle$ is then

$$\Delta\omega_{eg} = \left[g_{ie}\sqrt{n+1}\right]^2/\delta_{ie} \ . \qquad (79.97)$$

If the resonator is now placed between the two Ramsey cavities, which are tuned to $\omega_{\rm R} \approx \omega_{eg}$, such that the polarization of the $|e\rangle \to |g\rangle$ transition is rotated by $\approx \pi/2$, then the additional phase shift $\Delta\omega_{eg}\tau$, where τ is the transit time through the optical resonator, can be measured, and hence the photon number n. Since Rydberg states have a large coupling constant g_μ, the phase shift due to a single atom is detectable [86].

This proposal was demonstrated experimentally in 2007 at ENS [87]. With the ability of developing super high-quality microwave cavity, the experimental group successfully performs a QND measurement on single photons via dispersive interaction of single atoms in circular Rydberg states. The atoms have a high principle quantum number $n = 50$ and the highest possible angular and magnetic quantum numbers $(l = n-1, |m_l| = n-1)$, hence acquire a life time of the order $\tau = 30$ms. The experiment can witness the birth, life, and death of a photon non-destructively.

A complete measurement of n requires a sequence of N atoms because a single Ramsey measurement only determines whether the atom is in state $|e\rangle$ or $|g\rangle$, and hence $\Delta\omega_{eg}\tau$ to within $\pm\pi/2$. Since each measurement provides one binary bit of information, a sequence of N measurements can in principle distinguish 2^N possible Fock states for the photon field. However, with a monoenergetic beam, integral multiples of 2π remain undetermined. A distribution of velocities, and hence transit times, is therefore desirable. An entropy reduction strategy for selecting an optimal velocity distribution, based on the outcome of previous measurements, is described in [88]. The experimental demonstration is also reported in 2007 by the same group at ENS [89], where the experimental setup was refined to distinguish states with photon number $n \leq 7$.

As a consequence of the uncertainty principle, a measurement of the photon number destroys all information about the phase of the field. In the present case, the noise in the conjugate variable (the phase) is prevented from coupling back on the measured one, and hence the measurement is called a quantum nondemolition experiment. Many other aspects of phase diffusion, entangled states, and quantum measurements in the micromaser are discussed in [90].

79.7.2 Detecting and Trapping Atoms through Strong Coupling

One of the key ingredients of cavity QED experiments is to deterministically localize atoms at desired positions in a cavity, where the atom-photon coupling can be well calculated and tuned. From Fig. 79.8 it is obvious that an atom travelling through the cavity will modify the transmission properties of this cavity. The ability of tuning strong coupling thus enables the experimenter to detect the presence of a single atom dispersively by monitoring cavity transmission or reflection. Laser cooled atoms have low velocities and spend sufficient time in the cavity even in free flight to generate the transmission signal shown in Fig. 79.14. The signals correspond to individual atom transits, and the shape depends on the detuning of the probe laser from the resonantly interacting cavity-atom system [55, 91]. Thus, the strongly coupled cavity QED system can work as a sensitive single atom detector, and can help us to extract the temperature and the statistical properties of the

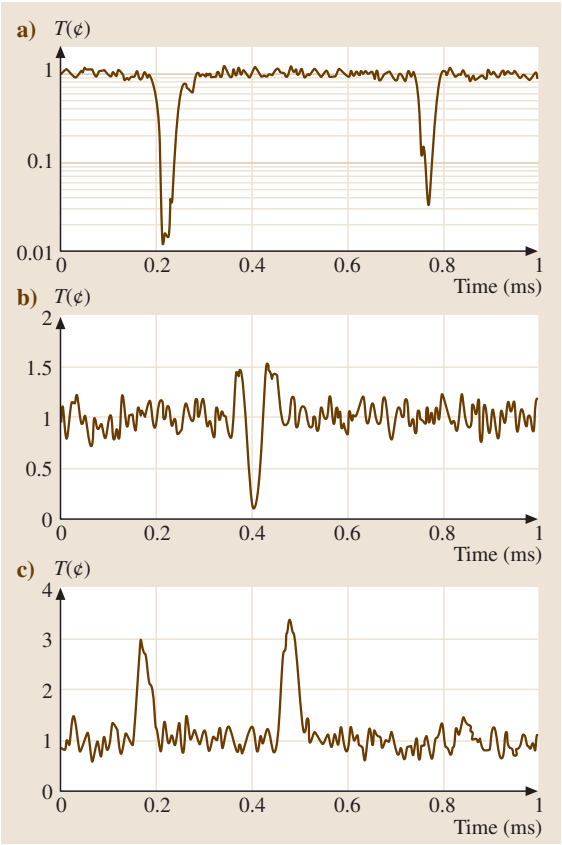

Figure 79.14: Transmission of a strongly coupled cavity for individual atom transits. Cesium atoms and cavity are in perfect resonance at $\lambda = 852\,\text{nm}$ while the probe laser is increasingly detuned to the red side of the resonance from top to bottom [109]

cold atoms, which have great potential in time-resolved atom-cavity microscopy and in tracking single atom trajectory.

The same scheme can also be applied to monitor a specific collective motion in an atomic ensemble [84, 92, 93]. In these experiments, the cavity mode is shifted in frequency by the strong interaction with the center-of-mass motion of the atomic ensemble. This provides the ability to realize continuous non-destructive measurement of a quantum many-body system.

The strong coupling between atom and cavity mode can also be used to trap atoms at specified positions. If an atom absorbs a photon inside the cavity, a strong dipole force can be exerted due to the inhomogeneous field distribution of the cavity mode. Trapping of atoms with a single photon was achieved [91], and from the time variation of the cavity transmission a reconstruction of atomic trajectories became possible. Similar mechanism is also implemented in a hybrid system of ion trap and optical cavity to localize single ions [94, 95]. This has allowed for very long trapping times of more than 90 min, as well as excellent control over the position of trapped ions within a sub-wavelength precision [96]. Recently, position control was also demonstrated individually for two ions trapped in the same cavity [97].

79.7.3 Single Photon Sources

Coherent laser fields are considered the ultimate source of classical radiation fields, and they are characterized by the random arrival time of photons. Nonclassical light sources with, for instance, a regularized stream of photons offer interesting properties for low-noise measurement applications.

Cavity-QED systems offer an attractive light-matter process for the generation of such *photon-bit-streams*, or single photon sources [98]. In such devices, a single photon state can, for instance, be created by Raman processes involving a classical field, which serves as the control parameter for the process, and the vacuum field of the optical resonator. The Raman process leaves a single photon in the cavity, which only weakly interacts with the atom. If the resonator has suitable transmission properties, this photon will then escape with predetermined frequency, shape, and propagation direction. Deterministic single photon sources have been realized with quantum dots [99, 100], single molecules [101], and also with slow [102, 103] or trapped [104, 105] cold atoms and ions [96, 106] inside

optical cavities.

The high efficiency of photon sources also paves the route towards quantum memory and quantum network, which is essential for providing cluster states in one-way quantum computing [92] and for the quantum simulation of complex solid-state systems [93]. Successive operations of photon generation, photon storage, and photon retrieval were successfully demonstrated in a hybrid atom-cavity system [70].

79.7.4 Generation of Entanglement

In the middle of the 1990s, it was realized that fully controlled quantum systems could be used to implement a revolutionary type of information processing now called quantum computing [107]. From the beginning, cavity QED has conceptually played an important role for experimental realizations, since it offers a route to manipulate, in principle, all physical parameters of a coherently interacting system. With the well established microwave-cavity–Rydberg-atom system, it was proven that the generation of correlated and nonlocal, so-called *entangled* quantum states, is possible [108].

The first *application* of cavity QED was the transfer of the strong coupling idea to the combined internal and motional quantum states of trapped ions [110]. Here the harmonic oscillation of the ion replaces the electric field of the conventional cavity-QED system. This quantum gate was realized with a system of two trapped ions coupled to each other by Coulomb forces [111].

Ideas about how to use the strong coupling of atoms and photons [112, 113, 114] for the generation of atom–photon, photon–photon, or atom–atom (by insertion of more than one atom) abound, and become possible with the aid of experimental capabilities in the preparation and control of atoms in high-finesse cavities.

Atom–photon entanglement A key advantage of the hybrid atom-cavity QED system is the potential to work as a quantum interface through which quantum state can be faithfully transferred from one medium to another. By driving a vacuum-stimulated Raman adiabatic passage into a superposition of two atomic ground states, for example with different orientations of the atomic spin of ^{87}Rb atoms [69], the internal state of a single atom can be entangled with the polarization state of a single photon.

Photon–photon entanglement Starting from the atom-photon entangled state, one can drive another vacuum simulated Raman adiabatic passage into a single atomic ground state with a well-defined spin orientation to map the quantum state of the atom into a second single photon. This process disentangle the atom and the light, and create an entangled photon pair. The two photons are emitted one after the other into the same spatial mode, hence have never overlapped with each other [115].

Atom–atom entanglement By reversing the role of field and atom, the atom–photon entanglement can also be transferred to a second atom to create atom–atom entanglement. Multiparticle entanglement is considered as crucial resource of quantum simulation, quantum computation, and quantum-enhanced metrology. The largest number of atoms ever to be entangled in an FP cavity is about 3000 [116], and is more than 40 in an optical fiber cavity [117]. The entanglement between two ions and two atomic ensembles via coupling to cavity mode were also demonstrated in experiments [118, 119].

Quantum network Using the aforementioned atom–photon entangled state as building blocks, an elementary quantum network can be implemented with two fiber-linked optical cavities, each containing a single trapped atom as a stationary quantum node. This scheme offers a clear perspective of both addressability

and scalability, because the atoms are trapped in their corresponding cavities, and more constituent cavities can be added to an existing network without much apparent complications. Besides, the component cavities can in principle be arranged in any geometry and that two-party links can be established at will, both in time and space.

Elementary quantum network links implementing teleportation protocols between remote trapped atoms and atom-photon quantum gate operations have been demonstrated in experiments [115, 120, 121, 122]. Besides, quantum networking between two cavities has also been experimentally demonstrated with atomic ensembles [123, 124]. These achievements represent a big step towards the goal to realize an elementary quantum network and a feasible quantum computing system.

Bibliography

[1] Cavity QED is reviewed in detail in S. Haroche: *Fundamental Systems in Quantum Optics*, ed. by J. Dalibard et al. (Elsevier, Amsterdam 1992)

[2] D. Meschede: Phys. Rep. **211**(5), 201–250 (1992)

[3] P. Berman (Ed.): *Cavity Quantum Electrodynamics* (Academic, Amsterdam 1994)

[4] An introduction into the more general framework of low energy Quantum Electrodynamics may be found in the recent textbook P. Milonni (Ed.): *The Quantum Vacuum* (Academic, Boston 1994)

[5] P. Berman (Ed.): *Cavity Quantum Electrodynmics* (Academic, Boston 1994)

[6] V. Weisskopf, E. Wigner: Z. Phys. **63**, 54 (1930)

[7] F. Levin, D. Micha (Eds.): *Long-Range Casimir Forces* (Plenum, New York 1993)

[8] D. Meschede, H. Walther, G. Müller: Phys. Rev. Lett. **54**, 551 (1985)

[9] L. Allen, J. Eberly: *Optical Resonance and Two-Level-Atoms* (Dover, New York 1987), reprint of the original 1975 edn.

[10] E. A. Power, T/ Thirunamachandran: Am. J. Phys. **46** 370 (1978)

[11] D. Kleppner: Phys. Rev. Lett. **47**, 233 (1981)

[12] R. G. Hulet, E. Hilfer, D. Kleppner: Phys. Rev. Lett. **55**, 2137 (1985)

[13] W. Jhe, A. Anderson, E. Hinds, D. Meschede, L. Moi, S. Haroche: Phys. Rev. Lett. **58**, 666 (1987)

[14] J. Eschner, Ch. Raab, F. Schmidt-Kaler, R. Blatt: Nature **413**, 495 (2001)

[15] M. A. Wilson, P. Bushev, J. Eschner, F. Schmidt-Kaler, C. Becher, R. Blatt, U. Dorner: Phys. Rev. Lett. **91**, 213602 (2003)

[16] J. Dowling: *Quantum Measurements in Optics*, ed. by P. Tombesi, D. Walls (Plenum, New York 1992)

[17] K. H. Drexhage: *Progress in Optics*, Vol. 12, ed. by E. Wolf (North-Holland, Amsterdam 1974)

[18] V. Sandoghar, C. Sukenik, E. Hinds, S. Haroche: Phys. Rev. Lett. **68**, 3432 (1992)

[19] H. Casimir, D. Polder: Phys. Rev. **73**, 360 (1948)

[20] C. Sukenik, M. Boshier, D. Cho, V. Sandoghar, E. Hinds: Phys. Rev. Lett. **70**, 560 (1993)

[21] A. Shih, D. Raskin, P. Kusch: Phys. Rev. A **9**, 652 (1974)

[22] C. Cohen-Tannoudji: *Fundamental Systems in Quantum Optics*, ed. by J. Dalibard et al. (Elsevier, Amsterdam 1992)

[23] S. Haroche, M. Brune, J. M. Raimond: Europhys. Lett. **14**, 19 (1991)

[24] M. Chevrollier, M. Fichet, M. Oria, G. Rahmat, D. Bloch, M. Ducloy: J. Phys. (Paris) **2**, 631 (1992)

[25] P. Bushev, A. Wilson, J. Eschner, C. Raab, F. Schmidt-Kaler, C. Becher, R. Blatt: Phys. Rev. Lett. **92**, 223602 (2004)

[26] M. Brune, P. Nussenzveig, F. Schmidt-Kaler, R. Bernadot, A. Maali, J. M. Raimond, S. Haroche: Phys. Rev. Lett. **72**, 3339 (1994)

[27] H. Failache, S. Saltiel, A. Fischer, D. Bloch, M. Ducloy: Phys. Rev. Lett. **88**, 243603 (2002)

[28] W. von Klitzing, R. Long, V. S. Ilchenko, J. Hare, V. Lefèvre-Seguin: Opt. Lett. **26**, 166 (2001)

[29] E. Yablonovitch: Phys. Rev. Lett. **58**, 2059 (1987)

[30] K. Inoue, K. Ohtaka (Eds.): *Photonic Crystals* (Springer, Berlin, Heidelberg 2004)

[31] J. P. Reithmaier, G. Sek, A. Löffler, C. Hofmann, S. Kuhn, S. Reitzenstein, L. V. Keldysh, V. D. Kulakovskii, T. L. Reinecke, A. Forchel: Nature **432**, 197 (2004)

[32] T. Yoshie, A. Scherer, J. Hendrickson, G. Khitrova, H. M. Gibbs, G. Rupper, C. Ell, O. B. Shchekin, D. G. Deppe: Nature **432**, 200 (2004)

[33] K. Vahala: Nature **424**, 839 (2003)

[34] C. Cohen-Tannoudji: *Frontiers in Laser Spectroscopy*, ed. by R. Balian et al. (North-Holland, Amsterdam 1977)

[35] R. Thompson, G. Rempe, H. Kimble: Phys. Rev. Lett. **68**, 1132 (1992)

[36] J. McKeever, A. Boca, A. D. Boozer, J. R. Buck, H. J. Kimble: Nature **425**, 268 (2003)

[37] I. Chiorescu, P. Bertet, K. Semba, Y. Nakamura, C. J. P. M. Harmans, J. E. Mooij: Nature **431**, 159 (2004)

[38] A. Wallraff, D. I. Schuster, A. Blais, L. Frunzio, R.-S. Huang, J. Majer, S. Kumar, S. M. Girvin, R. J. Schoelkopf: Nature **431**, 164 (2004)

[39] R. F. Stebbings, F. B. Dunning (Eds.): *Rydberg States of Atoms and Molecules* (Cambridge Univ. Press, Cambridge 1983)

[40] E. T. Jaynes, F. W. Cummings: Proc. IEEE **51**, 89 (1963)

[41] H. Paul: Ann. Phys. **11**, 411 (1963)

[42] J. H. Eberly, N. B. Narozhny, J. J. Sanchez-Mondragon: Phys. Rev. Lett. **44**, 1323 (1980)

[43] N. B. Narozhny, J. J. Sanchez-Mondragon, J. H. Eberly: Phys. Rev. A **23**, 236 (1981)

[44] P. L. Knight, P. M. Radmore: Phys. Rev. A **26**, 676 (1982)

[45] C. K. Law, J. H. Eberly: Phys. Rev. Lett. **76**, 1055 (1996)

[46] H. J. Briegel, B. G. Englert: Phys. Rev. A **47**, 3311 (1993)

[47] C. Ginzel, H. J. Briegel, U. Martini, B. G. Englert, A. Schenzle: Phys. Rev. A **48**, 732 (1993)

[48] B. R. Mollow: Phys. Rev. **188**, 1969 (1969)

[49] P. Filipowicz, J. Javanainen, P. Meystre: Phys. Rev. A **34**, 3077 (1986)

[50] G. Rempe, H. Walther: Phys. Rev. A **42**, 1650 (1990)

[51] G. Rempe, F. Schmidt-Kaler, H. Walther: Phys. Rev. Lett. **64**, 2783 (1990)

[52] U. Benson, G. Raithel, H. Walther: Phys. Rev. Lett. **72**, 3506 (1994)

[53] P. Meystre, G. Rempe, H. Walther: Opt. Lett. **13**, 1078 (1988)

[54] C. Wagner, A. Schenzle, H. Walther: Opt. Commun. **107**, 318 (1994)

[55] H. Mabuchi, Q. A. Turchette, M. S. Chapman, H. J. Kimble: Opt. Lett. **21**, 1393 (1996)

[56] C. J. Hood, M.S. Chapman, T. W. Lynn, H.J. Kimble: Phys. Rev. Lett. **80**, 4153 (1998)

[57] P. Münstermann, T. Fischer, P. Maunz, P. W. H. Pinkse, G. Rempe: Phys. Rev. Lett. **82**, 3791 (1999)

[58] P. Horak, G. Hechenblaikner, K. M. Gheri, H. Stecher, H. Ritsch: Phys. Rev. Lett. **79**, 4974 (1997)

[59] K. Murr: Phys. Rev. Lett. **96**, 253001 (2006)

[60] P. Maunz, T. Puppe, I. Schuster, N. Syassen, P. W. H. Pinkse, G. Rempe: Nature **428**, 50 (2004)

[61] A. Boca, R. Miller, K. M. Birnbaum, A. D. Boozer, J. McKeever, H. J.. Kimble: Phys. Rev. Lett. **93**, 233603 (2004)

[62] P. Maunz, T. Puppe, I. Schuster, N. Syassen, P. W. H. Pinkse, G. Rempe: Phys. Rev. Lett. **94**, 033002 (2005)

[63] A. Kubanek, A. Ourjoumtsev, I. Schuster, M. Koch, P. W. H. Pinkse, K. Murr, G. Rempe: Phys. Rev. Lett. **101**, 203602 (2008)

[64] I. Schuster, A. Kubanek, A. Fuhrmanek, T. Puppe, P. W. H. Pinkse, K. Murr, G. Rempe: Nat. Phys. **4**, 382 (2008)

[65] A. Ourjoumtsev, A. Kubanek, M. Koch, C. Sames, P. W. H. Pinkse, G. Rempe, K. Murr: Nature **474**, 623 (2011)

[66] A. Kuhn, M. Hennrich, G. Rempe: Phys. Rev. Lett. **89**, 067901 (2002)

[67] J. McKeever, A. Boca, A. D. Boozer, R. Miller, J. R. Buck, A. Kuzmich, H. J. Kimble: Science **303**, 1992 (2004)

[68] A. D. Boozer, A. Boca, R. Miller, T. E. Northup, H. J. Kimble: Phys. Rev. Lett. **98**, 193601 (2007)

[69] T. Wilk, S. C. Webster, A. kuhn, G. Rempe: Science **317**, 488 (2007)

[70] H. P. Specht, C. Nölleke, A. Reiserer, M. Uphoff, E. Figueroa, S. Ritter, G. Rempe: Nature **473**, 190 (2011)

[71] T. Kampschulte, W. Alt, S. Brakhane, M. Eckstein, R. Reimann, A. Widera, D. Meschede: Phys. Rev. Lett. **105**, 153603 (2010)

[72] T. J. Kippenberg, K. J. Vahala: Science **321**, 1172 (2008)

[73] T. Fischer, P. Maunz, T. Puppe, P. W. H. Pinkse, G. Rempe: New J. Phys. **3**, 11 (2001)

[74] P. Münstermann, T. Fischer, P. Maunz, P. W. H. Pinkse, G. Rempe: Phys. Rev. Lett. **84**, 4068 (2000)

[75] R. H. Dicke: Phys. Rev. **93**, 99 (1954)

[76] R. G. DeVoe, R. G. Brewer: Phys. Rev. Lett. **76**, 2049 (1996)

[77] P. Domokos, H. Ritsch: Phys. Rev. Lett. **89**, 253003 (2002)

[78] J. K. Asbóth, P. Domokos, H. Ritsch, A. Vukics: Phys. Rev. A **72**, 053417 (2005)

[79] A. T. Black, H. W. Chan, V. Vuletić: Phys. Rev. Lett. **91**, 203001 (2003)

[80] D. Nagy, J. K. Asbóth, P. Domokos, H. Ritsch: Europhys. Lett. **74**, 254 (2006)

[81] D. Nagy, G. Szirmai, P. Domokos: Eur. Phys. J. D **48**, 127 (2008)

[82] K. Baumann, C. Guerlin, F. Brennecke, T. Esslinger: Nature **464**, 1301 (2010)

[83] D. Nagy, G. Kónya, G. Szirmai, P. Domokos: Phys. Rev. Lett. **104**, 130401 (2010)

[84] S. Gupta, K. L. Moore, K. W. Murch, D. M. Stamper-Kurn: Phys. Rev. Lett. **99**, 213601 (2007)

[85] F. Brennecke, S. Ritter, T. Donner, T. Esslinger: Science **322**, 235 (2008)

[86] M. Brune, S. Haroche, V. Lefevre, J. M. Raimond, N. Zagury: Phys. Rev. Lett. **65**, 976 (1990)

[87] S. Gleyzes, S. Kuhr, C. Guerlin, J. Bernu, S. Deléglise, U. B. Hoff, M. Brune, J.-M. Raimond, S. Haroche: Nature **446**, 297 (2007)

[88] R. Schack, A. Breitenbach, A. Schenzle: Phys. Rev. A **45**, 3260 (1992)

[89] C. Guerlin, J. Bernu, S. Deléglise, C. Sayrin, S. Gleyzes, S. Kuhr, M. Brune, J.-M. Raimond, S. Haroche: Nature **448**, 889 (2007)

[90] C. Wagner, A. Schenzle, H. Walther: Phys. Rev. A **47**, 5068 (1993)

[91] A. C. Doherty, T. W. Lynn, C. J. Hood, H. J. Kimble: Phys. Rev. A **63**, 013401 (2001) and references therein

[92] F. Brennecke, T. Donner, S. Ritter, T. Bourdel, M. Köhl: Nature **450**, 268 (2007)

[93] Y. Colombe, T. Steinmetz, G. Dubois, F. Linke, D. Hunger, J. Reichel: Nature **450**, 272 (2007)

[94] G. R. Guthöhrlein, M. Keller, K. Hayasaka, W. Lange, H. Walther: Nature **414**, 49 (2001)

[95] A. B. Mundt, A. Kreuter, C. Becher, D. Leibfried, J. Eschner, F. Schmidt-Kaler, R. Blatt: Phys. Rev. Lett. **89**, 103001 (2002)

[96] M. Keller, B. Lange, K. Hayasaka, W. Lange, H. Walther: Nature **431**, 1075 (2004)

[97] M. Steiner, H. M. Meyer, C. Deutsch, J. Reichel, M. Möhl: Phys. Rev. Lett. **110**, 043003 (2013)

[98] C. K. Law, H. J. Kimble: J. Mod. Opt. **44**, 2067 (1997)

[99] P. Michler, A. Kiraz, C. Becher, W. V. Schoenfeld, P. M. Petroff, E. Hu. Lidong Zhang, A. Imamoglu: Science **290**, 2282 (2000)

[100] C. Santori, M. Pelton, G. Solomon, Y. Dale, Y. Yamamoto: Phys. Rev. Lett. **86**, 1502 (2001)

[101] B. Lounis, W. E. Moerner: Nature **407**, 491 (2000)

[102] A. Kuhn, M. Hennrich, G. Rempe: Phys. Rev. Lett. **89**, 067901 (2002)

[103] T. Wilk, S. C. Webster, H. P. Specht, G. Rempe, A. Kuhn: Phys. Rev. Lett. **98**, 063601 (2007)

[104] J. McKeever, A. Boca, A. D. Boozer, R. Miller, J. R. Buck, A. Kuzmich, H. J. Kimble: Science **303**, 1992 (2004)

[105] M. Hijlkema, B. Weber, H. P. Specht, S. C. Webster, A. Kuhn, G. Rempe: Nat. Phys. **3**, 253 (2007)

[106] H. G. Barros, A. Stute, T. E. Northup, C. Russo, P. O. Schmidt, R. Blatt: New J. Phys. **11**, 103004 (2009)

[107] D. P. DiVincenzo: Fortschr. Phys. **48**, 771–783 (2000)

[108] J. M. Raimond, M. Brune, S. Haroche: Rev. Mod. Phys. **73**, 565 (2001)

[109] C. J. Hood, M. S. Chapman, T. W. Lynn, H. J. Kimble: Phys. Rev. Lett. **80**, 4157 (1998)

[110] J. I. Cirac, P. Zoller: Phys. Rev. Lett. **74**, 4091 (1995)

[111] F. Schmidt-Kaler, H. Häffner, M. Riebe, S. Gulde, G. P. T. Lancaster, T. Deuschle, C. Becher, C. F. Roos, J. Eschner, R. Blatt: Nature **422**, 408 (2003)

[112] T. Pellizari, S. A. Gardiner, J. I. Cirac, P. Zoller: Phys. Rev. Lett. **75**, 3788 (1995)

[113] A. S. Soerensen, K. Moelmer: Phys. Rev. Lett. **91**, 097905 (2003)

[114] L. You, X. X. Yi, X. H. Su: Phys. Rev. A **67**, 032308 (2003)

[115] B. Weber, H. P. Specht, T. Müller, J. Bochmann, M. Mücke, D. L. Moehring, G. Rempe: Phys. Rev. Lett. **102**, 030501 (2009)

[116] R. McConnell, H. Zhang, J. Hu, S. Ćuk, V. Vuletić: Nature **519**, 439 (2015)

[117] F. Haas, J. Volz, R. Gehr, J. Reichel, J. Estéve: Science **344**, 180 (2014)

[118] B. Casabone, A. Stute, K. Friebe, B. Brandstätter, K. Schüppert, R. Blatt, T. E. Northup: Phys. Rev. Lett. **111**, 100505 (2013)

[119] J. Simon, H. Tanji, S. Ghosh, V. Vuletić: Nat. Phys. **3**, 765 (2007)

[120] S. Ritter, C. Nölleke, C. Hahn, A. Reiserer, A. Neuzner, M. Uphoff, M. Mücke, E. Figueroa, J. Bochmann, G. Rempe: Nature **484**, 195 (2012)

[121] C. Nölleke, A. Neuzner, A. Reiserer, C. Hahn, G. Rempe, S. Ritter: Phys. Rev. Lett. **110**, 140403 (2013)

[122] A. Reiserer, N. Kalb, G. Rempe, S. Ritter: Nature **508**, 237 (2014)

[123] K. S. Choi, H. Deng, J. Laurat, H. J. Kimble: Nature **452**, 67 (2008)

[124] D. N. Matsukevich, T. Chaneliére, S. D. Jenkins, S. -Y. Lan, T. A. B. Kennedy, A. Kuzmich: Phys. Rev. Lett. **96**, 030405 (2006)

光腔中的超冷原子气体

余东洋 [1]，姬 青 [1]，张 翔 [1,2,*]，张 威 [1,2†]

[1] 中国人民大学物理系，北京市海淀区中关村大街 59 号，100872
[2] 光电功能材料北京市重点实验室，北京市海淀区中关村大街 59 号，100872

摘要：近年来，光腔和冷原子气体的耦合系统受到了越来越多的关注。本文简要综述了近年来该领域在理论和实验方面的一些进展，重点关注其中的超辐射相变，并围绕光腔–原子耦合这一特征，分别介绍了超冷玻色气体和费米气体中的新奇量子相和量子相变。这些研究工作展示了该系统在非平衡态物理、多体系统的量子模拟、人造规范势和人造自旋–轨道耦合等方向的价值和意义。

关键词: 腔量子电动力学；超冷原子气体；超辐射跃迁；非平衡态

中图分类号： O469 **文献标识码：** A **DOI:** 10.13725/j.cnki.pip.2017.04.001

目 录

I. 导论

近几十年来，原子分子物理和光学领域发展了一系列用于冷却、束缚、操控和测量原子、分子和光子的技术。特别是随着磁束缚、光束缚、激光冷却、蒸发冷却、Feshbach 共振、光晶格和高品质的光学共振腔等技术的日益成熟，使得人们可以在纳米和纳开量级控制原子外部自由度的同时，也能对原子内部状态进行精确地制备和操控。这些实验手段为人们研究物质在极低温下的量子效应、新奇物相以及光与物质的相互作用提供了一个极佳的平台。

该领域的一个重要方向是研究光学微腔和冷原子气体的耦合系统。从理论方面，耦合系统中的光学模式和原子自由度相互耦合会带来很多新奇的物理现象。首先，原子可以通过散射驱动光子进入腔光场，在光腔中实现超辐射相变，同时伴随着原子系统发生对称性破缺。在相变前后，原子系统的基态和激发态特征，以及动力学行为都会受到光场反馈的影响。特别值得注意的是，由于腔内光子会漏出腔外，导致腔光场存在耗散并和环境发生耦合，该体系长时间后将达到动力学稳态，而非热力学平衡态。这一特征不仅为研究非平衡态物理提供了优秀的平台，而且漏出腔外的光子还能提供非破坏性的测量手段。其次，在发生超辐射相变之后，腔内光子和原子发生相干耦合，可以在原子间诱导出等效的长程相互作用。这不仅将有助于在碱金属超冷原子气体中实现和研究电荷密度波 (Charge Density Wave，CDW) 和超固 (supersolid) 等新奇多体物相，还可能使体系出现燕尾结构等非线性效应。另外，还可以利用腔光场在多分量原子气体中实现人造规范势和人造自旋–轨道耦合，为研究强磁场物理、非

Received date: 2017-05-02
E-mail: *siang.zhang@ruc.edu.cn; † wzhangl@ruc.edu.cn

平庸拓扑物态等问题提供新的可能。从应用角度，光腔–原子耦合体系兼顾了光学系统中丰富的测量操控手段和原子系统扩展方便、耦合强度大、退相干时间长等优势，有可能用来实现量子存储、量子中继等重要技术应用。

本文将简要综述近年来在光腔–原子耦合系统的研究中取得的一些进展。重点聚焦超冷玻色和费米气体中的超辐射相变，以及与之相关的原子气体中的新奇量子现象。

II. 背景：腔量子电动力学

当利用波导管等电介质把光波局限在有限空间中时，光的模式会受到边界条件的限制。由此引起的有限空间中真空场的变化会导致原子的自发辐射几率幅或被加强或被减弱。基于此，人们设计了许多用途广泛的光腔，可以用于测量光波波长、测量光谱以及激光系统等等。根据被束缚光场的特点，光腔可以分为驻波腔（如 Fabry-Perót 腔，简称 FP 腔）和行波腔（如环形腔）等。

常用的驻波腔是 FP 腔，它由两面距离 $l_{\rm res}$ 很近（约 200 μm）且反射率 $\mathcal{R}$ 极高的镜子构成。实验操作中常用两块近平面的球面玻璃代替平面的镜子。反映光腔性质的一个重要参数是品质因数 $\mathcal{F}$

$$\mathcal{F}=\frac{\Delta\nu_{\rm FSR}}{\Delta\nu_{\rm C}}, \tag{1}$$

其中 $\Delta\nu_{\rm FSR}$ 是不同本征模式之间的频率差，$\Delta\nu_{\rm C}$ 是通频带的半高宽，主要受镜子间距 $l_{\rm res}$ 和品质影响。以 ETH 的 Esslinger 实验小组的光腔为例 [1]，光腔间距 $l_{\rm res}\approx 176$ μm，球面玻璃的半径 $R\approx 75$ mm。由于边界条件要求波长 λ 满足 $n\lambda/2=l_{\rm res}$，这使得沿腔轴方向模式之间的频率差 $\Delta\nu_{\rm FSR}=c/2l_{\rm res}=852$ GHz。对于波长 $\lambda=785.3$ nm 的光波，$\Delta\nu_{\rm C}=2.4$ MHz。因此该光腔的品质因数可达 $\mathcal{F}=3.42\times10^5$。品质因数还决定了光腔的耗散能力。光子在腔中来回反射 $\langle N\rangle=\mathcal{F}/2\pi$ 次后，会通过镜子漏出光腔，其耗散率为 $\kappa=2\pi\Delta\nu_{\rm C}$。此外，腔中还存在垂直于腔轴方向（横向）的模式 TEM_{nm}，其中 n，m 为横向腔模的量子数。在上述实例中，能量最低的横向模式标记为 TEM_{00}，与高能模式的间距 $\Delta\nu_{\rm T}=18.6$ GHz。

将原子置于这样的光腔内，当原子的基态与激发态之间的跃迁频率 $\omega_{\rm A}=\omega_{\rm e}-\omega_{\rm g}$（比如 ^{87}Rb 的 D_2 谱系）接近于腔共振的频率 $\omega_{\rm C}=2\pi\nu_{\rm C}$ 时，由于原子的尺寸远远小于光波波长，此时原子通过电偶极相互作用与腔模耦合，其强度 $\hbar g_0=d\cdot E_{\rm C}=d\sqrt{\hbar\omega_{\rm C}/\varepsilon_0 V_{\rm cav}}$。这里 d 表示原子的电偶极矩，ε_0 为真空的介电常数，$\mathrm{V}_{\rm cav}$ 表示腔的有效体积。在上述实验中，g_0 达到了 $2\pi\times10.6$ MHz。

III. 超辐射及 DICKE 模型

根据爱因斯坦的自发辐射理论，真空电磁场与单个原子的相互作用会导致处于激发态的原子通过自发辐射回到原子的基态。在这个过程中，自发辐射几率幅主要依赖于原子的能级结构。1954 年，Dicke 将这一过程推广到多原子体系，从理论上研究了 N 个全同原子和单模光场之间的相互作用 [2]。在两能级近似下，Dicke 发现所有原子趋向于协同向同一个方向辐射，且自发辐射几率幅被提高了 N 倍，即 $\Gamma_N\propto N\Gamma_0$，其中 Γ_0 是单个原子的自然自发辐射几率。这种相干效应后来被称为超辐射 (superradiance)。

随着冷原子技术的发展和成熟，人们得以利用高度可调且纯净的冷原子体系研究超辐射现象 [3−14]。经过十几年的研究，人们已经对超辐射现象有了较为深入的认识和理解。1999 年，Inouye 等人研究了 “雪茄型” 玻色–爱因斯坦凝聚体 (BEC) 的瑞利散射 [3]。他们用红失谐的线偏振光横向驱动 BEC，并且使得其线偏振方向垂直于 BEC 长轴。实验发现，由于 BEC 在空间的不对称性，散射光会沿着 BEC 长轴方向散射，这种现象在文献中被称为物质波超辐射 (matter wave superradiance)。在这一现象中，被原子自发散射的光子沿着介质 (BEC) 长轴被原子受激瑞利散射，同时原子获得光子的反冲动量，运动的原子与静止的原子相位相干形成物质波。同时，物质波作为光栅散射驱动光，形成物质波超辐射。实验还发现静止的原子数会随着时间以比指数更快的形式衰减，从另一个侧面反映了超辐射的性质。由于 BEC 的相位相干性，物质波超辐射现象在 BEC 中具有失谐非对称性（相对于原子的激发态），即红失谐加强超辐射而蓝失谐抑制超辐射 [8−9]。物质波超辐射现象同样适用于不同统计性质的介质，比如费米子或者热原子，但超辐射现象保持失谐对称性 [11]。这里尤其值得注意的是，超辐射现象不一定需要量子简并。2005 年，来自日本的研究者 Yoshikawa 等人在实验上借助拉曼散射成功地在热原子中观察到了拉曼物质波超辐射现象 [6]。他们在实验中通过拉曼散射避开了物质波相干散射的影响，并

发现热原子气体中的相干时间主要受温度影响。

由于精细和超精细劈裂以及电子之间的相互作用，一般的原子能级结构较为复杂。但是，当原子最外层只有一个电子时，内部满壳层电子被紧紧束缚在内层，而对外层电子的影响可以忽略。因此，碱金属原子通常具有相对简单的光谱结构，从而在理论和实验上得到了广泛深入的研究。在冷原子物理中，人们常用的是碱金属的 D_2 谱系，其波长在可见光范围。由于能量守恒，单色性极好的激光（频率 $\omega_{\rm C}$）只能有效耦合其频率附近的能级。为了物理清楚，我们可以假设原子只有一个激发态能级（与基态频率差 $\omega_{\rm A}$）能在单模光场的作用下被显著激发，这一近似称为两能级近似。此外，由于可见光的波长 λ（约 500 nm）远大于原子尺寸（约 0.1 nm），在原子尺度内激光强度近似为常数，因此可以忽略在原子尺度上光场强度的变化，这一近似称为偶极近似。在两能级近似和偶极近似下，描述单原子和单模光场相互作用的哈密顿量（本文取自然单位 $\hbar \equiv 1$）可以写为如下形式，

$$\hat{H} = \omega_{\rm C}\hat{a}^{\dagger}\hat{a} + \frac{\omega_{\rm A}}{2}\hat{\sigma}_z + g_0\Big(\hat{a}^{\dagger} + \hat{a}\Big)\Big(\hat{\sigma}_+ + \hat{\sigma}_-\Big). \quad (2)$$

其中 $\hat{a}^{\dagger}$ 和 $\hat{a}$ 是光子的产生湮灭算符，$\hat{\sigma}_+ = |e\rangle\langle g|$ 和 $\hat{\sigma}_- = |g\rangle\langle e|$ 是原子的升降算符，$\sigma_z = |e\rangle\langle e| - |g\rangle\langle g|$，$g_0$ 代表单光子拉比频率。除了利用真实原子以外，利用人工原子也能实现上述模型 [15−16]。如果耦合强度 g_0 远小于光子频率 $\omega_{\rm C}$，我们称为弱耦合极限。目前为止，在直接利用可见光耦合原子的方案中，使用原子芯片方案 [17] 达到了最大的耦合强度（约为 200 MHz），但是其值仍然远小于可见光频率（$\sim 10^8$ MHz）。在这种条件下，哈密顿量 (2) 式中的能量不守恒项 $\hat{a}\hat{\sigma}_-$ 和 $\hat{a}^{\dagger}\hat{\sigma}_+$ 将变得不再重要，可以被舍去。在量子光学中，这个近似被称为旋波近似 (Rotating Wave Approximation，RWA)，并由此可以得到常见的单原子 Jaynes-Cummings (JC) 模型

$$\hat{H} = \omega_{\rm C}\hat{a}^{\dagger}\hat{a} + \frac{\omega_{\rm A}}{2}\hat{\sigma}_z + g_0\big(\hat{a}^{\dagger}\hat{\sigma}_- + \hat{a}\hat{\sigma}_+\big). \quad (3)$$

相反地，如果耦合强度 g_0 达到了光子频率 $\omega_{\rm C}$ 的量级，我们称为强耦合。此时，旋波近似不再适用，能量不守恒项和能量守恒项将同等重要，并会导致一些有趣的现象 [15−16]。

在弱耦合条件下，当有 N 个全同原子与单模光场相互作用时，其有效哈密顿量写作

$$\hat{H} = \omega_{\rm C}\hat{a}^{\dagger}\hat{a} + \frac{\omega_{\rm A}}{2}\sum_{j=1}^{N}\hat{\sigma}_{z,j} + \frac{\tilde{g}_0}{\sqrt{N}}\sum_{j=1}^{N}\Big(\hat{a}\hat{\sigma}_{+,j} + \hat{a}^{\dagger}\hat{\sigma}_{-,j}\Big). \quad (4)$$

其中耦合系数重整为 $\tilde{g}_0 = g_0\sqrt{N}$。上式（4）被称为 Dicke 哈密顿量。自从 Dicke 在理论上预言了上述模型的超辐射相变后，人们对其能谱和波函数进行了仔细的研究。当原子和单模光场共振时，Tavis 和 Cummings 解析地给出了此模型的能谱 [18−20]。所以在文献中，有时又把 Dicke 模型称为 Tavis-Cummings (TC) 模型。借助一些近似方法，后续的研究者得到了此模型在非共振时的能谱 [21]。1973 年，Hepp 和 Lieb 指出此模型在热力学极限下有一个量子相变 [22]，即当耦合强度 $\tilde{g}_0$ 超过临界值 $\tilde{g}_0^{\rm cr} = \sqrt{\omega_{\rm A}\omega_{\rm C}/4}$ 时，腔光场有宏观占据（$\langle\hat{a}^{\dagger}\hat{a}\rangle/N \neq 0$），同时会有有限大小的原子数布居在激发态上。当温度升高时，热涨落会破坏原子之间的相干性，因而其临界强度将随温度的升高而增加（如图 1 所示）。这个转变在文献中也被称为超辐射相变 [22−23]。需要注意的是，这里的超辐射相变是热力学极限下的相变，不同于 Dicke 最初提到的动力学超辐射现象。

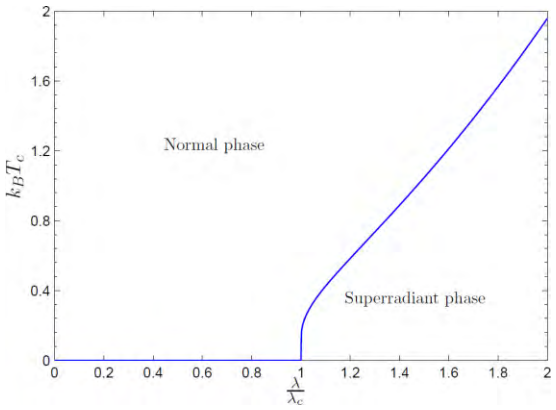

图 1. 热力学极限下 Dicke 模型的超辐射相变 [24]。横轴是相对耦合强度，纵轴是临界温度。图中 $\lambda_{\rm c} = \tilde{g}_0^{\rm cr} = \sqrt{\omega_{\rm A}\omega_{\rm C}/4}$。

在实验上，为了实现强耦合并探索超辐射相变，人们开始研究高品质光腔和原子的耦合体系。将 BEC 置于光腔中，可以实现集体耦合强度 $\sim$ 20 GHz，并产生显著的真空拉比劈裂 [17,25]。但是，由于临界强度 $\tilde{g}_0^{\rm cr} \sim \omega_{\rm A} \sim \omega_{\rm C}$，在光频腔中仍然无法直接观察到超辐射相变。这使得人们思考能否在别的物理构形中实现超辐射相变。其中一个可能是利用双光子拉曼过程，

将原子两个能量接近的基态作为 Dicke 模型中的两能级加以耦合 [26]。这一构想随后在实验中得以实现 [27]。另外，还可以利用 BEC 的相干性，把 BEC 的基态和激发态作为两能级从而实现超辐射相变 [28]。

除了能够显著提高光与物质（原子）相互作用的强度以外，光腔不可避免的耗散同时为光腔–原子耦合系统的研究打开了一扇新的大门 — 非平衡态。在这个系统中，原子散射腔光场，后者反过来又改变原子气体的状态，同时腔光场又不断耗散到环境。最终，耦合系统的内部动力学自由度与外部环境达到动力学非平衡稳态 (dynamical nonequilibrium steady state)。不断耗散出来的光子，不仅会影响系统的稳态，同时也提供了一个非破坏 (non-demolition) 观察原子体系演化的绝佳途径。

对这个系统的描述，除了要考虑原子的内禀自由度与光场之间的耦合，还要考虑光场强度随空间的变化、原子的质心运动、原子的自发辐射和腔的耗散等过程 [29]。在旋波近似下，原子与光场之间的耦合由 JC 模型给出

$$\hat{H}_{\rm JC} = -\Delta_{\rm pa}\hat{\sigma}^{+}\hat{\sigma}^{-} - \Delta_{\rm pc}\hat{a}^{\dagger}\,\hat{a} + g_{\rm c}u_{\rm c}(\boldsymbol{r})\hat{a}\hat{\sigma}^{+} + g_{\rm c}^{*}u_{\rm c}^{*}(\boldsymbol{r})\hat{a}^{\dagger}\hat{\sigma}^{-}. \tag{5}$$

这里 $u_{\rm p}$ ($u_{\rm c}$) 表示驱动光（腔光场）的波模。例如对驻波而言，$u_{\rm p,c}(\boldsymbol{r}) = \cos(\boldsymbol{k}_{\rm p,c}\boldsymbol{r})$，其中 $\boldsymbol{k}_{\rm p}$ 和 $\boldsymbol{k}_{\rm c}$ 分别表示驱动光和腔光场的波矢。另外，上式中 $g_{\rm c}$ 代表单光子拉比频率，驱动光相对于原子跃迁频率和腔模的失谐分别为 $\Delta_{\rm pa} = \omega_{\rm p} - \omega_{\rm A}$ 和 $\Delta_{\rm pc} = \omega_{\rm p} - \omega_{\rm C}$。原子的质心运动由以下哈密顿量描述

$$\hat{H}_{\rm mech} = \frac{\hat{p}^2}{2m} + V_{\rm ext}(\boldsymbol{r}). \tag{6}$$

其中 $V_{\rm ext}(\boldsymbol{r})$ 包含所有的外加约束势和光晶格势。 驱动光的动力学哈密顿量则具有以下的形式

$$\hat{H}_{\rm pump} = i\eta_{\rm c}\big(\hat{a}^{\dagger} - \hat{a}\big) + \Omega_{\rm p}u_{\rm p}(\boldsymbol{r})\hat{\sigma}^{+} + \Omega_{\rm p}^{*}u_{\rm p}^{*}(\boldsymbol{r})\hat{\sigma}^{-}. \tag{7}$$

注意上式中包含了两种驱动方式，一种是驱动光直接照射在原子气体上（即原子驱动，atom pumping，驱动光和原子耦合的强度为 $\Omega_{\rm p}$），另一种驱动光直接驱动腔模，并间接耦合原子气体（即腔驱动，cavity pumping，驱动光和腔的耦合强度为 $\eta_{\rm c}$）。在理论研究中，一般我们只考虑一种驱动方式，即单纯的原子驱动（$\eta_{\rm c} = 0$, $\Omega_{\rm p} \neq 0$）或单纯的腔驱动（$\eta_{\rm c} \neq 0$, $\Omega_{\rm p} = 0$）。综上所述，描述原子气体单粒子动力学行为的哈密顿量为 $\hat{H}_0(\boldsymbol{r}) = \hat{H}_{\rm JC} + \hat{H}_{\rm mech} + \hat{H}_{\rm pump}$。

在实验中，我们通常把一团处于简并温度以下的超冷原子气体置于光学腔中，并在垂直于腔轴方向（原子驱动）或沿腔轴方向（腔驱动）用频率为 $\omega_{\rm p}$ 的激光驱动，同时使驱动激光频率相对于原子的共振频率 $\omega_{\rm A}$ 的失谐远远大于原子激发态的线宽，即 $|\Delta_{\rm pa}| = |\omega_{\rm A} - \omega_{\rm p}| \gg \gamma$。这时，原子处在激发态 $|e\rangle$ 的概率可以忽略，从而可以不考虑自发辐射的影响，原子如一个电偶极矩绝热地跟随光子运动。这个极限被称为色散极限 (dispersion limit)。此时，在驱动光的旋转坐标系下，通过绝热消除哈密顿量 $\hat{H}_0(\boldsymbol{r})$ 中原子的激发态自由度，腔–原子耦合系统的单粒子哈密顿量 $\tilde{H}_0(\boldsymbol{r})$ 可以写为：

$$\tilde{H}_0(\boldsymbol{r}) = \frac{\hat{\boldsymbol{p}}^2}{2m} + V_{\rm ext}(\boldsymbol{r}) - \Delta_{\rm pc}\hat{a}^{\dagger}\hat{a} + i\eta_{\rm c}\big(\hat{a}^{\dagger} - \hat{a}\big) + \frac{1}{\Delta_{\rm pa}}\left[\Omega_{\rm p}u_{\rm p}(\boldsymbol{r}) + g_{\rm c}u_{\rm c}(\boldsymbol{r})\hat{a}^{\dagger}\right]\left[\Omega_{\rm p}^{*}u_{\rm p}^{*}(\boldsymbol{r}) + g_{\rm c}^{*}u_{\rm c}^{*}(\boldsymbol{r})\hat{a}\right]. \tag{8}$$

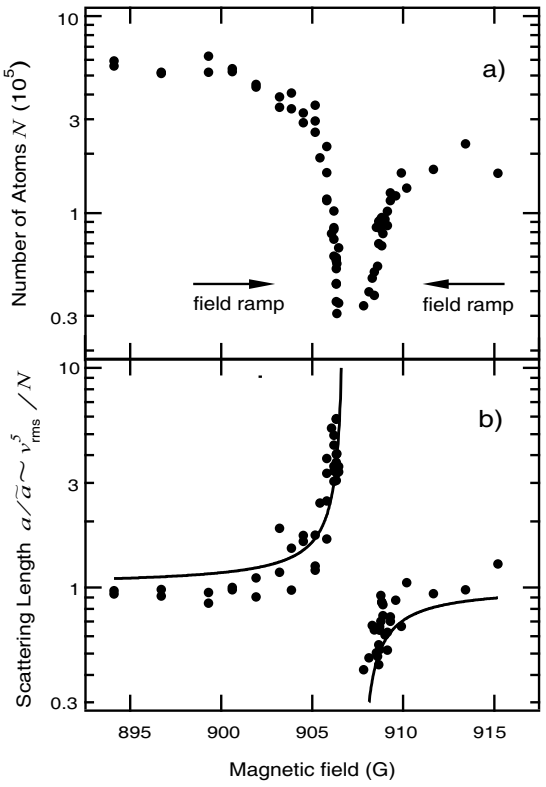

图 2. 原子气体中的 Feshbach 共振。上图是超冷玻色气体在不同磁场下的粒子数。可以看到在共振点附近，由于散射长度发散导致三体损失增大，原子数量大幅减少。下图是通过飞行时间 (time-of-flight) 荧光成像技术反推出的 a_s 散射长度。该图来自参考文献 [30]。

除了单粒子的动力学行为，原子之间的相互作用

对原子系综的性质也有非常重要的影响。原子之间的相互作用在真实的系统中是广泛存在的，相互作用形式往往千差万别，不同组分，不同温度甚至不同维度都会改变相互作用的形式。一般而言，两个碱金属原子进行散射时，它们之间的短程相互作用主要受最外层电子库仑相互作用影响，而长程相互作用主要来自诱导的偶极相互作用，即范德瓦尔斯势 $V(r) \propto 1/r^6$。在研究两个原子的散射问题时，如果体系的角动量守恒，可以利用分波法将散射过程分为 s-，p-，d- 波等。当原子气体的温度足够低的时候，由于复杂的短程相互作用被离心势所屏蔽，原子之间的散射将主要受长程相互作用影响。通过仔细的研究，人们发现当气体的温度足够低 ($\sim$ nK) 且密度足够稀薄 ($\sim 10^{13}-10^{15}\mathrm{cm}^{-3}$) 时，只用一个参数 — s 波散射长度 a_s — 就可以完全刻画原子之间的相互作用。此时，原子之间的相互作用可以用一个简单的接触势近似描述

$$V(\boldsymbol{r}'-\boldsymbol{r}) = U_\mathrm{s}\delta(\boldsymbol{r}'-\boldsymbol{r}) = \frac{4\pi\hbar a_\mathrm{s}}{m}\delta(\boldsymbol{r}'-\boldsymbol{r}). \tag{9}$$

随着对 Feshbach 共振技术的挖掘和利用，人们发现可以通过外磁场调节 s 波散射长度

$$a_s(B) = a_\mathrm{bg}\left(1-\frac{\Delta}{B-B_0}\right). \tag{10}$$

这里的 a_bg 是原子之间的背景散射长度，B_0 是 Feshbach 共振发生的位置，Δ 为共振宽度。从公式 (10) 明显看出，散射长度 a_s 可以从 $-\infty$ 连续地调节到 $+\infty$，从而实现对相互作用强度 U_s 的调节。1998 年，Inouye [30] 等在钠原子 (^{23}Na) BEC 中观察到了 Feshbach 共振（见图 2 ）。

此外，在温度接近量子简并温度时，原子的量子统计规律也会显著影响体系的性质。在超冷原子气体中，由于原子的德布罗意波长 $\lambda_\mathrm{d} = \sqrt{h^2/3mk_\mathrm{B}T}$ 和原子间距 d 量级接近，原子变得不可区分，这时玻色子和费米子的多体波函数分别具有偶宇称和奇宇称。这种对称性的要求将极大地改变系统的热力学和动力学行为。对于玻色子，由于玻色统计允许多个粒子占据同一个量子态，当温度足够低时，所有玻色子凝聚在能量最低的状态 — 玻色–爱因斯坦凝聚，相干效应使得原子气体表现得像一个原子。而对于费米子，由于泡利不相容原理，同一个量子态只允许最多占据一个粒子，体系会形成费米面，并在相互作用的影响下表现出超导、磁性等丰富多彩的性质。

在研究多体系统时，一个常用的方案是使用二次量子化语言。这时，玻色子和费米子分别满足对易关系如下：

$$\begin{aligned}
[\hat{\Psi}(\boldsymbol{r}),\hat{\Psi}^\dagger(\boldsymbol{r})] &= \hat{\Psi}(\boldsymbol{r})\hat{\Psi}^\dagger(\boldsymbol{r}') - \hat{\Psi}^\dagger(\boldsymbol{r}')\hat{\Psi}(\boldsymbol{r}) \\
&= \delta(\boldsymbol{r}-\boldsymbol{r}'), \quad \text{玻色} \\
\{\hat{\Psi}(\boldsymbol{r}),\hat{\Psi}^\dagger(\boldsymbol{r})\} &= \hat{\Psi}(\boldsymbol{r})\hat{\Psi}^\dagger(\boldsymbol{r}') + \hat{\Psi}^\dagger(\boldsymbol{r}')\hat{\Psi}(\boldsymbol{r}) \\
&= \delta(\boldsymbol{r}-\boldsymbol{r}'), \quad \text{费米}
\end{aligned} \tag{11}$$

上式中 $\hat{\Psi}(\boldsymbol{r})$ 和 $\hat{\Psi}^\dagger(\boldsymbol{r})$ 分别表示 $\boldsymbol{r}$ 处的湮灭和产生算符。在这个记号下，单原子哈密顿量写作

$$\hat{H}_0 = \int \mathrm{d}\boldsymbol{r}\hat{\Psi}^\dagger(\boldsymbol{r})\tilde{H}_0(\boldsymbol{r})\hat{\Psi}(\boldsymbol{r}). \tag{12}$$

原子间的 s 波相互作用则写为

$$\hat{H}_\mathrm{int} = \begin{cases} \dfrac{U_\mathrm{s}}{2}\displaystyle\int \mathrm{d}\boldsymbol{r}\hat{\Psi}^\dagger(\boldsymbol{r})\hat{\Psi}^\dagger(\boldsymbol{r})\hat{\Psi}(\boldsymbol{r})\hat{\Psi}(\boldsymbol{r}) & \text{玻色} \\ 0 & \text{费米} \end{cases} \tag{13}$$

注意由于交换反对称性的限制，同组分费米子之间的 s 波相互作用被禁戒。这样，腔–原子体系的整体哈密顿量为 $\hat{H}_\mathrm{tot} = \hat{H}_0 + \hat{H}_\mathrm{int}$。

由于光腔是一个耗散系统，光子主要通过原子的自发辐射和光腔的耗散损失。这两项耦合一般可以通过量子主方程刻画：

$$\frac{\partial\hat{\rho}}{\partial t} = -i\left[H_\mathrm{tot},\hat{\rho}\right] + \left(\mathcal{L}_\mathrm{cav}+\mathcal{L}_\mathrm{atom}\right)\hat{\rho}. \tag{14}$$

式中 $\hat{\rho}$ 代表光和原子复合系统的总密度矩阵，$\mathcal{L}_\mathrm{cav}$ 和 $\mathcal{L}_\mathrm{atom}$ 分别刻画腔和原子的耗散，在 Born-Markov 近似下，分别写作：

$$\mathcal{L}_\mathrm{cav} = -\kappa\Big(\hat{a}^\dagger\hat{a}\hat{\rho} + \hat{\rho}\hat{a}^\dagger\hat{a} - 2\hat{a}\hat{\rho}\hat{a}^\dagger\Big), \tag{15}$$

$$\begin{aligned}
\mathcal{L}_\mathrm{atom} = -\gamma\Big(&\hat{\sigma}^\dagger\hat{\sigma}\hat{\rho} + \hat{\rho}\hat{\sigma}^\dagger\hat{\sigma} \\
&- 2\int \mathrm{d}^2\boldsymbol{u}N(\boldsymbol{u})\hat{\sigma}e^{-ik_\mathrm{A}\boldsymbol{u}\cdot\boldsymbol{r}}\hat{\rho}e^{ik_\mathrm{A}\boldsymbol{u}\cdot\boldsymbol{r}}\hat{\sigma}^\dagger\Big).
\end{aligned} \tag{16}$$

其中 κ 是腔的耗散频率，γ 是激发态原子 $|e\rangle$ 的自发辐射几率幅，k_A 是伴随自发辐射原子获得的沿 $\boldsymbol{u}$ 方向的反冲动量，$N(\boldsymbol{u})$ 是散射光子的角分布函数。为了使得原子对驱动光的散射最有效，实验中通过调节光腔的最低能量模式 TEM_{00} 的频率 ω_C 与驱动光的频率近似共振，即 $|\Delta_\mathrm{pc}| \approx \kappa$。同时，由于横向模式的能级差 $\Delta\nu_\mathrm{T} \gg \kappa$，腔的横向高能模式的影响可以忽略。此外，目前实验已经能够使原子与腔耦合的拉比频率 g_0 达到腔模的线宽 κ 的量级，从而实现了强耦合 $g_0^2/\kappa\gamma \gg 1$ [17,25]。

至此，腔–原子耦合体系的性质可以通过联立求解哈密顿量 (11) 和 (13) 式，以及主方程 (14) 式得到。下面，我们将分别针对玻色和费米气体的情况加以详细讨论。

IV. 光学腔中的超冷玻色气体

在本章中，为了叙述方便并保持物理图像清晰，我们假设驱动方式是原子驱动，即 $\eta_{\rm c}=0$ 而 $\Omega_{\rm p}\neq 0$，并且假设驱动光的波矢 $\boldsymbol{k}_{\rm p}$ 垂直于腔轴。在这种情况下，体系的总哈密顿量简化为

$$\begin{aligned}\hat{H}_{\rm tot}=&-\Delta_{\rm pc}\hat{a}^{\dagger}\hat{a}+\frac{U_s}{2}\int {\rm d}\boldsymbol{r}\hat{\Psi}^{\dagger}(\boldsymbol{r})\hat{\Psi}^{\dagger}(\boldsymbol{r})\hat{\Psi}(\boldsymbol{r})\hat{\Psi}(\boldsymbol{r})\\&+\int {\rm d}\boldsymbol{r}\hat{\Psi}^{\dagger}(\boldsymbol{r})\Bigg\{\frac{\hat{\boldsymbol{p}}^2}{2m}+V_{\rm ext}(\boldsymbol{r})\\&+\frac{1}{\Delta_{\rm pa}}\left[\Omega_{\rm p}u_{\rm p}(\boldsymbol{r})+g_{\rm c}u_{\rm c}(\boldsymbol{r})\hat{a}^{\dagger}\right]\\&\left[\Omega_{\rm p}^{*}u_{\rm p}^{*}(\boldsymbol{r})+g_{\rm c}^{*}u_{\rm c}^{*}(\boldsymbol{r})\hat{a}\right]\Bigg\}\hat{\Psi}(\boldsymbol{r}).\end{aligned}\tag{17}$$

原子算符和光场算符的动力学演化过程由海森堡方程决定

$$\begin{aligned}i\partial_t\hat{\Psi}(\boldsymbol{r},t)=&[\hat{\Psi}(\boldsymbol{r},t),H_{\rm tot}]_-\\=&\Bigg[\frac{\hat{\boldsymbol{p}}^2}{2m}+V_{\rm ext}(\boldsymbol{r})+\frac{1}{\Delta_{\rm pa}}(\Omega_{\rm p}u_{\rm p}(\boldsymbol{r})\\&+g_{\rm c}u_{\rm c}(\boldsymbol{r})\hat{a}^{\dagger})(\Omega_{\rm p}^{*}u_{\rm p}^{*}(\boldsymbol{r})+g_{\rm c}^{*}u_{\rm c}^{*}(\boldsymbol{r})\hat{a})\Bigg]\hat{\Psi}(\boldsymbol{r},t)\\&+U_{\rm s}\hat{\Psi}^{\dagger}(\boldsymbol{r},t)\hat{\Psi}(\boldsymbol{r},t)\hat{\Psi}(\boldsymbol{r},t),\\i\partial_t\hat{a}(t)=&[\hat{a}(t),\hat{H}_{\rm tot}]_--i\kappa\hat{a}(t)\\=&\int {\rm d}\boldsymbol{r}\left[\frac{|g_{\rm c}|^2}{\Delta_{\rm pa}}|u_{\rm c}(\boldsymbol{r})|^2\hat{a}(t)+\frac{\Omega_{\rm p}^{*}g_{\rm c}}{\Delta_{\rm pa}}u_{\rm p}^{*}(\boldsymbol{r})u_{\rm c}(\boldsymbol{r})\right]\\&\Psi^{\dagger}(\boldsymbol{r},t)\hat{\Psi}(\boldsymbol{r},t)-(\Delta_{\rm pc}+i\kappa)\hat{a}(t).\end{aligned}\tag{18}$$

注意在上式中，我们唯象地引入了光场的耗散项 $-i\kappa\hat{a}$。

在温度足够低且腔光场的光子数足够多的时候，原子和光场的涨落以及它们之间的纠缠可以忽略不计 [31,32]，这时体系的描述变得极为简单：原子处在玻色–爱因斯坦凝聚态，而光场处在一个相干态（或者真空态）。这时，可以对算符做如下近似 $\hat{\Psi}(\boldsymbol{r},t)\to\psi(\boldsymbol{r},t)$，$\hat{a}(t)\to\alpha(t)$，并得到腔-BEC系统的含时动力学演化方程 (Time-dependent Gross-Pitaevskii equation，TDGP equation)。为描述原子系综和光场的耦合效果，我们定义 $\tilde{\Delta}_{\rm pc}=\Delta_{\rm pc}-N\xi_{\rm c}B$ 代表原子感受到的有效失谐，其中 N 为总原子数，$\xi_{\rm c}=g_{\rm c}^2/\Delta_{\rm pa}$，$B\equiv(1/N)\int {\rm d}\boldsymbol{r}\psi^{*}(\boldsymbol{r},t)u_{\rm g}^2(\boldsymbol{r})\psi(\boldsymbol{r},t)$ 描述了原子气体密度与腔光场之间的重叠程度，也被称为 Bunching 参量。如果 $|\tilde{\Delta}_{\rm pc}|\gg\kappa\gg\omega_{\rm R}$，原子气体动力学演化时间 $1/\omega_{\rm R}$ 最为缓慢，而光子从光腔的一侧漏出之前 ($t<1/\kappa$)，光场已经在 $1/\tilde{\Delta}_{\rm pc}$ 的时间尺度内达到动力学稳态。在这样的系统中，原子气体和腔光场相互影响，同时腔光场又通过耗散和环境耦合，最终系统将达到稳态，其稳态方程为

$$\begin{aligned}\alpha=&\frac{N\eta_{\rm p}\Theta}{\tilde{\Delta}_{\rm pc}+i\kappa},\\\mu\psi_0(\boldsymbol{r})=&\left[\frac{\hat{\boldsymbol{p}}^2}{2m}+V_{\rm ext}(\boldsymbol{r})+V_{\rm ad}(\boldsymbol{r})+U_{\rm s}|\psi_0(\boldsymbol{r})|^2\right]\psi_0(\boldsymbol{r}).\end{aligned}\tag{19}$$

其中 μ 是原子气体的化学势，$\eta_{\rm p}=\Omega_{\mathbf{p}}g_{\rm c}^{*}/\Delta_{\rm pa}$。在上式中，序参量 Θ 定义为 $\Theta=(1/N)\int {\rm d}r u_{\rm p}^{*}(\boldsymbol{r})u_{\rm c}(\boldsymbol{r})|\psi_0(\boldsymbol{r})|^2$，对应原子气体的 Z_2 对称性自发破缺。当 $\Theta=0$ 时，原子气体沿腔轴均匀分布；而当 $\Theta=\pm1$ 时，原子气体局限到偶格点 ($kx=2n\pi$) 或者奇格点 ($kx=(2n+1)\pi$)。由于腔光场的有效动力学演化特征时间 $1/\tilde{\Delta}_{\rm pc}$ 远小于原子气体的特征时间，因而原子会感受到一个由光子调制的有效绝热势

$$\begin{aligned}V_{\rm ad}(\boldsymbol{r})=&\frac{1}{\Delta_{\rm pa}}\big(\Omega_{\rm p}u_{\rm p}(\boldsymbol{r})+g_{\rm c}u_{\rm c}(\boldsymbol{r})\alpha^{*}\big)\\&\big(\Omega_{\rm p}^{*}u_{\rm p}^{*}(\boldsymbol{r})+g_{\rm c}^{*}u_{\rm c}^{*}(\boldsymbol{r})\alpha\big)\\=&V_{\rm p}|u_{\rm p}(\boldsymbol{r})|^2+\xi_{\rm c}|\alpha|^2|u_{\rm c}(\boldsymbol{r})|^2+V_{\rm pc}(\boldsymbol{r}).\end{aligned}\tag{20}$$

这里 $V_{\rm p}=|\Omega_{\rm p}|^2/\Delta_{\rm pa}$ 是驱动光诱导的沿驱动方向的光晶格振幅，第二项表示由腔光场诱导的光晶格，其大小依赖于腔光子数 $|\alpha|^2$ 和耦合强度 $\xi_{\rm c}$，最后一项 $V_{\rm pc}(\boldsymbol{r})=\eta_{\rm p}\alpha u_{\rm p}(\boldsymbol{r})u_{\rm c}^{*}(\boldsymbol{r})+\eta_{\rm p}^{*}\alpha^{*}u_{\rm p}^{*}(\boldsymbol{r})u_{\rm c}(\boldsymbol{r})$ 代表腔光场和驱动光之间的相互散射。2007 年，瑞士 ETH 的 Esslinger 小组实现了上述的实验条件 [25]。

A. 自组织及超辐射相变

在腔驱动中，所有的原子都同时和同一个模式的腔光场耦合，腔光场的大小 α 依赖于原子气体的分布，反过来又会影响原子系统状态。在原子驱动下，原子和光场的耦合依赖于空间，不同位置散射的腔光场的振幅和相位也是空间依赖的，且由于相邻格点之间距离为半个波长，散射的光子的相位正好差 π，所以相邻格点散射的腔光场相互抵消。因此，最初人们认为这

样的系统中不会有腔光场的形成。但之后的研究发现，密度涨落（热涨落或者量子涨落）可以辅助腔光场的形成，腔光场反过来正反馈初始的密度涨落，最终使得原子气体在空间上形成周期性分布，腔光场有宏观占据 [33−37]，且原子气体在空间上的分布周期和腔光场的周期一致（Z_2 对称性的破缺） [28,38]。对于原子气体，这种相变被称为自组织 (self-organization)。对于腔光场而言，这种相变被称为超辐射相变。后面我们会说明，在临界点附近，超辐射相变等价于 Dicke 相变。伴随着原子气体形成新的分布，原子的动能也被腔光场通过耗散 κ 带出腔，所以原子气体的温度也会被降低到腔的展宽 κ 的量级 [33,34]。上述现象首先被基于半经典的 Fokker-Planck 方程的数值模拟所预言 [33]。如图 3 所示，随着时间的推移，原子沿腔轴方向的运动最后都被束缚形成棋盘状（checkerboard，见上图），原子气体沿腔轴的温度会由于腔场的耗散效果而降低（见下图）。这一数值结果随后被实验证实 [34]。值得注意的是，对于自组织的形成，原子数或者驱动光强存在一个阈值，只有在阈值之上才可能出现相变 [33,37]。

如同热原子中的自组织相变，玻色–爱因斯坦凝聚体也会有类似的现象。不失一般性，我们用沿腔轴方向束缚的准一维气体（取为 x 方向）进行说明。考虑一个沿 x 方向放置的 FP 腔，腔模为 $u_{\rm c}(x)=\cos(kx)$，腔内原子沿横向方向（垂直于腔轴）的运动被束缚在基态。假设使用沿 y 方向的平面波驱动原子气体，即 $u_{\rm p}(y)=\exp(iky)$，把横向自由度积分后，体系的哈密顿量为

$$\begin{aligned}\hat{H}_{\rm tot}=&-\Delta_{\rm pc}\hat{a}^{\dagger}\hat{a}+\frac{g_{\rm 1D}}{2}\int {\rm d}x\hat{\psi}^{\dagger}(x)\hat{\psi}^{\dagger}(x)\hat{\psi}(x)\hat{\psi}(x)\\&+\int {\rm d}x\hat{\psi}^{\dagger}(x)\Bigg[\frac{-\hbar^2\partial_x^2}{2m}+V_{\rm ext}(x)+\xi_{\rm c}\hat{a}^{\dagger}\hat{a}\cos^2(kx)\\&+\eta_{\rm p}(\hat{a}^{\dagger}+\hat{a})\cos(kx)\Bigg]\hat{\psi}(x).\end{aligned}\tag{21}$$

式中 $g_{\rm 1D}$ 表示原子在一维方向的有效相互作用强度，$V_{\rm ext}(x)$ 是用于约束原子的外加束缚势。简单起见，我们暂时省略 $V_{\rm ext}(x)$ 的影响。方括号中第三项是由腔光场形成的光晶格，最后一项是由原子散射驱动光形成的干涉项，散射的能力由 $\eta_{\rm p}$ 衡量。当 $|\Delta_{\rm pc}|$ 主导整个体系的动力学行为时，光子将绝热地跟随原子气体运动，这时光子的状态为

$$\hat{a}=\frac{\eta_{\rm p}\hat{\Theta}}{\Delta_{pc}-\xi_{\rm c}\hat{B}+i\kappa},\tag{22}$$

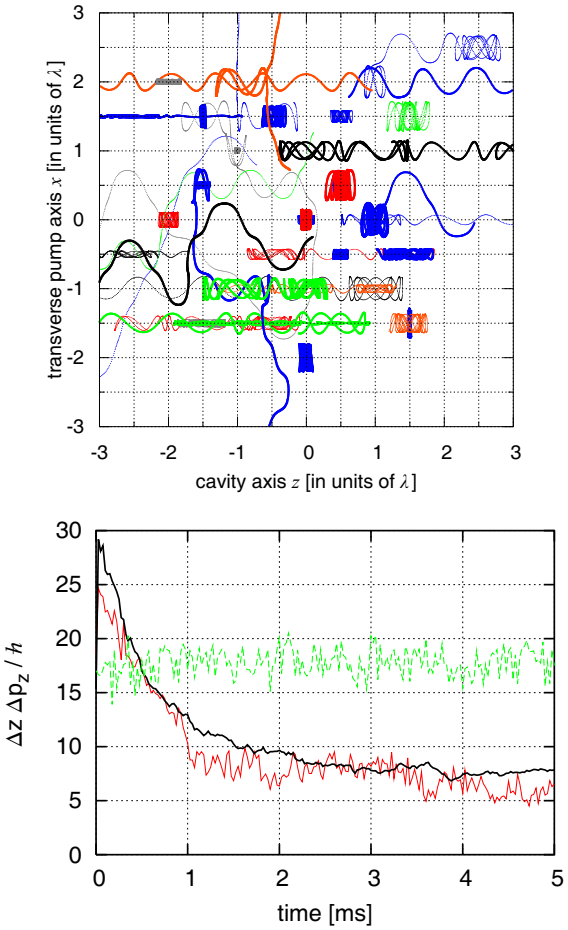

图 3. 上图：在临界驱动强度以上，40 个 ^{85}Rb 原子在前 40 μs 中的运动轨迹。不同颜色代表不同原子，其中大多数原子最终形成棋盘结构的分布。该图来自参考文献 [36]。下图：原子气体沿腔轴的相空间体积（海森堡不确定性）随时间的演化。实（虚）线分别代表在临界强度之上（下）。红色和黑色的实线分别代表原子数为 40 和 160 的情况。该图来自参考文献 [33,36]。

这里 $\hat{\Theta}=\int {\rm d}x\hat{\psi}^{\dagger}(x)\cos(kx)\hat{\psi}(x)$，$\hat{B}=\int {\rm d}x\hat{\psi}^{\dagger}(x)\cos^2(kx)\hat{\psi}(x)$。注意算符 $\hat{\Theta}$ 和 $\hat{B}$ 对易，所以不会有顺序问题。在平均场近似下，腔-原子耦合系统的稳态行为由稳态方程 (22) 和 BEC 的 Gross-Pitaevskii (GP) 方程共同描述

$$\begin{aligned}\alpha=&\frac{\eta_{\rm p}\Theta}{\Delta_{\rm pc}-\xi_{\rm c}B+i\kappa},\\ \mu\psi_0(x)=&\Bigg[\frac{-\hbar^2\partial_x^2}{2m}+\xi_{\rm c}|\alpha|^2\cos^2(kx)\\&+\eta_{\rm p}(\alpha+\alpha^*)\cos(kx)+g_{\rm 1D}|\psi_0(x)|^2\Bigg]\psi_0(x).\end{aligned}\tag{23}$$

这时绝热势中的干涉项为

$$V_{\rm pc}=\frac{2\eta_{\rm p}^2\tilde{\Delta}_{\rm pc}\Theta}{\tilde{\Delta}_{\rm pc}^2+\kappa^2}\cos(kx), \tag{24}$$

且 $\Theta=\int {\rm d}x\cos(kx)|\psi_0(x)|^2$。设光腔和驱动光的有效失谐 $\tilde{\Delta}_{\rm pc}$，以及驱动光相对于原子激发态的失谐 $\Delta_{\rm pa}$ 均为红失谐（$\tilde{\Delta}_{\rm pc},\Delta_{\rm pa}<0$），当驱动光功率很小或者粒子数较少时，由涨落导致的腔光场 $|\alpha|$ 较小（特别是高温时），导致 $V_{\rm pc}(x)$ 不足以长时间束缚原子 [37]。这时由于被不同位置的原子散射的腔光场随机抵消，此时腔内将没有宏观数目的腔光子。但是，随着驱动光的功率不断增强，等效的 $|\eta_{\rm p}|$ 随之增大，量子涨落将越来越强。可以设想，某时刻涨落足以使原子气体更多地局限在偶格点 $kx=2n\pi$ （$\Theta>0$），而 $V_{\rm pc}(x)$ 将在偶数格点极小而在奇数格点 $kx=(2n+1)\pi$ （$\Theta<0$）极大，使得奇数格点的原子被更多地吸引到偶数格点。而光子的布拉格散射将放大最初的涨落使得原子被更多地吸引到偶数格点。这样的放大过程最终被相互作用（气体稠密）或者动能（气体稀薄）所平衡，因为这两种作用都倾向于原子均匀分布。类似地，原子也可以汇聚到奇数格点。 图 4 展示了 BEC 在横向平面波驱动下，在临界值 $\eta_{\rm p}^{\rm cr}$ 之上发生的自组织相变。可以看到当驱动光超过一定临界值后，相干性迅速建立，$V_{\rm pc}(x)$ 振幅增加，原子的波函数在空间上越来越局域化。注意对于单分量的玻色气体而言，超辐射现象依赖于腔光场对原子气体密度涨落的正反馈，这要求 $\tilde{\Delta}_{\rm pc}$ 和 $\Delta_{\rm pa}$ 必须为红失谐。如果不是红失谐，则腔光场将压制原子气体的密度涨落，超辐射相将被抑制。

这种腔–原子耦合体系中的自组织现象与光晶格中玻色气体的超流–莫特 (Mott) 绝缘体相变是不同的。一方面，前者在形成自组织现象的初期（$\eta_{\rm p}\gtrsim\eta_{\rm p}^{\rm cr}$），原子的波函数并没有完全的局域化；另一方面，即使在深自组织区域（$\eta_{\rm p}\gg\eta_{\rm p}^{\rm cr}$）时，气体的压缩率依然不为零（莫特绝缘体压缩率为零）；最后，研究显示在热力学极限下，无论驱动光多强，总有一部分原子分布在原子数较少的格点 [36]。

上述 BEC 的自组织现象也可以通过 Dicke 相变来理解。在原子间相互作用比较弱的情况下，当玻色气体处于 BEC 状态时，原子大部分凝聚在 $|k=0\rangle$ 的状态。原子吸收一个光子变为 $|k=\pm k_{\rm R}\rangle$，而此态正好可以加强光子的布拉格散射，使得更多的光子进入腔中。当驱动光强度 $\eta_{\rm p}$ 在临界点附近时，腔光场较弱，原子被散射到更高动量的概率很小，因而把 BEC 的波函数

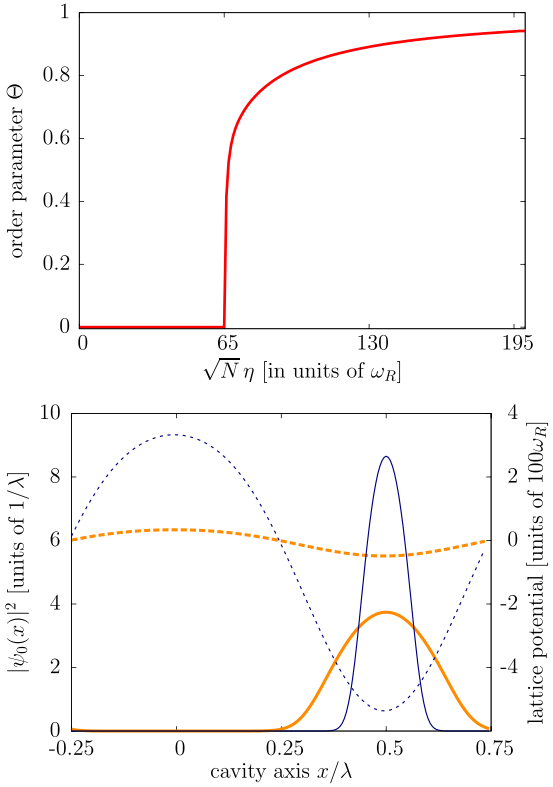

图 4. 上图：腔-BEC 耦合系统超辐射序参量 Θ 随驱动光强的变化。当驱动强度超过临界值 $\sqrt{N}\eta_{\rm p}^{\rm cr}=65.6\omega_{\rm R}$ 后，伴随着腔光场的建立，序参量的出现意味着原子沿腔轴形成周期的分布，破坏了原有的 Z_2 对称性。下图：在超辐射相中对应于驱动强度分别为 $\sqrt{N}\eta_{\rm p}=100\omega_{\rm R}$（黄粗线）和 $\sqrt{N}\eta_{\rm p}=300\omega_{\rm R}$ （蓝细线）时，原子波函数 $|\psi_0(x)|^2$ （实线）以及相应的由腔光场产生的绝热光学势 $\xi_{\rm c}|\alpha|^2\cos^2(kx)+V_{\rm pc}(x)$（虚线）在空间的分布。图中所用参数为 $\mu_0=10\hbar\omega_{\rm R}\lambda$，$N\xi_{\rm c}=-100\omega_{\rm R}$，$\Delta_{\rm pc}=-300\omega_{\rm R}$。该图来自参考文献 [37]。

写作

$$\hat{\psi}(x)=\sqrt{\frac{1}{L}}\hat{C}_0+\sqrt{\frac{2}{L}}\hat{C}_1\cos(k_{\rm R}x). \tag{25}$$

式中 L 表示原子气体的尺寸，原子总数 $N=\hat{C}_0^\dagger\hat{C}_0+\hat{C}_1^\dagger\hat{C}_1$ 是守恒量。引入 Schwinger 表象 $\hat{S}_+=\hat{S}_-^\dagger=\hat{C}_1^\dagger\hat{C}_0$ 和 $\hat{S}_z=1/2(\hat{C}_1^\dagger\hat{C}_1-\hat{C}_0^\dagger\hat{C}_0)$，可以得到如下等效双模哈密顿量

$$\hat{H}=-\tilde{\Delta}_{\rm pc}\hat{a}^\dagger\hat{a}+\omega_{\rm R}\hat{S}_z+\frac{\tilde{\eta}_{\rm p}}{\sqrt{N}}(\hat{a}^\dagger+\hat{a})\left(\hat{S}_++\hat{S}_-\right)+\frac{\xi_{\rm c}N}{4}\hat{a}^\dagger\hat{a}\left(\frac{1}{2}+\frac{\hat{S}_z}{N}\right)+\omega_{\rm R}N. \tag{26}$$

这里，算符 $\hat{C}_0$ 或 $\hat{C}_1$ 代表湮灭一个动量为 0 或 $\pm k_{\rm R}$ 的粒子， $\tilde{\Delta}_{\rm pc}=\Delta_{\rm pc}-N\xi_{\rm c}/2$，$\tilde{\eta}_{\rm p}=\sqrt{N}\eta$。 哈密顿量 (26) 式 的第一项描述原子气体对腔共振频率的移动，第二项描述原子吸收或者放出一个光子所获得的反冲

动能 $\omega_{\rm R}$，第三项是原子和光场之间的相互作用。这三项正好对应的就是 Dicke 模型。第四项表示原子对腔共振频率的动力学移动，在相变点附近可以被忽略。

此外，通过虚时演化分析不含时 GP 方程 (23) 式可以得到其临界驱动光强度。在相变点附近，假定原子的波函数为 $\psi(x)=\psi_0(x)[1+\epsilon\cos(k_{\rm R}x)]$，$\epsilon$ 为无穷小量，则正常态失稳的条件就是激发态的衰减速率慢于基态的衰减速率。由此得到临界驱动光强为

$$\tilde{\eta}_{\rm p}^{\rm cr}=\sqrt{N}\eta_{\rm p}^{\rm cr}=\frac{1}{\sqrt{2}}\sqrt{\frac{\tilde{\Delta}_{\rm pc}^2+\kappa^2}{-\tilde{\Delta}_{\rm pc}}(\omega_{\rm R}+2\mu_0)}. \tag{27}$$

令 $g_{\rm cr}=\sqrt{N}\eta_{\rm p}^{\rm cr}$，$\omega_{\rm C}=-\tilde{\Delta}_{\rm pc}$，$\omega_{\rm A}=2(\omega_{\rm R}+2\mu_0)$（考虑了由于相互作用导致的能级移动），上式恰好是开放系统 Dicke 哈密顿量发生超辐射相变的临界值

$$g_{cr}=\sqrt{\frac{\omega_{\rm C}^2+\kappa^2}{4\omega_{\rm C}}\omega_{\rm A}}. \tag{28}$$

综上所述，该体系中的自组织（超辐射）相变可以被归为 Dicke 相变一类。

B. 元激发

在这一节里，我们将运用一阶线性涨落理论分析腔-BEC 耦合系统的一阶线性激发谱。在临界点附近，腔光场很小，此时原子体系只有一小部分被激发到 $\cos(k_{\rm R}x)$ 的状态 [39,40]，二能级近似的条件成立 [39,41]。当进入较深的超辐射相时，原子的更高激发态也将被显著激发。类比于凝聚态物理中的极化子，与腔光场耦合的低能激发被称为极化激元 (polariton) [37,41]。在临界点附近，最低能量的极化激元在动量 $|k|=k_{\rm R}$ 附近的能隙逐渐软化，直到临界点时变为零，这一支特殊的极化激元又被称为旋子 (roton) [42,43]。在临界点附近，人们发现旋子激发谱的临界指数为 -1，而不是封闭系统 Dicke 模型预言的 $-1/2$ [41,44,45]。产生这个区别的原因是由于腔-BEC 耦合系统的低能激发通过与腔光场的耦合获得了耗散的特性。这也使得人们可以通过直接测量耗散光子无损地探测原子体系量子态。在实验上，原子体系的耗散要比预期的大 [46]，这是因为有限尺寸效应耦合了原子不同的集体激发模 [43]。

为了简单起见，我们仍然采用上一节的一维模型。同时，为了抓住腔和物质之间耦合的物理，暂时忽略原子之间的相互作用。由于（26）式中最后一项可以忽略，我们可以考虑其对应的 Dicke 模型的稳态解。令 $\alpha=\langle\hat{a}\rangle$，$\beta=\langle\hat{S}_-\rangle$，$w=\langle\hat{S}_z\rangle$，可以得到

$$\begin{aligned}
i\partial_t\alpha&=(-\tilde{\Delta}_{pc}-i\kappa)\alpha+\frac{\tilde{\eta}_{\rm p}}{\sqrt{N}}(\beta^*+\beta),\\
i\partial_t\beta&=\omega_{\rm R}\beta+2\frac{\tilde{\eta}_{\rm p}}{\sqrt{N}}(\alpha^*+\alpha)w,\\
i\partial_t w&=\frac{\tilde{\eta}_{\rm p}}{\sqrt{N}}(\alpha^*+\alpha)(\beta^*-\beta).
\end{aligned} \tag{29}$$

这里 $w^2+|\beta|^2=N^2/4$ 为守恒量。上面这个方程组始终有一个平庸解 $\alpha=\beta=0$ 和 $w=-N/2$，代表腔内没有光子，同时所有的原子都处于其基态 $k=0$。但是当 $\tilde{\eta}_{\rm p}>\tilde{\eta}_{\rm p}^{\rm cr}=1/\sqrt{2}\sqrt{\left(\tilde{\Delta}_{\rm pc}^2+\kappa^2\right)\omega_{\rm R}/(-\tilde{\Delta}_{\rm pc})}$ 时，将出现另外一个解，即腔内出现宏观占据的光子和部分原子处于激发态 $k=k_{\rm R}$，这时有

$$\begin{aligned}
\alpha&=\pm\sqrt{N}\frac{\tilde{\eta}_{\rm p}}{-\tilde{\Delta}_{\rm pc}-i\kappa}\sqrt{1-\left(\frac{\tilde{\eta}_{\rm p}^{\rm cr}}{\tilde{\eta}_{\rm p}}\right)^4},\\
\beta&=\mp\frac{N}{2}\sqrt{1-\left(\frac{\tilde{\eta}_{\rm p}^{\rm cr}}{\tilde{\eta}_{\rm p}}\right)^4},\\
w&=-\frac{N}{2}\left(\frac{\tilde{\eta}_{\rm p}^{\rm cr}}{\tilde{\eta}_{\rm p}}\right)^2.
\end{aligned} \tag{30}$$

由于在临界点附近，原子被激发到激发态 $k=\pm k_{\rm R}$ 的概率很小，可以引入 Holstein–Primakoff 变换：$\hat{S}_z=\hat{b}^\dagger\hat{b}-N/2$，$\hat{S}_+=\hat{b}^\dagger\sqrt{N-\hat{b}^\dagger\hat{b}}$，$\hat{S}_-=\hat{S}_+^\dagger$。这里 $\hat{b}$ 是新的玻色场，满足对易关系 $[\hat{b},\hat{b}^\dagger]=1$。在热力学极限下，涨落很小，其激发谱可以用线性涨落的方式考虑：当 $\tilde{\eta}_{\rm p}<\tilde{\eta}_{\rm p}^{\rm cr}$ 时（即正常相），

$$\hat{H}_{\rm ex}^N=-\tilde{\Delta}_{\rm pc}\hat{a}^\dagger\hat{a}+\omega_{\rm R}\hat{b}^\dagger\hat{b}+\tilde{\eta}_{\rm p}(\hat{a}^\dagger+\hat{a}))(\hat{b}^\dagger+\hat{b}). \tag{31}$$

当 $\tilde{\eta}_{\rm p}\gtrsim\tilde{\eta}_{\rm p}^{\rm cr}$ 时（即超辐射相），经过变换 $\hat{a}\to\alpha+\hat{c}$ 和 $\hat{d}=\beta/\sqrt{N}+\hat{d}$，可得

$$\begin{aligned}
\hat{H}_{\rm ex}^{\rm SR}=&-\tilde{\Delta}_{\rm pc}\hat{c}^\dagger\hat{c}+\omega_{\rm R}\hat{d}^\dagger\hat{d}+g_{\rm cd}(\hat{c}^\dagger+\hat{c}))(\hat{d}^\dagger+\hat{d})\\
&+g_{\rm dd}(\hat{d}^\dagger+\hat{d})^2.
\end{aligned} \tag{32}$$

这里的耦合参数 $g_{\rm cd}=\tilde{\eta}_{\rm p}/8\big(5+3(\tilde{\eta}_{\rm p}^{\rm cr}/\tilde{\eta}_{\rm p})^4\big)$，$g_{\rm dd}=\omega_{\rm R}/8\big((\tilde{\eta}_{\rm p}/\tilde{\eta}_{\rm p}^{\rm cr})^2-(\tilde{\eta}_{\rm p}^{\rm cr}/\tilde{\eta}_{\rm p})^2\big)$。在 $\omega_{\rm R}\ll\kappa\ll|\tilde{\Delta}_{\rm pc}|$ 时，激发谱为

$$\begin{aligned}
\omega_{\rm ex}=&\omega_{\rm R}\sqrt{1-\left(\frac{\tilde{\eta}_{\rm p}}{\tilde{\eta}_{\rm p}^{\rm cr}}\right)^2}\left[1+\frac{1}{2}\frac{\omega_{\rm R}^2}{\tilde{\Delta}_{\rm pc}^2+\kappa^2}\left(\frac{\tilde{\eta}_{\rm p}}{\tilde{\eta}_{\rm p}^{\rm cr}}\right)^2\right]\\
&-i\frac{\kappa\omega_{\rm R}^2}{\tilde{\Delta}_{\rm pc}^2+\kappa^2}\left(\frac{\tilde{\eta}_{\rm p}}{\tilde{\eta}_{\rm p}^{\rm cr}}\right)^2.
\end{aligned} \tag{33}$$

激发谱的频率为 $\mathrm{Re}(\omega_{\rm ex})$，而其耗散为 $\mathrm{Im}(\omega_{\rm ex})$。当 $\tilde{\eta}_{\rm p}=0$，激发谱 $\omega_{\rm ex}=\omega_{\rm R}$，代表 BEC 的第一个

集体激发频率。而当 $\tilde{\eta}_{\rm p}$ 越来越趋近于 $\tilde{\eta}_{\rm p}^{\rm cr}$ 时，其激发谱的频率也逐渐变为零，说明 BEC 逐渐获得了光子的性质。

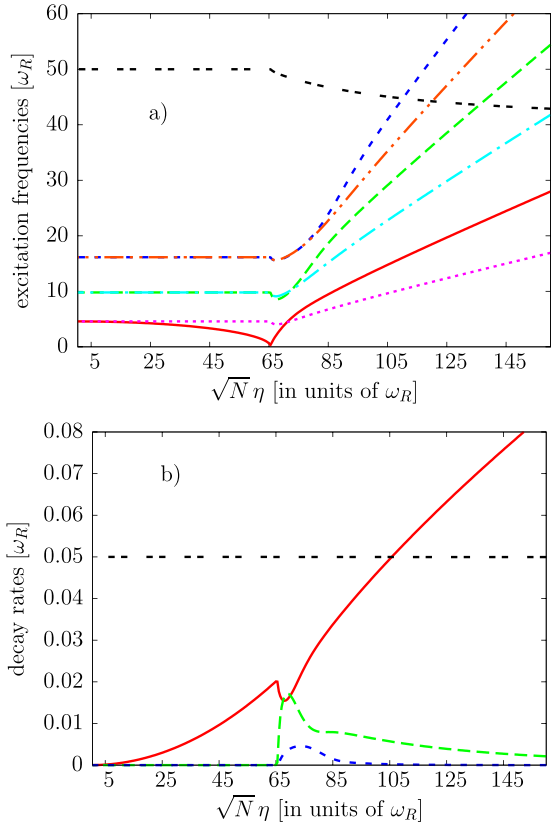

图 5. 腔-BEC 系统中低能激发的 (a) 激发频率 $\mathrm{Re}(\omega_{\rm ex})$ 和 (b) 耗散率 $\mathrm{Im}(\omega_{\rm ex})$。图中展示了能量最低的 6 支 BEC 主导（类原子）和 1 支腔主导（类腔）的集体激发模式。图 (a) 和图 (b) 的颜色一一对应。为了比较方便，类腔模式的激发频率和耗散率分别被除以 5 和 4000（黑色双虚线），能量最低的类原子模式（红实线）的耗散率 γ_1 也被除以 2。其余的参数与图 4 的上图相同。该图来自参考文献 [37]。

随着驱动光的增强，BEC 的更高能级集体激发也会有宏观占据，两能级近似将变得不再适用，此时需要考虑更多激发态的影响 [37,40]。图 5 展示了腔-BEC 耦合系统中集体激发谱随驱动光强度 $\tilde{\eta}_{\rm p}=\sqrt{N}\eta$ 的变化趋势。在临界点 $\sqrt{N}\eta=\tilde{\eta}_{\rm p}=\tilde{\eta}_{\rm p}^{\rm cr}$（这里取 65.612 $\omega_{\rm R}$）以下，BEC 的激发谱（类原子）是两重兼并的。在正常相中，BEC 的每一个集体激发有一支（图 5 中洋红点线、靛蓝点虚线、红双点划线）与腔模脱耦，即使进入自组织区域，它们也只与 BEC 的其它模式耦合，因此耗散率始终为零；而类原子激发中能量最低的一支（图 5 中红实线）则与腔模耦合，混合了原子的集体激发和腔光场在稳态附近的涨落。我们可以看到类原子的这支激发频率（红实线）随着驱动光强增强而逐渐软化，在临界点上激发态能量变为零，而耗散率变为有限值（在临界点附近耗散率的小凹陷是由于数值精度造成的），意味着系统的能隙关闭从而导致相变发生。这些结果进一步佐证了前面关于两模 Dicke 模型的讨论。

随着驱动光强 η 的继续增大，类原子的高能集体激发模式也会与腔模耦合，从而获得了光子的耗散特性（绿虚线和蓝虚线）。但是在强驱动光极限 $\eta\to\infty$ 时，所有原子都被局限到腔模的波谷位置，导致只有 BEC 的第二支集体激发（红实线）能与腔模耦合。因此，除了这一支获得有限的耗散率，其余的两支（包括能量更高的）的耗散速率都将变为零（绿虚线和蓝虚线）。这三支都混合了 BEC 的集体激发和腔光场在稳态附近的涨落，这一点与固体物理中类光声子和光子之间耦合形成极化激元的过程是类似的。在这个意义上，这三支激发谱又被称为极化激元。在强驱动极限下，由于所有原子都会感受到一个简谐势 $\tilde{\eta}_{\rm p}\cos(k_{\rm R}x)\approx\tilde{\eta}_{\rm p}k_{\rm R}^2x^2$，因此其激发频率将变为等间距的简谐振子的频谱。

类原子激发谱中能量最低的一支（红实线）代表着腔-BEC 耦合系统的第一激发态的能隙。由于其动量为 $k_{\rm R}$ 且其激发频率在临界点附近被软化，因而这一支极化激元也具有旋子的特征 [42,43]。2012 年，Esslinger 小组通过布拉格光谱的方法，实际测量了二维体系中极化激元的能隙随着驱动光光强变化的趋势（图 6）。实验同时测量了处于激发态 $|k_x=\pm k_{\rm R},k_z=\pm k_{\rm R}\rangle$ 的原子数 $N_{\rm e}$ 和腔光子数 $N_{\rm ph}$。由于在临界点附近只有激发态 $|k_x=\pm k_{\rm R},k_z=\pm k_{\rm R}\rangle$ 有宏观占据，实验结果和基于 Dicke 模型的理论基本符合。对于有超辐射相变的情形 ($V<0$)，随着驱动光光强从弱极限扫过临界点，腔-BEC 耦合系统从正常相过渡到超辐射相，激发谱的能隙先关闭再打开；相反地，对于 $V>0$ 的区域，由于腔光场趋向于压制原子气体的密度涨落，因而没有超辐射相变，激发谱的能隙随着驱动光的增加而增加。由于探测光的动量为 $k_{\rm R}$，上述测量反映的是系统在 $p=\hbar k_{\rm R}$ 的激发谱，所以这个实验证实了在腔 -BEC 耦合系统中类旋子激发谱的存在。另外，上述结论通过测量原子密度的静态响应率也得到了证实 [42]。

C. 相变临界指数

在腔–原子耦合体系中，原子与腔光场耦合，腔光场与环境相互作用导致腔光场不断耗散到环境，因此环境会间接影响原子气体的动力学演化，最终耦合

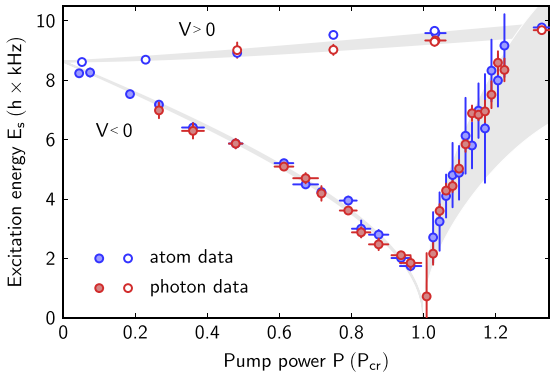

图 6. 腔-BEC 耦合体系的低能激发。这里同时测量了来源于原子的信号（处于激发态 $|k_x = \pm, k_z = \pm\rangle$ 的原子数 N_e，蓝色）和来源于光子的信号（红色）。$V = \hbar\eta_p^2/\tilde{\Delta}_{pc}$ 代表原子感受到的束缚势的振幅。为了与有超辐射相变的情形对比（$V < 0$，实心圆），图中展示了没有超辐射相变情形（$V > 0$，空心圆）。灰色阴影区域代表基于双模模型的理论预测（包含了实验中的不确定性）。其余的参数设置为：原子数 $N = 1.7 \times 10^5$，对于 $V < 0$ 的情形取 $\tilde{\Delta}_{pc} = -2\pi \times (19.8, 23.2)$ MHz，对于 $V > 0$ 的情形取 $\tilde{\Delta}_{pc} = 2\pi \times 15.1$ MHz，驱动光的强度 P 用临界强度 P_{cr} 标度。该图来自参考文献 [42]。

系统达到了动力学稳态。这一动力学稳态与封闭系统的热力学平衡态在各方面都可能存在本质的差别。以前面讨论过的 Dicke 模型为例，对于封闭系统的平衡态，平均场预言正常相在零温时的光场涨落 $\langle\delta\hat{a}^\dagger\delta\hat{a}\rangle_{ebs}$ 为 [41,44]

$$\langle\delta\hat{a}^\dagger\delta\hat{a}\rangle_{ebs} = \frac{\eta^2}{\omega^2\sqrt{1-\left(\frac{\eta}{\eta_{cr}}\right)^2}} \propto |\eta-\eta_{cr}|^{-1/2}, \quad (34)$$

其临界指数是 $-1/2$，与一般的平均场模型一致。而对于动力学稳态，平均场理论结果变为

$$\langle\delta\hat{a}^\dagger\delta\hat{a}\rangle_{dss} = \frac{\eta^2}{2\omega\omega_0\left(1-\left(\frac{\eta}{\eta_{cr}}\right)^2\right)} \propto |\eta-\eta_{cr}|^{-1}, \quad (35)$$

其临界指数是 -1（图 7）。此外，原子算符的涨落（即被激发到 k_R 态的数目）$\langle\delta\hat{b}^\dagger\delta\hat{b}\rangle$ 也具有类似的临界行为 [44]。由此可见，非平衡态稳态将极大地影响量子相变的性质。

2013 年，Esslinger 小组通过实时测量光场的耗散，发现正常相中的腔光场涨落的临界指数在 $-0.9(\pm0.1)$，与平均场理论的预测基本一致 [46]。但是，从图 8 可以发现，基于腔光子单通道耗散的理论预测（黑虚线）明显高于实验所测数据（红色实心圆）。只有人为地把原子激发态的耗散 γ（灰虚点线）也考虑进来，才能使得理论与实验相符（红实线）。同时，开放系统的光子

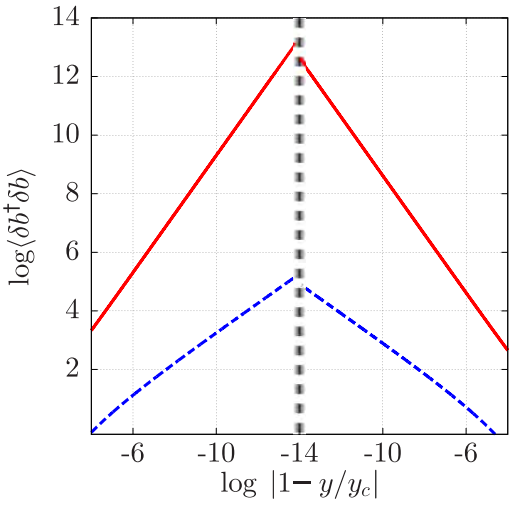

图 7. 开放系统（红色实线）和封闭系统（蓝色虚线）在趋近于临界驱动强度 y_c 时密度涨落的临界行为。开放系统的耗散率 $\kappa = 2\omega_R$，其余的参数为 $\Delta_{pc} = -2\omega_R$，$\xi_c = 0$。该图来自参考文献 [44]。

涨落也明显高于闭合系统的涨落（黑实线）。实际上，实验中不可避免的有限尺寸效应会耦合 BEC 的高能激发态与类旋子激发态，从而使得原子的高能激发态扮演了一个附加的热库，为旋子激发提供了一个新的耗散通道 γ。这一效应必然依赖于驱动光强和体系尺寸的大小，并且会压制由于腔光场导致的密度涨落，从而导致腔光场涨落的减小。有限尺寸效应同时会使得临界点附近的光场涨落添加一个次发散项 $|\eta-\eta_{cr}|^{-3}$，但并不会改变临界指数 [43]。另外，如果考虑非单模的热库，非平衡态的临界行为也会被相应地改变。例如，计算发现 sub-ohmic 热库会通过其低能态密度影响开放系统中的临界指数，使得其绝对值低于 1 [47]。

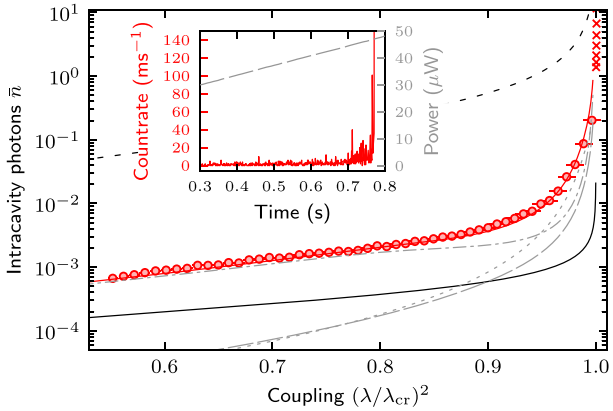

图 8. 发生超辐射之前腔内涨落的光子数。红色圆点是实验结果，黑色实线是闭合系统的理论结果，黑色虚线是基于腔光子单通道耗散的理论预测，红色实线是考虑原子激发态耗散（灰色虚点线）后的结果。该图来自参考文献 [46]。

除了涨落的临界指数以外，弛豫时间、相干长度等物理量的临界指数也能反映相变的类型和性质。在自组织（超辐射）临界点附近，由于旋子的软化，系统的相干长度发散，其弛豫时间变得无穷长，并服从幂律形式

$$\tau \approx |\eta_{\rm p} - \eta_{\rm p}^{\rm cr}|^{-z_\mu \nu_\mu}, \tag{36}$$

式中 $z_\mu\nu_\mu$ 是只依赖于相变类别的普适量（μ 标记驱动相变的方向，即从正常相驱动到自组织相或者反过来）。实验上，从不同方向驱动系统通过临界转变驱动强度 $\eta_{\rm p}^{\rm cr}$，人们发现从均匀相驱动到自组织相的临界指数 $z_1\nu_1 = 0.75$，而从自组织相驱动到均匀相的临界指数 $z_2\nu_2 = 0.18$ [48]。这一结果与 Kibble-Zeruk 机制预测的临界指数 $z_\mu\nu_\mu = 0.5$（包括两个驱动方向）差别较为明显，其中的机制还有待进一步研究。

D. 单分量的玻色–哈伯德模型

在超辐射相变发生后，腔内的光场会形成一个具有周期性的驻波场，原子的运动状态由准动量标记。和传统的光晶格不同的是，腔光场不再是“经典”的保守势，而是会产生反馈效果的势场。这种效应会产生非线性的相互作用，并有可能导致光学双稳现象、甚至更为复杂的三稳现象和一些“燕尾”(swallowtail) 结构。

简单起见，考虑一维单组分玻色气体在单模腔中的运动，且原子被束缚在最低的能带（单带近似），而光腔被原子驱动或者腔驱动。在热力学极限下，如果不考虑原子和腔光场之间的纠缠，所有原子将感受到一个平均的腔光场，此时总哈密顿量简化为

$$\begin{aligned}
\hat{H} &\cong -\Delta_{\rm pc}\hat{a}^\dagger\hat{a} + i\eta_{\rm c}(\hat{a}^\dagger - \hat{a}) + \hat{H}_0 + \hat{H}_1 + \hat{H}_{\rm LM},\\
\hat{H}_0 &= -t_0\sum_{\langle i,j\rangle}(\hat{b}_i^\dagger\hat{b}_j + {\rm H.C.}) + \frac{g_{\rm 1D}}{2}\sum_i \hat{n}_i(\hat{n}_i - 1),\\
\hat{H}_1 &= \xi_{\rm c}\hat{a}^\dagger\hat{a}\big(\hat{D}_s + \hat{B}_s\big),\\
\hat{H}_{\rm LM} &= \eta_{\rm p}\big(\hat{a} + \hat{a}^\dagger\big)\big(\hat{D}_d + \hat{B}_d\big).
\end{aligned} \tag{37}$$

上式中 $\hat{H}_0$ 是背景晶格上的玻色–哈伯德模型（Bose-Hubbard Model, BHM），$\hat{H}_1$ 描述腔光场对光晶格势的影响，$\hat{H}_{\rm LM}$ 描述驱动光与腔光场的干涉，其中在位密度 $\hat{D}_\varepsilon = \sum_i J_{ii}^\varepsilon \hat{n}_i$ 和最近邻格点跃迁 $\hat{B}_\varepsilon = \sum_{\langle i,j\rangle} J_{ij}^\varepsilon(\hat{b}_i^\dagger\hat{b}_j + \hat{b}_j^\dagger\hat{b}_i)$ 分别描述了原子的密度和动能与光场之间的耦合。耦合系数 $J_{ij}^\varepsilon = \int {\rm d}\boldsymbol{r} f_\varepsilon(\boldsymbol{r})\mathbf{w}_i^*(\boldsymbol{r})\mathbf{w}_j(\boldsymbol{r})$，积分内核

$$f_\varepsilon(\boldsymbol{r}) = \begin{cases} u_{\rm c}^*(\boldsymbol{r})u_{\rm c}(\boldsymbol{r}), & \varepsilon = s,\\ u_{\rm p}^*(\boldsymbol{r})u_{\rm c}(\boldsymbol{r}), & \varepsilon = d. \end{cases} \tag{38}$$

如第 IV.A 小节所述，在腔光场的特征频率足够大时，腔光场将跟随原子气体运动，因而可以消去光场，得到原子运动的有效哈密顿量。比如，在原子驱动情形下，物质场和光场之间的干涉项 $\hat{H}_{\rm LM}$ 写为

$$\hat{H}_{\rm LM} = \eta_{\rm p}^{\rm eff}\big(\hat{D}^\dagger + \hat{B}^\dagger\big)\big(\hat{D} + \hat{B}\big). \tag{39}$$

式中 $\eta_{\rm p}^{\rm eff} = 2\tilde{\Delta}_{\rm pc}\eta_{\rm p}^2/(\tilde{\Delta}_{\rm pc}^2 + \kappa^2)$ 刻画了原子之间被腔光场诱导出的有效长程相互作用的强度，可以通过激光驱动强度 $\eta_{\rm p}$ 和激光失谐 $\Delta_{\rm pc}$ 等调节。

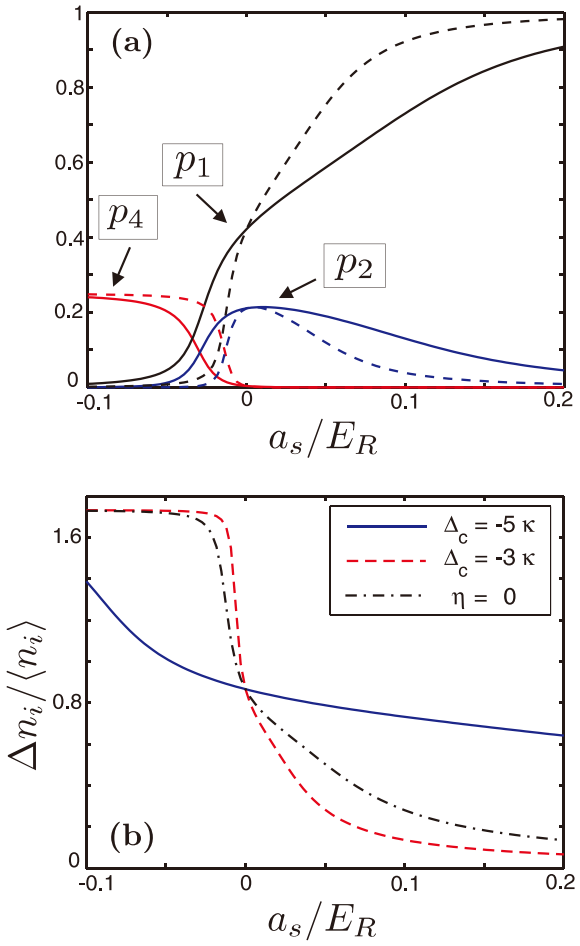

图 9. （a）单个格点上有 n 个粒子占据的概率 p_n 和（b）粒子数涨落随散射长度 $a_{\rm s}$ 的变化。图（a）中实线是原子气体位于光腔产生的光晶格中的情况，虚线是没有腔但有相同深度的经典光晶格 $V_{\rm eff}$ 的情况。此外，$\xi_{\rm c} = -\kappa$，$\Delta_{\rm pc} = -3.75\kappa$，$V_{\rm eff} = -4E_{\rm R}$。图（b）中虚点线对应于经典光晶格情况，其余的线对应不同的失谐。该图来自参考文献 [49]。

除了为原子提供一个平均的周期势之外，腔光场

的量子涨落也会影响原子气体的状态。一方面，对于原子和腔耦合较弱或者腔光子很少的情况，较大的腔光场涨落会使得系统的基态表现出较为复杂的行为 [49]。比如，当腔光子数 $n_{\rm ph}=0$ 时（没有外加束缚势和较弱的接触相互作用），腔光场不影响原子气体的长程关联；但是当 $n_{\rm ph}=1$ 时，此时的腔光场趋向于阻止原子在空间的移动，破坏原子气体的长程关联，因而原子的基态往往是不同物质相的叠加态（图 9(a)）。腔光场的涨落还会增加 Feshbach 共振 BEC 区域的粒子数涨落，同时压制 BCS 区域的粒子数涨落（图 9(b)）。另一方面，如果外加较深的背景光晶格使得原子的跃迁矩阵元 $(J_{ij}^{\rm s})$ 只是微弱的依赖于腔光场（腔光场涨落相对较小），由腔光场诱导的相邻格点的跃迁仍然会改变原子系综的稳态，这一点在腔驱动和原子驱动的情形均可以看到。

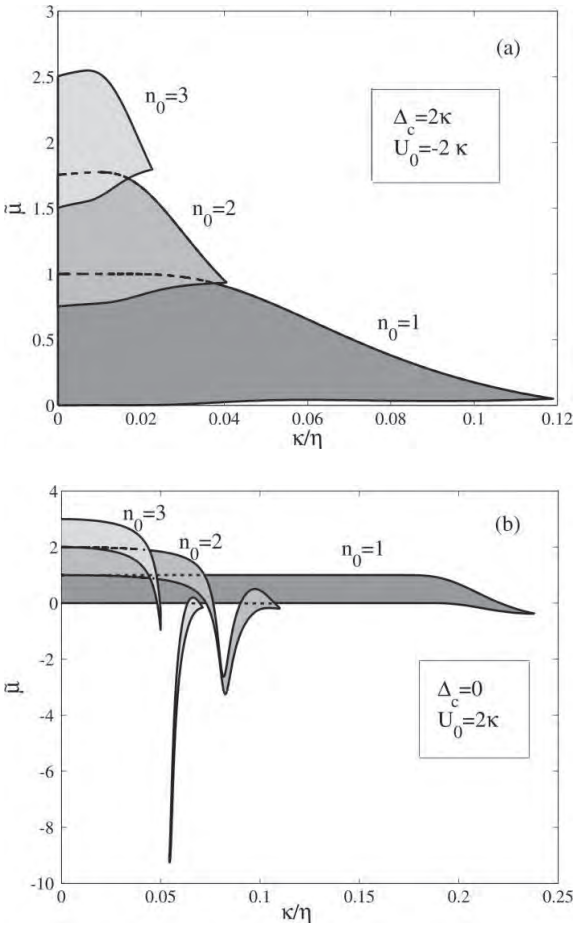

图 10. 腔驱动情况下玻色–哈伯德模型的相图。横轴为耗散率和驱动光强的比值 κ/η，纵轴为重整后的化学势 $\tilde{\mu}/g_{\rm 1D}$。该图来自参考文献 [50]。

比如在腔驱动的情况下，由于腔的非线性效应和相互作用对粒子数密度的影响，莫特绝缘态会出现许多亚稳态 [50,51]，系统在不同失谐下的相图也会表现出较大的差异（图 10）。当 $\Delta_{\rm pa}<0$ 时，原子趋向于聚集在波腹上，使得原子和腔的耦合极大，这时腔的非线性效应最为显著；而如果 $\Delta_{\rm pa}>0$，原子聚集在波节，使得原子和腔的耦合极小。因而在强驱动极限下，相图和标准的玻色–哈伯德模型一致。但是当驱动光较弱时，相图中出现了许多双稳态区域，甚至有些莫特绝缘态还出现在了化学势为负的区域。

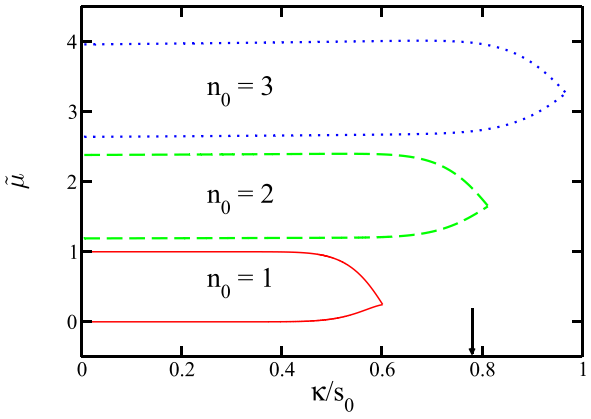

图 11. 原子驱动情况下玻色–哈伯德模型的相图。横轴为耗散率与驱动光强的比值，纵轴是重整后的化学势（相对于每个格点上仅有一个粒子时的在位相互作用特征能量 U_1）。黑色箭头代表密度 $n_0=1$ 时发生超辐射相变的位置。其他参数为 $\Delta_{\rm pc}=-50\,\kappa$，$\xi_{\rm c}=-0.1\,\kappa$，$g_{\rm 1D}/E_{\rm R}\lambda=4.74\times10^{-4}$。该图来自参考文献 [58]。

在原子驱动的情况下，由于原子的在位相互作用能依赖于腔光场的大小。腔光场越大，在位相互作用能越大。这不仅使得超流到莫特绝缘体转变的临界驱动光强变大，也使得莫特绝缘体的各区域 (lobes) 之间出现间隙（图 11）。在弱驱动极限 $s_0\to0$ 或者坏腔极限 $\kappa\to\infty$ $(\kappa/s_0\to\infty)$ 下，系统进入均匀的超流相（平均光子数为零）。随着驱动光的增强或者腔的耗散下降，系统将进入超辐射相，使得原子在空间形成周期为 λ 的莫特绝缘体。在超流和绝缘体之间，原子系综可能既具有超流的非对角长程序也具有电荷密度波的对角长程序。比如在填充数 $n_0=1$ 且 $0.6<\kappa/s_0<0.78$ 时，原子气体既有固体的周期性又有超流的相干性，因而又称这种状态为超固相 (supersolid)。对超固相的寻找和研究是凝聚态物理的重要课题之一 [28,52–57]。以往的研究大多聚焦具有长程相互作用的体系，比如具有偶极相互作用的 BEC [54]。在腔-BEC 耦合系统中，由于原子和同一个模式下的腔光场相互作用，使得原子之间具有等效的长程相互作用，因而在某些参

数区间可能出现超固相。

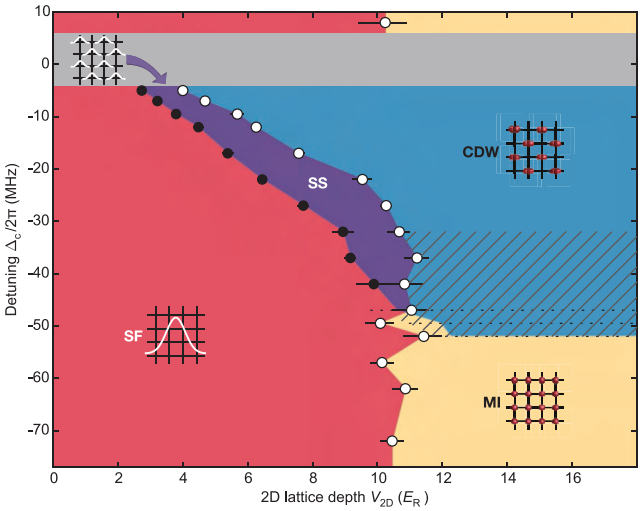

图 12. 在失谐 Δ_{pc}（即图中 Δ_c）和晶格深度 V_{2D} 平面的相图。相图中包括超流相 SF（红色）、超固体相 SS （紫色）、电荷密度波相 CDW（蓝色）和莫特绝缘体相（黄色）。黑色实心点代表电荷密度波的建立，白色空心点代表超流性的消失，斜线区域代表 CDW 和 MI 的共存区域。图中填充数 $n_0 \approx 1$。该图来自参考文献 [57]。

在 2016 年的实验中 [57]，Esslinger 小组将由约 4.2×10^4 个 ^{87}Rb 原子组成的 BEC（温度为 42 nK）传送到一个光腔中，通过沿腔轴和垂直于腔轴两个方向加一个经典光晶格，同时在另一个正交的方向加一束强光把原子气体切成二维气体。由于驱动光与腔的失谐 $|\Delta_{pc}|/2\pi \sim 10$ MHz 远大于腔的耗散频率 $\kappa/2\pi \sim 1$ MHz，而后者又远大于原子运动的特征频率 $\omega_R/2\pi \sim 1$ KHz，因此可以安全地绝热消除光子自由度，得到腔中扩展的玻色–哈伯德模型

$$\hat{H} = -t_0 \sum_{\langle e,o\rangle} (\hat{b}_e^\dagger \hat{b}_o + \text{H.C.}) + \frac{U_s}{2} \sum_{i\in e,o} \hat{n}_i(\hat{n}_i - 1), \\ + \frac{U_l}{K}\Big(\sum_e \hat{n}_e - \sum_o \hat{n}_o\Big)^2 - \sum_{i\in e,o} (\mu - V_i)\hat{n}_i, \quad (40)$$

上述哈密顿量的前两项代表传统的玻色–哈伯德模型，而第三项代表由腔光子诱导的原子之间的长程相互作用，其系数 $U_l = K\hbar|\eta M_0|^2\tilde{\Delta}_{pc}/(\tilde{\Delta}_{pc}^2 + \kappa^2) \propto V_{2D}/\tilde{\Delta}_{pc}$，$V_{2D}$ 为背景光晶格深度。另外，$\tilde{\Delta}_{pc} = \Delta_{pc} - \delta_c$，$M_0$ 代表原子和光场之间的重叠程度，δ_c 代表原子气体对腔的频率移动。这个体系中的电荷密度波序可以用奇偶格点的粒子数失衡 $\Theta = |\sum_e n_e - \sum_o n_o|/|\sum_e n_e + \sum_o n_o|$ 表征。当 $\tilde{\Delta}_{pc} > 0$ 时，长程相互作用会使得原子之间的能量升高，因而此时只有超流相或者莫特绝缘体相。当 $\tilde{\Delta}_{pc} < 0$ 时，$U_l < 0$，这时系统将有可能具有电荷密度波序（$\Theta \neq 0$）。

该实验通过测量光子数反推 Θ（图 12 黑实心点），并通过时间飞行 (time-of-flight) 测量原子气体的空间相干性（图 12 白空心点）。一方面，当失谐 $|\Delta_{pc}|$ 较小时，较浅的晶格使得气体被原子的动能所主导，因而表现为空间均匀的超流态（红色，SF）。而较深的晶格则会压制原子的动能，但是由于腔光场较强使得电荷密度波序得以建立。在这两者之间，气体既有超流特性又有电荷密度波序，此时被称为超固相（紫色，SS）。另一方面，随着失谐 $|\tilde{\Delta}_{pc}|$ 的增加，腔光场也随之减小，因而在较深的晶格下，原子气体表现为莫特绝缘体（黄色，MI）。值得注意的是，腔光场和经典光晶格的竞争有可能导致双稳态，如图 12 中的斜线区域。在理论上，人们对该体系中的超固相进行了一系列的研究。平均场理论给出的相图和实验结果定性吻合 [59−62]。注意到由于前述实验是通过调节背景光晶格深度 V_{2D} 的方式调节在位相互作用 U_s，在调节的同时也改变了长程相互作用，因此并不能独立解析出在位相互作用 U_s 的影响。此外，动力学平均场方法（Dynamical Mean Field Theory, DMFT）也确认了二维系统中超固相的存在 [63,64]。同时由于在位相互作用趋向于使得原子气体均匀分布，因而会提高发生超辐射相变的临界值 [63]。随后的进一步研究指出，动力学平均场方法在定量上仍然不精确 [65]。值得一提的是，当腔光场足够强时，将不仅与原子的密度耦合，而且还与原子的动能耦合，这使得原子体系形成了一些新奇的物相 [59]。

另一方面，当腔的耗散率 κ 与原子的动能 ω_R 相当时，腔光子不再绝热地跟随原子运动，导致绝热近似失效。此时腔光子不仅会诱导原子之间的全局相互作用，还会有其他的动力学效应。虽然如此，腔-BEC 耦合系统仍然可以达到动力学稳态 [48,65]。当驱动光和腔的有效失谐 $\tilde{\Delta}_{pc} < 0$ 时，腔光场放大原子气体的密度涨落，因而仍然会发生超辐射相变。当腔光场超过一定临界值时，原子体系的空间相干性将会消失，成为莫特绝缘体，如图 13 所示。在这个实验中，原子的有效失谐 $|\tilde{\Delta}_{pc}|$ 与腔的耗散速率 κ 在相同量级，填充数 $n_0 \approx 20$。图中 HSF 代表仅有空间相干性的均匀超流相，SSF 代表同时具有电荷密度波序和空间相干性的超固相，而 SMI 代表仅有电荷密度波序的自组织莫特相。由于腔和原子运动的特征时间相当，人们在实验中也观察到了可能由动力学效应导致的 “磁滞效

应” [48]。

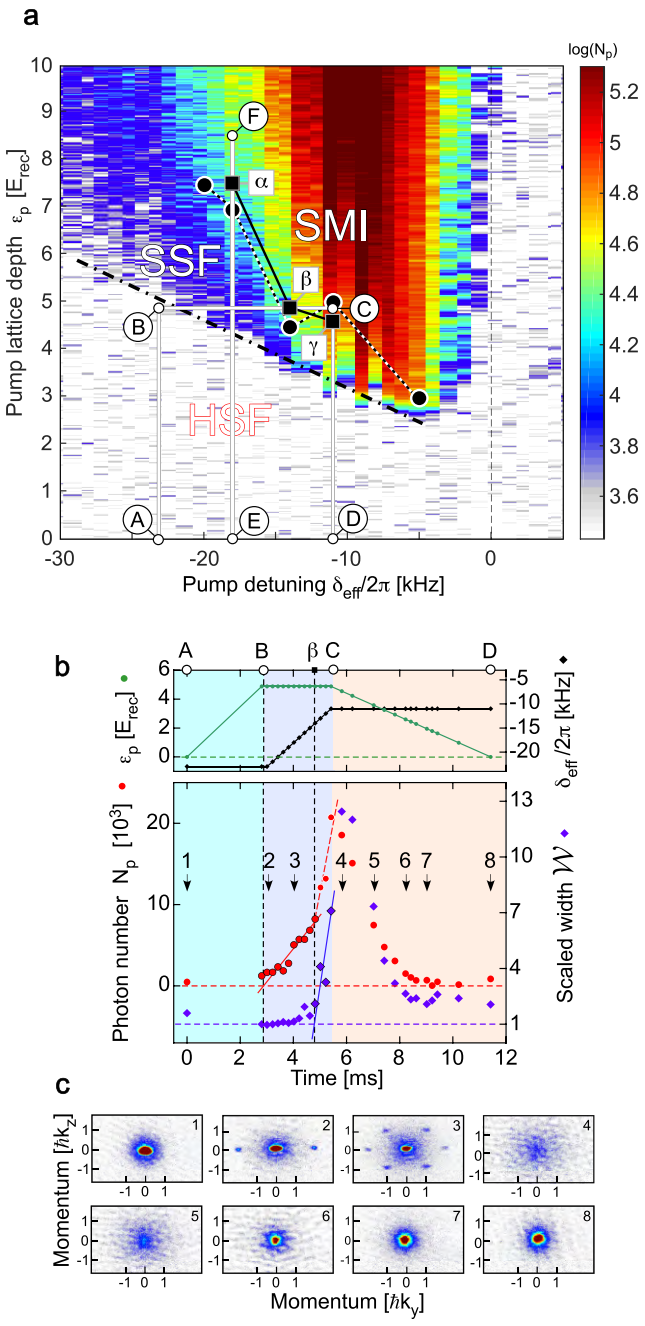

图 13. (a) 腔光子数 $N_{\rm p}$ 随有效失谐 $\tilde{\Delta}_{\rm pc}$（即图中 $\delta_{\rm eff}$）和驱动光强度（图中 $\epsilon_{\rm p}$）的变化趋势。图中 HSF 代表均匀超流相，SSF 代表超固体相，SMI 代表莫特相。(b) 沿图 (a) 中的路径 $ABCD$，光子数和动量分布半高宽 W 的变化趋势。在 $B-C$ 之间，腔光子数有限而原子仍然具有空间相干性，体系处于 SSF 相。(c) 沿 $ABCD$ 路径，体系经过图(b) 中由箭头标记的位置 1-8 时，原子在 k_y-k_z 平面内的动量分布。该图来自参考文献 [65]。

E. 自旋–轨道耦合的玻色气体

自旋–轨道耦合效应往往会强烈地改变单粒子的色散关系和自旋成分，从而极大地影响体系的性质，出现新奇的基态物相和低能激发 [66,67]。在冷原子物理中，现有的实验一般通过微波或者拉曼过程耦合原子不同超精细能级形成人工自旋–轨道耦合。当把原子气体置于光腔中时，腔光场和原子气体的相互影响使得腔–原子耦合系统往往表现出一些非线性效应。最简单的实现人造自旋-轨道耦合的方案是通过微波直接耦合原子不同超精细能级，使得不同分量的原子相干并伴随动量转移。即使在这样简单的构形里，光腔也会使得系统表现出一些不同于传统的光力系统的性质。腔–原子耦合系统在某些参数区间内甚至表现出三稳现象 — 存在两个亚稳态和一个基态 [68]。在拉曼过程产生的自旋–轨道耦合系统中，原子的两个基态与一个高能激发态通过两束拉曼光耦合。当两束拉曼光的单光子失谐远远大于激发态的线宽时，激发态的占据可以忽略不计，此时原子的两个基态发生相干形成自旋–轨道耦合。如果其中一束拉曼光借助于腔光场实现，则腔的非线性和耗散效应也将通过拉曼过程进入到系统，使得系统出现燕尾结构 (swallowtail) [69] 等非线性效应 [70−73]。

例如，可以沿垂直于腔轴的方向使用两束大失谐（相对于原子跃迁频率红失谐，$\Delta_{\rm pa}<0$）的平面波（探测光，拉比频率 Ω_2）和驻波（驱动光，拉比频率 Ω_1）驱动原子，同时选择恰当的驱动光偏振方向使得它们耦合原子的不同基态能级，通过压制 σ^- 光使得腔光场同时能耦合驱动光所耦合的能级（拉比频率 g_0），这时原子将通过两种拉曼过程耦合起来，即 $\Omega_2-\Omega_1$ 和 Ω_2-g_0。描述该系统的有效哈密顿量为 [74]

$$h=\begin{bmatrix} -\delta/2 & \hat{M}_-(x,y) \\ \hat{M}_-^\dagger(x,y) & \delta/2+\hat{M}_z(x,y) \end{bmatrix}. \tag{41}$$

其中 δ 是有效的双光子失谐，$\hat{M}_z(x,y)=U_1\cos^2(ky)+U_0\hat{a}^\dagger\hat{a}\cos^2(kx)+\eta(\hat{a}^\dagger+\hat{a})\cos(kx)\cos(ky)$ 代表赝自旋朝下的粒子感受到的由驱动光和腔光场产生的晶格势。在一般的实验中，驱动光的拉比频率 Ω_1 比腔的拉比频率 g_0 大很多，比如 $\Omega_1/g_0=10$，因而影响主要来源于驱动光的晶格势 (U_1) 和驱动光与腔光场之间的散射 η。此外，$\hat{M}_-(x,y)=[-\Omega\cos(ky)+\Omega_{\rm c}\hat{a}\cos(kx)]e^{-iky}$ 描述两种拉曼过程产生的自旋–轨道耦合效应，其中 $\Omega=-\Omega_1\Omega_2/\Delta_{\rm pc}$，$\Omega_{\rm c}=g_0\Omega_2/\Delta_{\rm pc}$。这时的腔光场振幅 $\alpha=\langle\hat{a}\rangle=(\eta\Theta+\Omega_{\rm c}\Xi)/(-U_0B+i\kappa)$，其中 $B=$

$\langle\Psi_\downarrow|\cos^2(kx)|\Psi_\downarrow\rangle$，$\Theta = \langle\Psi_\downarrow|\cos(kx)\cos(ky)|\Psi_\downarrow\rangle$ 和 $\Xi = \langle\Psi_\downarrow|\cos(kx)\exp(iky)|\Psi_\uparrow\rangle$ 分别衡量了自旋朝下的粒子对腔频率的移动、对驱动光的散射能力以及拉曼过程对探测光的散射能力。

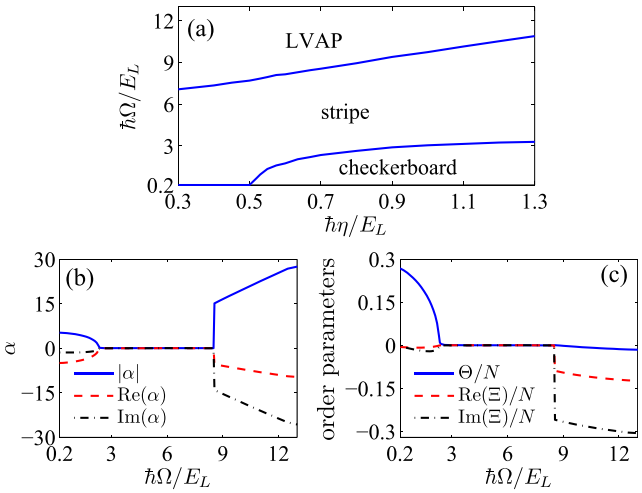

图 14. (a) 具有腔诱导的自旋–轨道耦合的两分量玻色气体的相图。图中 Ω 是探测光驱动的自旋–轨道耦合强度，η 是驱动光强度。固定驱动光强度 $\eta = 0.7EL/\hbar$ 时，腔光场的期望值 α 和原子体系序参量 Θ 随自旋–轨道耦合强度 Ω 的变化趋势如 (b) 和 (c) 所示。图中其他参数为：双光子拉曼失谐 $\delta = -4E_{\rm L}/\hbar$，驱动光与腔光场的单光子拉比频率比 $\Omega_1/g_0 = 10$。该图来自参考文献 [74]。

如图 14(a) 所示，在 $\Omega_1 \gg g_0$ 的条件下，随着探测光 Ω_2 的变化，该系统在零温可以出现三个截然不同的物相：棋盘相（超辐射）、条纹相（正常态）和涡旋-反涡旋晶格相（超辐射）。首先，当探测光 Ω_2 较小时，只有自旋朝下的粒子散射驱动光 ($\Theta \neq 0$)，而自旋朝上的粒子不散射光子 ($\Xi \approx 0$)。因此只有驱动光的强度超过临界值时，腔光场才会有宏观占据 ($\alpha = \langle\hat{a}\rangle \neq 0$)，此时自旋朝下的粒子形成棋盘结构。由于不可避免的背景散射会使得自旋朝上与自旋朝下的粒子之间存在相互作用，自旋朝上的粒子的空间分布也会受到影响，具体形式依赖于散射长度。以铬原子 (Chromium，Cr)为例，由于不同赝自旋之间的散射长度为 $a_{\uparrow\uparrow} = a_{\uparrow\downarrow} = 112a_{\rm B}$ 和 $a_{\downarrow\downarrow} = 87.5a_{\rm B}$（$a_{\rm B}$ 是玻尔半径）满足不相容 (immiscible) 条件 $a_{\uparrow\downarrow}^2 > a_{\uparrow\uparrow}a_{\downarrow\downarrow}$，因此自旋朝上的粒子将聚集在自旋朝下粒子密度最小的地方。其次，当逐渐增加探测光的强度 Ω_2 时，由 $\Omega_2 - \Omega_1$ 组成的拉曼过程形成自旋–轨道耦合。这种自旋–轨道耦合效应等价于一个空间位置依赖的有效磁场 $\boldsymbol{B} = (B_x, B_y) \approx -\Omega\cos(ky)(\cos(ky), \sin(ky))$，其周期为 π/k。这个有效磁场将压制腔光场的形成（后者的周期为 $2\pi/k$），因而随着 Ω (Ω_2) 的增强，腔光场将逐渐消失，最终进入一个由 $\Omega_1 - \Omega_2$ 主导的物质相——条纹相。这时垂直于腔轴方向原子形成条纹状的分布 ($\alpha = 0$)，见图 14(b)。最后，当进一步增强 Ω 时，通过 $\Omega_2 - g_0$ 散射光子的拉曼过程也开始显现作用，此时的腔光场主要来源于通过拉曼过程散射的探测光，即 $\Theta \approx 0$ 和 $\Xi \neq 0$（图 14(c)）。这时由于拉曼过程起主导作用，两种组分的原子将在空间形成相同的分布 (miscible)。注意到该体系中的拉曼过程相当于引入了有效磁场，一方面使得原子的自旋形成磁性结构，另一方面使得原子波函数的相位形成涡旋–反涡旋晶格阵列（周期 $2\pi/k$）。这一等效磁场的强度可以达到几个特斯拉量级，这使得腔–原子气体耦合系统成为研究量子霍尔效应的一个新平台。

V. 光学腔中的超冷费米气体

如前所述，当温度足够高时，遵从麦克斯韦–玻尔兹曼统计的热原子气体会在足够强的横向驱动下出现超辐射（自组织）相变 [33,34]。但是，随着温度的逐渐降低，不同的量子统计性质使得耦合系统表现出截然不同的性质。对于玻色子，当温度足够低的时候，几乎所有的原子都会凝聚到能量最低态，这使得超辐射相变更容易发生。对于费米子而言，其在低温下是否仍然能够发生超辐射相变？相变的发生条件和特征是否会出现变化？近期的研究发现，一方面，对于单分量 (spinless) 费米气体，泡利不相容原理并没有禁戒超辐射相变，相反在某些参数区间，超辐射的不稳定性会被极大地增强，而维度和光腔的耗散也会产生显著的影响；另一方面，当原子的自旋自由度参与到系统的动力学演化，该复合体系的性质会变得更为特殊和有趣，出现非平衡态的腔诱导配对 [75]、人造规范势 [76–78] 等新奇物理现象。

A. 单分量费米气体

将简并的单分量费米气体置于驻波光腔中，同时沿横向驱动原子气体。描述其运动的哈密顿量与玻色气体具有相同的形式（见 (17) 式）。由于费米统计，原子算符遵循反对易关系 $\{\hat{\Psi}(\boldsymbol{r}), \hat{\Psi}^\dagger(\boldsymbol{r}')\} = \delta(\boldsymbol{r} - \boldsymbol{r}')$，同时原子之间的接触相互作用被泡利不相容原理所禁戒，即 $U_{\rm s} = 0$。在热力学极限下，光场的涨落可以忽略不计，我们采用平均场的方式处理腔光场 $\langle\hat{a}\rangle = \alpha$。在红

失谐的驱动光情形下，光场的涨落仍然会扩大原子气体的密度涨落，但是由于泡利不相容原理，使得原子气体的超辐射相变受到气体密度和维度的影响。理论研究发现 [79]，腔光场的建立一方面会加深沿腔轴的晶格深度 $\xi_{\rm c}|\alpha|^2\cos^2(k_{\rm R}x)$，另一方面会散射近共振的驱动光（$\omega_{\rm p}\approx\omega_{\rm c}$）进入光腔 $\eta_{\rm p}(\alpha+\alpha^*)\cos(k_{\rm R}x)$，而沿驱动光的晶格深度也会受驱动光的影响。通过二阶微扰论可得临界驱动强度

$$\eta_{\rm p}^{\rm cr}\sqrt{N}=\frac{1}{2}\sqrt{\frac{\tilde{\Delta}_{\rm pc}^2+\kappa^2}{-\tilde{\Delta}_{\rm pc}}\frac{E_{\rm R}}{f}},\tag{42}$$

这里的参数定义与玻色气体的情形保持一致。式中 f 是一个与统计特性、驱动强度、原子气体密度和维度有关的量。

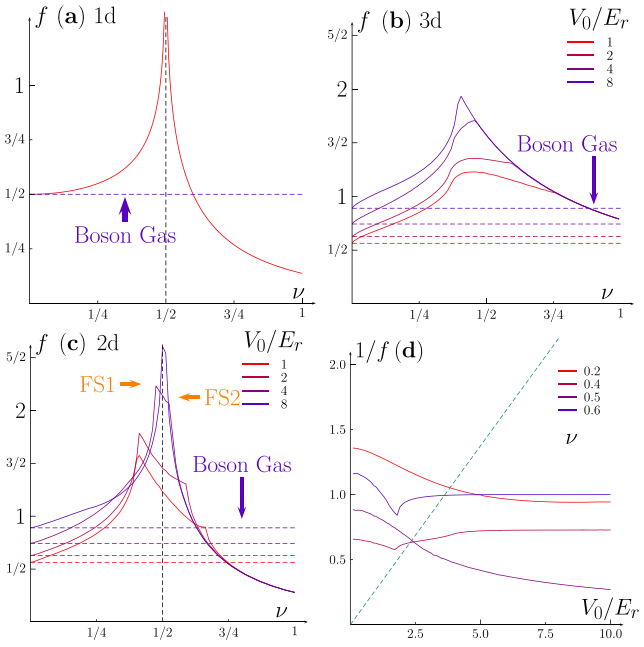

图 15. (a) 一维、(b) 三维、(c) 二维单分量费米气体发生超辐射相变的临界参数 f 随填充数 ν 的变化。参数 f 和临界驱动强度的关系如公式（42）所示。图中 V_0 为驱动光的强度，虚线代表同样参数下玻色气体的情况。(d) 不同填充数下参数 $1/f$ 随 V_0 的变化趋势。图中虚线和实线的交点代表相应情况下的超辐射相变点。该图来自参考文献 [79]。

图 15 展示了不同维度下 f 随原子填充数 ν（气体密度）的变化关系 [79]。对于玻色气体而言，由于粒子可以占据同一个格点，因此其临界强度不受气体密度和维度的影响（图中虚线）。但是对于费米气体而言，由于统计性质的影响，费米子能够获得的相空间受到气体密度和维度的强烈影响（实线）。在低密度时（$\nu\to 0$），费米气体比玻色气体更容易发生超辐射相变。在高密度时，泡利不相容原理则会压制超辐射相

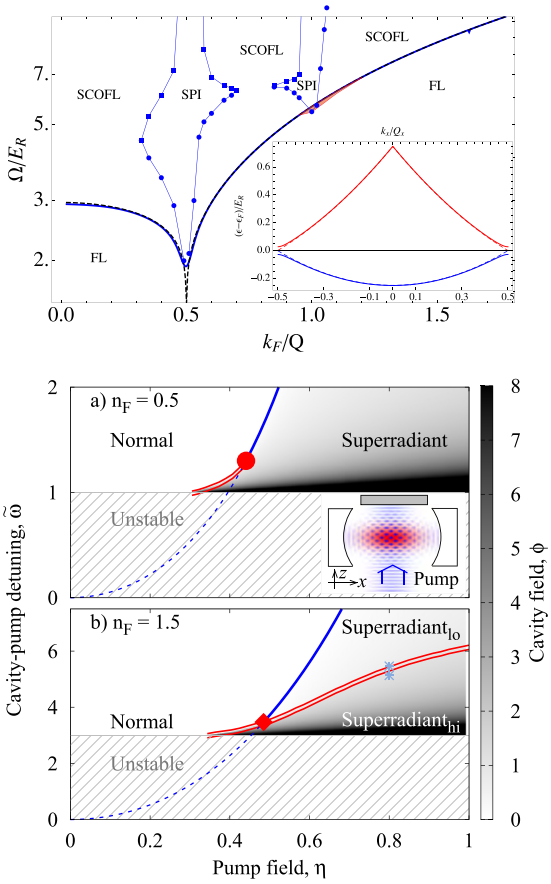

图 16. 上图：一维单分量费米气体的相图。主图由蓝色实线区分三个物相（温度 $k_{\rm B}T/E_{\rm r}=0.01$）：费米液体 (Fermi Liquid，FL)、超辐射 Peierls 绝缘体 (Superradiant Peierls Insulator，SPI) 、超辐射电荷有序费米液体 (Superradiant Charge Ordered Fermi Liquid，SCOFL)。黑色虚线代表温度 $k_{\rm B}T/E_{\rm r}=0$。插图代表超辐射相变在费米面附近从无能隙（虚线）变为有能隙（实线）。该图来自参考文献 [80]。下图：二维单分量费米气体的相图。图中 (a) 和 (b) 分别代表填充数 $n_{\rm F}=0.5$ 和 1.5 的情况，蓝色实线代表二阶相变，红色双线代表一阶相变，斜线区域代表不稳定区域。该图来自参考文献 [81]。

变 [79–81]。特别地，当费米面和腔光场的波矢发生嵌套 (nesting) 时，超辐射相变被极大地增强。这一机制与固体中的 Pierels 相变类似。由于一维费米气体的费米面是两个离散点，当填充数 $\nu=0.5$ 费米面发生嵌套时，效果最为显著，导致临界驱动强度 $\eta_{\rm p}^{\rm cr}\to 0$，如图 15(a) 和图 16（上）所示。此时，任意有限的腔光场都可以在费米面打开能隙，使得原子气体表现为绝缘体（图 16（上）的 SPI 区域）。当填充数远离半满时，有限的腔光场并不能在费米面附近打开能隙，因而原子气体表现为金属（图 16（上）的 SCOFL 区域）。与玻色体系类似，超辐射相变既可以是连续相变也可以是一阶相变（图 16）。在二维和三维体系中，由于费米

面不能完全匹配，嵌套效果虽然会增强超辐射，但临界驱动强度不能达到零，如图 15(b) 和 (c) 所示。当填充数占据到更高能带时，费米面的复杂结构将会带来更为丰富的现象。特别地，当沿腔轴方向的晶格深度超过驱动方向的晶格深度时，原子将趋向于更多地沿腔轴排列，从而增强超辐射。这时将发生一个腔光场较小到较大的一阶相变，如图 16 （下）图所示。这两个相通过不同的密度绝热地联系起来，类似于气液相变。

有限大小的耗散或者温度都会抑制腔光场的建立，但是上述诸多现象在实验范围内仍然可以被探测，比如借助于时间飞行测量或者光腔的漏光光谱 [80]。值得注意的是，费米气体虽然具有不同于玻色气体的特性，但是在高密度极限下，费米气体的超辐射相变与玻色气体的相变类似。在临界点附近，仍然可以等价为 Dicke 模型 [82]。

B. 两分量简并费米气体

随着自旋自由度的引入，光腔中两分量费米气体会表现出更为丰富的物理。首先，由于不同分量原子之间的 s 波散射长度可以通过 Feshbach 共振技术进行调控，原子之间的相互作用可以从弱吸引相互作用经过幺正区域连续调节到弱的排斥相互作用，使得体系发生 BCS-BEC 过渡。在 BCS 区域 ($a_s<0$)，低能激发服从费米统计，其超辐射相变主要表现为费米体系的特征，比如临界驱动强度的密度依赖；在 BEC 区域 ($a_s>0$)，两个不同分量的费米子形成复合玻色子，低能激发服从玻色统计，其超辐射相变主要体现出玻色体系的特征，其临界驱动强度基本与密度无关。在幺正区域 ($1/k_{\rm F}a_s\to\pm0$)，低能激发则会同时表现出两种统计特性。因此，在 BCS-BEC 过渡中，超辐射相变临界驱动强度强烈地依赖于原子间相互作用和原子密度 [83]。

此外，在不同分量费米子之间也可以实现人造规范势和人造自旋-轨道耦合。具有自旋-轨道耦合的费米系统会产生极为丰富的物理现象，比如自旋霍尔效应 [84]、拓扑绝缘体 [85]、Majorana 费米子 [86]、Weyl 半金属 [87] 等。在势阱和光晶格中的超冷费米气体中，目前已经实现了多种类型的自旋–轨道耦合 [88−90]，在理论上对其中的配对物理和拓扑性质也进行了深入的研究 [91,92]。在光学腔中，腔光场和自旋–轨道耦合的相互叠加使得原子气体展现出了和自由空间不同的性质和现象，如拓扑超辐射和拓扑超流等 [77]。同时，腔光场的耗散通道也使得人们可以非破坏地研究多体体系的动力学行为和非平衡态相变。

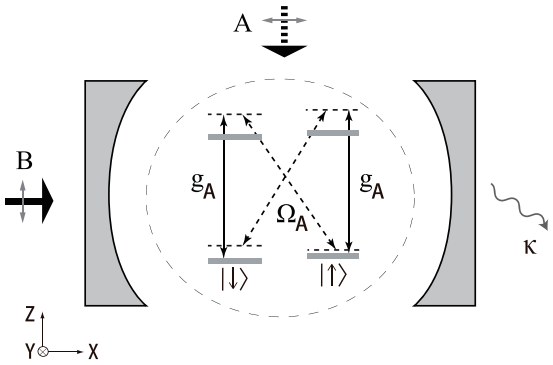

图 17. 利用 FP 腔在两分量费米气体中实现人造自旋–轨道耦合的方案。本方案中垂直于腔轴方向加一束驱动光 $\omega_{\rm A}$ 驱动 A 模式，两分量的超冷原子只能沿腔轴运动，同时沿腔轴方向加一束大失谐的线偏振光驱动腔的另一支模 B。该图来自参考文献 [93]。

考虑将处于量子简并温度以下的费米气体（比如 ^{6}Li）装载到 FP 腔中，沿垂直于腔轴方向驱动原子（偏振方向沿腔轴），超辐射相变将使得光腔的一支振动模式被激发（模式 A）。同时，光腔的另一个模式 (B) 被大失谐的线偏振光驱动，如图 17 所示。为了使更多光子被散射到光腔中，纵向驱动光和腔光场的 A 模近共振，且相对于原子的激发态是大的蓝失谐。这时激发态的占据数很小，可以被绝热消除。为了简单起见，假设垂直于腔轴的两个方向都存在强的束缚势，约束强度 $\hbar\omega_\perp$ 远大于原子气体的费米能 E_F。这时，费米气体等效为沿腔轴方向的准一维费米气体，其等效哈密顿量为 [77]

$$\begin{aligned}\hat{H}_0=&-\Delta_{\rm pc}\hat{a}^\dagger\hat{a}+\sum_\sigma\int{\rm d}x\hat{\Psi}^\dagger_\sigma(x)\left[\frac{-\hbar^2\partial_x^2}{2m}\right.\\&\left.+(V_0+\xi_A\hat{a}^\dagger\hat{a})\cos^2(k_0x)+\xi_\sigma m_z\right]\hat{\Psi}_\sigma(x)\\&+\eta_A(\hat{a}^\dagger+\hat{a})\left[\int{\rm d}x\hat{\Psi}^\dagger_\uparrow(x)\cos(k_0x)\hat{\Psi}_\downarrow(x)+{\rm H.C.}\right].\end{aligned}\tag{43}$$

式中 $\hat{a}$ 和 $\hat{\Psi}_\sigma(x)$ 分别是腔模 A 和原子场的场算符，$\Delta_{\rm pc}=\omega_{\rm p}-\omega_{\rm A}$ 为驱动光相对于腔模 A 的失谐，V_0 腔模 B 提供的背景光晶格，$\xi_{\rm A}=g_{\rm A}^2/\Delta_{\rm pa}$ 为单个原子对腔模 A 的频率移动，$\eta_{\rm A}=sg_{\rm A}\Omega_{\rm A}/\Delta_{\rm pa}$ 是有效拉比频率，m_z 为沿 z 方向的磁场。这里 $s=\exp(-k_0^2\rho^2/8)$，$\Delta_{\rm pa}=\omega_{\rm p}-\omega_{\rm eg}>0$)，$\xi_\sigma=\pm1$。如果腔光场不为零，哈密顿量（43）式的第三项描述了由腔光场诱导的自旋–轨道耦合。

对腔光场应用平均场近似 $\langle\hat{a}\rangle=\alpha$，当腔光场的动力学特征频率远大于原子的反冲能量 $E_{\rm r}=\hbar^2k_0^2/2m$ 时，费米气体和腔光场最终达到如下稳态

$$\alpha=\frac{\eta_A\int \mathrm{d}x\cos(k_0x)\left[\langle\hat{\psi}_\downarrow^\dagger\hat{\psi}_\uparrow\rangle+\mathrm{H.C.}\right]}{\Delta_{\rm pc}+i\kappa-\xi_A\sum_\sigma\int \mathrm{d}x\langle\hat{\psi}_\sigma^\dagger\hat{\psi}_\sigma\rangle\cos^2(k_0x)}. \quad (44)$$

当没有驱动光时，磁场会把系统分为正常费米气体 ($m_z<m_{\rm c}$) 和完全极化费米气体 ($m_z>m_{\rm c}$)。当驱动光足够强时，通过拉曼过程原子将散射足够多的光子进入腔并与耗散过程达到平衡，这时发生超辐射相变 $\alpha\neq0$。更为重要的是，拉曼过程将引起不同能带间的自旋翻转过程，使得基于瓦尼尔 (Wannier) 表象的单带近似不再适用。当磁场较小时 ($m_z<m_{\rm c}$)，驱动光诱导的有限腔光场将在费米面附近打开能隙的同时翻转原子的自旋，系统进入了一个拓扑超辐射态。这个非平庸拓扑态的拓扑性质可以由第一布里渊区内自旋结构的非零环绕 (Winding) 数刻画（如图 18 所示），同时会伴随一对零模边缘态 (edge state) 的产生。当磁场大于临界磁场时 ($m_z>m_{\rm c}$)，计算表明存在两种不同的超辐射相：一种是拓扑平庸超辐射相，而另一种相与弱磁场极限的拓扑非平庸相一致。这里的拓扑非平庸态来源于特殊的拉曼构形：腔光场所形成的拉曼光晶格的周期是背景晶格周期的两倍，它们在波节处相交，因而使得拉曼场耦合同格点上的 s 和 p 能带，同时带间的耦合强度反比于能级差，所以不同分量对应的耦合强度不同。这种特性使得系统的能隙随着驱动光强度 $\eta_{\rm A}$（或者腔光场 α）的增强经历了先闭合再逐渐打开的过程。通过对角化哈密顿量（43）式，可以得到在 m_z–$\eta_{\rm A}$ 平面的相图，如图 19 所示。

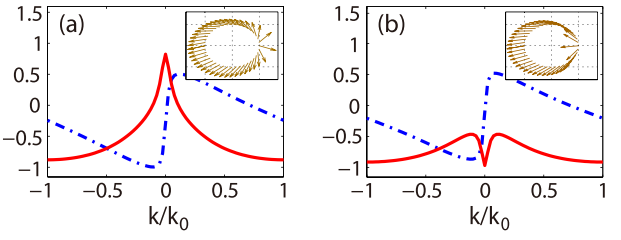

图 18. 第一布里渊区内拓扑超辐射相 (a) 和普通超辐射相 (b) 中典型的自旋分布。其中红色实线代表自旋沿 z 轴分量，黑色虚线代表自旋沿 y 轴分量。插图显示了动量空间中自旋的结构。该图来自参考文献 [77]。

由于腔光场会不断通过腔耗散，一方面，系统最终达到的状态并非热力学平衡态而是动力学稳态；另一方面，系统的持续耗散过程也为观察原子系综提供了一个很好的通道。在半满填充时，费米面的波矢满

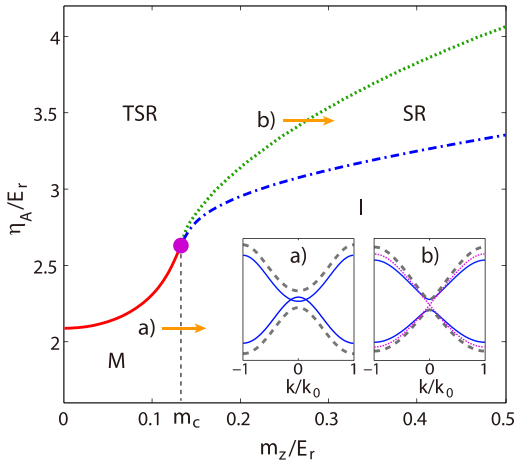

图 19. 具有腔诱导自旋–轨道耦合的无相互作用一维费米气体的相图。当等效磁场 $m_z<m_{\rm c}$ 时，系统随驱动光强度 $\eta_{\rm A}$ 的增加，从正常金属相 (M) 进入拓扑非平庸超辐射相 (TSR)。当 $m_z>m_{\rm c}$ 时，系统在弱驱动时为极化的绝缘体 (I)，经过超辐射相变后进入拓扑平庸的超辐射相 (SR)，随着驱动进一步增强变为非平庸的超辐射相 (TSR)。图中黑色虚线、绿色点线和蓝色点划线代表二级相变，红色实线代表一级相变。在临界磁场 $m_{\rm c}$ 处存在一个四相点。插图显示了沿不同轨迹（黄色箭头）跨越相变线时，能带结构的变化。其中蓝色实线为箭头起点的情形，粉色点线为相变点的情形，灰色虚线为箭头终点的情形。该图来自参考文献 [77]。

足 $2k_{\rm F}=k_0$，因而费米面嵌套效应将显著增强超辐射相变，导致在热力学极限下任意有限的驱动强度都可以引发超辐射相变（图 19 中的有限驱动强度归因于有限尺寸效应），同时在腔光场中留下了特征。例如，腔内光子数的一阶导数 $\partial|\alpha|^2/\partial\eta_{\rm A}$ 会在能隙闭合时表现出一个峰状结构。结合自旋选择的时间飞行测量，在实验上将有可能测量并区分这两种超辐射相。

接下来，我们考虑原子之间的相互作用的影响。这部分哈密顿量的形式如下 [93]

$$\hat{H}_I=-g_{\rm 1D}\int \mathrm{d}x\hat{\Psi}_\uparrow^\dagger(x)\hat{\Psi}_\downarrow^\dagger(x)\hat{\Psi}_\downarrow(x)\hat{\Psi}_\uparrow(x). \quad (45)$$

这里 $g_{\rm 1D}$ 是不同组分之间的有效相互作用强度，可以通过 Feshbach 共振调节 s 波散射长度 a_s 或者通过约束诱导共振调节横向束缚势频率 $\omega_\perp$（或束缚势特征长度 $\rho\equiv\sqrt{\hbar/m\omega_\perp}$）来达到改变 $g_{\rm 1D}$ 的目的

$$g_{\rm 1D}=-\frac{4\pi\hbar^2a_s}{m}\frac{1}{2\pi\rho^2}\left(1-\mathcal{C}\frac{a_s}{\sqrt{2}\rho}\right)^{-1}, \quad (46)$$

式中 $\mathcal{C}=1.4603$。当 $g_{\rm 1D}>0$ 时，原子之间的有效相互作用将是吸引相互作用，相反动量和自旋的原子将由于 BCS 不稳定性形成弱束缚的库伯对 (Cooper pair)，同时费米面将失稳并打开一个能隙，体系进入超流态。

腔光场辅助的自旋–轨道耦合效应会使费米面发生自旋混合，配对态的性质也会发生改变。平均场理论研究表明 [93]，虽然在较大参数范围内发现了超流态和超辐射共存的区域，但是大多数时候并不是原子气体的基态（图 20）。对于费米超流与费米超辐射两种不同序的共存以及其中的拓扑性质有待进一步研究。

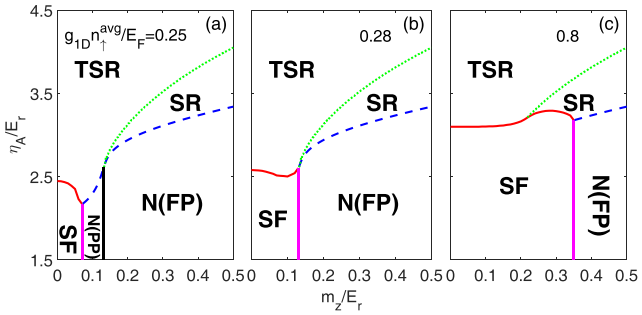

图 20. 具有腔诱导自旋-轨道耦合的一维费米气体在有相互作用时的零温相图。相互作用强度 $g_{1D}n_{\uparrow}^{avg}/E_F$ 从左至右依次为 0.25, 0.28, 0.8，其余参数与图 19 一致。随着相互作用强度的增强，超流 (SF) 的区域变大，正常态（N，包括完全极化 (FP) 和部分极化 (PP)）的区域变小。图中实线表示一阶相变，虚线表示二阶相变，点线表示拓扑相变。该图来自参考文献 [93]。

VI. 总结

本文简要综述了光腔–原子耦合系统中的超辐射相变，并针对超冷玻色气体和费米气体分别介绍了近年来的一些理论和实验进展。从前面的叙述可以看出，原子通过散射驱动光进入光腔，可以在腔内诱导出超辐射相变，腔内光场模式出现宏观占据，同时伴随着原子在空间的分布出现对称性破缺。发生超辐射相变之后，原子在腔光场形成的驻波场中运动，反过来腔光场又受到原子的作用和反馈，二者相互耦合，在长时间极限下共同达到稳态。和自由空间中外加的光晶格相比，超辐射相变后腔光场的主要区别有以下两点。第一，腔光场通过耗散和环境发生耦合，因此体系达到的是动力学稳态，而非热力学平衡态；第二，腔光场和原子发生相干耦合，因此会在不同的原子间诱导出等效的长程相互作用。这些特点不仅会导致该体系的物质相和物质相变具有和传统光晶格系统不同的行为，还为探索非平衡物理、发展非破坏实时测量技术、寻找多体新奇物态等研究提供了丰富的思路。

致 谢

作者感谢国家自然科学基金委（11274009、11434011、11522436）、科技部（2013CB922000）以及中国人民大学科研基金（10XNL016、16XNLQ03）的大力支持。由于时间和作者水平所限，疏漏之处在所难免，敬请读者见谅。

参考文献

[1] Brennecke C F *Collective interaction between a Bose-Einstein condensate and a coherent few-photon field*. PhD thesis, Eidgenössische Technische Hochschule (ETH), Zürich, CH, 2009.
[2] Dicke R H. *Phys. Rev.*, 1954, **93**: 99-110
[3] Inouye S, Chikkatur A P, Stamper-Kurn D M, Stenger J, Pritchard D E, Ketterle W. *Science*, 1999, **285**(5427): 571-574
[4] Inouye S, Pfau T, Gupta S, Chikkatur A P, Görlitz A, Pritchard D E, Ketterle W. *Nature*, 1999, **402**(6762): 641-644
[5] Schneble D, Torii Y, Boyd M, Streed E W, Pritchard D E, Ketterle W. *Science*, 2003, **300**(5618): 475-478
[6] Yoshikawa Y, Torii Y, Kuga T. *Phys. Rev. Lett.*, 2005, **94**: 083602
[7] Li J, Zhou X, Yang F, Chen X. *Phys. Lett. A*, 2008, **372**: 4750-4753
[8] Deng L, Payne M G, Hagley E W. *Phys. Rev. Lett.*, 2010, **104**: 050402
[9] Deng L, Hagley E W, Cao Q, Wang X, Luo X, Wang R, Payne M G, Yang F, Zhou X, Chen X, Zhan M. *Phys. Rev. Lett.*, 2010, **105**: 220404
[10] Zhou X, Yang F, Yue X, Vogt T, Chen X. *Phys. Rev. A*, 2010, **81**: 013615
[11] Wang P, Deng L, Hagley E W, Fu Z, Chai S, Zhang J. *Phys. Rev. Lett.*, 2011, **106**: 210401
[12] Kampel N S, Griesmaier A, Steenstrup M P H, Kaminski F, Polzik E S, Müller J H. *Phys. Rev. Lett.*, 2012, **108**: 090401
[13] Lu B, Zhou X, Vogt T, Fang Z, Chen X. *Phys. Rev. A*, 2011, **83**: 033620
[14] Vogt T, Lu B, Liu X, Xu X, Zhou X, Chen X. *Phys. Rev. A*, 2011, **83**: 053603
[15] Schoelkopf R J, Girvin S M. *Nature*, 2008, **451**(7179): 664-669
[16] Niemczyk T, Deppe F, Huebl H, Menzel E P, Hocke F, Schwarz M J, Garciaripoll J J, Zueco D, Hummer T, Solano E, Marx A, Gross R. *Nat. Phys.*, 2010, **6**(10): 772-776
[17] Colombe Y, Steinmetz T, Dubois G, Linke F, Hunger D, Reichel J. *Nature*, 2007, **450**(7167): 272-276
[18] Tavis M, Cummings F W. *Phys. Lett. A*, 1967, **25**: 714-715
[19] Tavis M, Cummings F W. *Phys. Rev.*, 1968, **170**: 379
[20] Travis M, Cummings F W. *Phys. Rev.*, 1969, **188**: 692-695
[21] Narducci L M, Orszag M, Tuft R A. *Phys. Rev. A*, 1973, **8**: 1892

[22] Hepp K, Lieb E H. *Ann. Phys.*, 1973, **76**(2): 360-404
[23] Wang Y K, Hioe F T. *Phys. Rev. A*, 1973, **7**: 831
[24] De Oliveira F D. *Study of the Dicke model: From phase space approach to quantum trajectories*. PhD thesis, The University of Auckland, Auckland, NZ, 2008
[25] Brennecke F, Donner T, Ritter S, Bourdel T, Köhl M, Esslinger T. *Nature*, 2007, **450**(7167): 268-271
[26] Dimer F, Estienne B, Parkins A S, Carmichael H J. *Phys. Rev. A*, 2007, **75**: 013804
[27] Baden M P, Arnold K J, Grimsmo A L, Parkins S, Barrett M D. *Phys. Rev. Lett.*, 2014, **113**: 020408
[28] Baumann K, Guerlin C, Brennecke F, Esslinger T. *Nature*, 2010, **464**(7293): 1301-1306
[29] Ritsch H, Domokos P, Brennecke F, Esslinger T. *Rev. Mod. Phys.*, 2013, **85**(2):553
[30] Inouye S, Andrews M R, Stenger J, Miesner H J, Stamper-Kurn D M, Ketterle W. *Nature*, 1998, **392**(6672): 151-154
[31] Maschler C, Ritsch H, Vukics A, Domokos P. *Opt. Commun.*, 2007, **273**(2): 446-450
[32] Vukics A, Maschler C, Ritsch H. *New J. Phys.*, 2007, **9**(8): 255
[33] Domokos P, Ritsch H. *Phys. Rev. Lett.*, 2002, **89**: 253003
[34] Black A T, Chan H W, Vuletić V. *Phys. Rev. Lett.*, 2003, **91**: 203001
[35] Zippilli S, Morigi G, Ritsch H. *Phys. Rev. Lett.*, 2004, **93**: 123002
[36] Asbóth J K, Domokos P, Ritsch H, Vukics A. *Phys. Rev. A*, 2005, **72**: 053417
[37] Nagy D, Szirmai G, Domokos P. *Eur. Phys. J. D*, **48**(1): 127 – 137, 2008; see also *arXiv:0801.4771*
[38] Baumann K, Mottl R, Brennecke F, Esslinger T. *Phys. Rev. Lett.*, 2011, **107**: 140402
[39] Nagy D, Kónya G, Szirmai G, Domokos P. *Phys. Rev. Lett.*, 2010, **104**: 130401
[40] Kónya G, Szirmai G, Domokos P. *Eur. Phys. J. D*, 2011, **65**(1-2): 33-42
[41] Öztop B, Bordyuh M, Müstecaplıoğlu Ö E, Türeci H E. *New J. Phys.*, 2012, **14**(8): 085011
[42] Mottl R, Brennecke F, Baumann K, Landig R, Donner T, Esslinger T. *Science*, 2012, **336**(6088): 1570-1573
[43] Kulkarni M, Öztop B, Türeci H E. *Phys. Rev. Lett.*, 2013, **111**: 220408
[44] Nagy D, Szirmai G, Domokos P. *Phys. Rev. A*, 2011, **84**:043637
[45] Dalla Torre E G, Diehl S, Lukin M D, Sachdev S, Strack P. *Phys. Rev. A*, 2013, **87**: 023831
[46] Brennecke F, Mottl R, Baumann K, Landig R, Donner T, Esslinger T. *Proc. Natl. Acad. Sci.*, 2013, **110**(29): 11763-11767
[47] Nagy D, Domokos P. *Phys. Rev. Lett.*, 2015, **115**: 043601
[48] Klinder J, Keßler H, Wolke M, Mathey L, Hemmerich A. *Proc. Natl. Acad. Sci.*, 2015, **112**(11): 3290-3295
[49] Maschler C, Ritsch H. *Phys. Rev. Lett.*, 2005, **95**: 260401
[50] Larson J, Damski B, Morigi G, Lewenstein M. *Phys. Rev. Lett.*, 2008, **100**: 050401
[51] Larson J, Fernández-Vidal S, Morigi G, Lewenstein M. *New J. Phys.*, 2008, **10**(4): 045002
[52] Andreev A F, Lifshits I M. *Zhur. Eksper. Teoret. Fiziki*, 1969, **56**(6): 2057-2068
[53] Kim E, Chan M H W. *Nature*, 2004, **427**(6971): 225-227
[54] Yi S, Li T, Sun C P. *Phys. Rev. Lett.*, 2007, **98**: 260405
[55] Zhang X F, Sun Q, Wen Y C, Liu W M, Eggert S, Ji A C. *Phys. Rev. Lett.*, 2013, **110**: 090402
[56] Kim D Y, Chan M HW. *Phys. Rev. Lett.*, 2012, **109**: 155301
[57] Landig R, Hruby L, Dogra N, Landini M, Mottl R, Donner T, Esslinger T. *Nature*, 2016, **532**(7600): 476
[58] Fernández-Vidal S, De Chiara G, Larson J, Morigi G. *Phys. Rev. A*, 2010, **81**: 043407
[59] Caballero-Benitez S F, Mekhov I B. *Phys. Rev. Lett.*, 2015, **115**: 243604
[60] Niederle A E, Morigi G, Rieger H. *Phys. Rev. A*, 2016, **94**: 033607
[61] Dogra N, Brennecke F, Huber S D, Donner T. *Phys. Rev. A*, 2016, **94**:023632
[62] Chen Y, Yu Z, Zhai H. *Phys. Rev. A*, 2016, **93**: 041601
[63] Li Y, He L, Hofstetter W. *Phys. Rev. A*, 2013, **87**:051604
[64] Bakhtiari M R, Hemmerich A, Ritsch H, Thorwart M. *Phys. Rev. Lett.*, 2014, **114**: 123601
[65] Klinder J, Kesler H, Bakhtiari M R, Thorwart M, Hemmerich A. *Phys. Rev. Lett.*, 2015, **115**: 230403
[66] Lin Y J, Jiménez-García K, Spielman I B. *Nature*, 2011, **471**(7336): 83-86
[67] Wu Z, Zhang L, Sun W, Xu X T, Wang B Z, Ji S C, Deng Y, Chen S, Liu X J, Pan J W. *Science*, 2016, **354**(6308): 83-88
[68] Dong Y, Ye J, Pu H. *Phys. Rev. A*, 2011, **83**: 031608
[69] Dong L, Zhou L, Wu B, Ramachandhran B, Pu H. *Phys. Rev. A*, 2014, **89**: 011602
[70] Wu B, Diener R B, Niu Q. *Phys. Rev. A*, 2002, **65**: 025601
[71] Watanabe G, Yoon S, Dalfovo F. *Phys. Rev. Lett.*, 2011, **107**: 270404
[72] Zhang S L, Zhou Z W, Wu B. *Phys. Rev. A*, 2013, **87**: 013633
[73] Yu D, Yi W, Zhang W. *Phys. Rev. A*, 2015, **92**: 033623
[74] Deng Y, Cheng J, Jing H, Yi S. *Phys. Rev. Lett.*, 2014, **112**: 143007
[75] Guo X, Ren Z, Guo G, Peng J. *Phys. Rev. A*, 2012, **86**: 053605
[76] Padhi B, Ghosh S. *Phys. Rev. Lett.*, 2013, **111**: 043603
[77] Pan J S, Liu X J, Zhang W, Yi W, Guo G C. *Phys. Rev. Lett.*, 2015, **115**: 045303
[78] Kollath C, Sheikhan A, Wolff S, Brennecke F. *Phys. Rev. Lett.*, 2016,**116**: 060401
[79] Chen Y, Yu Z, Zhai H. *Phys. Rev. Lett.*, 2014, **112**: 143004
[80] Piazza F, Strack P. *Phys. Rev. Lett.*, 2014, **112**: 143003
[81] Keeling J, Bhaseen M J, Simons B D. *Phys. Rev. Lett.*, 2014, **112**: 143002
[82] Yang S, Al-Amri M, Zubairy M S. *J. Phys. B At. Mol. Opt. Phys.*, 2014, **47**(13): 135503
[83] Chen Y, Zhai H, Yu Z. *Phys. Rev. A*, 2015, **91**: 021602
[84] Kato Y K, Myers R C, Gossard A C, Awschalom D D. *Science*, 2004, **306**(5703): 1910-1913
[85] Hasan M Z, Kane C L. *Rev. Mod. Phys.*, 2010, **82**: 3045-3067
[86] Sau J D, Lutchyn R M, Tewari S, Sarma S D. *Phys.*

Rev. Lett., 2010, **104**: 040502
[87] Burkov A A, Balents L. *Phys. Rev. Lett.*, 2011, **107**: 127205
[88] Wang P, Yu Z Q, Fu Z, Miao J, Huang J, Chai S, Zhai H, Zhang J. *Phys. Rev. Lett.*, 2012, **109**: 095301
[89] Cheuk L W, Sommer A T, Hadzibabic Z, Yefsah T, Bakr W S, Zwierlein M W. *Phys. Rev. Lett.*, 2012, **109**: 095302
[90] Huang L, Meng Z, Wang P, Peng P, Zhang S L, Chen L, Li D, Zhou D, Zhang J. *Nat. Phys.*, 2016, **12**: 540
[91] Zhang W, Yi W. *Nat. Commun.*, 2013, **4**: 2711
[92] Yi W, Zhang W, Cui X. *Sci. China Phys. Mech. Astron.*, 2015, **58**(1): 014201
[93] Yu D, Pan J S, Liu X J, Zhang W, Yi W. *Front. Phys.*, 2017, In print

Ultracold atomic gases in optical cavities

Yu Dong-Yang[1], Ji Qing[1], Zhang Xiang[1,2], Zhang Wei[1,2]

1. Department of Physics, Renmin University of China, Beijing 100872, People's Republic of China
2. Beijing Key Laboratory of Opto-electronic Functional Materials and Micro-nano Devices, Renmin University of China, Beijing 100872, People's Republic of China

The hybrid system of optical cavity and ultracold atomic gas has caught great attention in recent years. This review article focuses on the up-to-date progresses in both theory and experiment worldwide, especially on the superradiant transition and some interesting quantum phases in Bose or Fermi atomic ensembles. It is shown that the hybrid system is highly valuable in the exploration of many interesting physics including non-equilibrium states, quantum simulation of many-body systems, and synthetical gauge field and spin-orbit coupling.

Key words: Cavity-QED, Ultracold atomic gases, Superradiant transition, Non-equilibrium state